STRUCTURE-PROPERTY RELATIONSHIPS IN LASER ASSISTED AND MECHANICALLY DEFORMED ADVANCED MATERIALS

rijksuniversiteit groningen

STRUCTURE-PROPERTY RELATIONSHIPS IN LASER ASSISTED AND MECHANICALLY DEFORMED ADVANCED MATERIALS

Proefschrift

ter verkrijging van de graad van doctor aan de
Rijksuniversiteit Groningen
op gezag van de
rector magnificus prof.dr. C. Wijmenga
en volgens besluit van het College voor Promoties.

De openbare verdediging zal plaatsvinden op

Vrijdag 20 November 2020 om 16.15 uur

door

Herman Fidder

geboren op 21 Mei 1985
te Stellenbosch, Zuid-Afrika

Promotor
Prof. dr. J. Th. M. De Hosson

Co-promotor
Dr. V. Ocelík

Beoordelingscommissie
Prof. dr. P. Rudolf
Prof. dr. H.A. De Raedt
Prof. dr. A. Botes

STRUCTURE-PROPERTY RELATIONSHIPS IN LASER ASSISTED AND MECHANICALLY DEFORMED ADVANCED MATERIALS

Herman Fidder

PhD thesis
University of Groningen

Zernike Institute PhD thesis series 2020-11
ISSN: 1570-1530
ISBN: 978-94-034-2690-7 (Printed version)
ISBN: 978-94-034-2691-4 (Electronic version)
Print: Zalsman Groningen B.V.

The research presented in this thesis was performed in the Department of Applied Physics and Engineering, Materials Science group of the Zernike Institute for Advanced Materials at the University of Groningen, the Netherlands.
This work was funded by the Zernike Institute for Advanced Materials.

Cover: Titanium test sample subjected to laser forming and mechanical forming processes. Microstructural behavior of these processes is illustrated.

CONTENTS

Chapter 1

Introduction

1.1 Background and motivations

The acronym '*LASER*' stands for "Light Amplification by Stimulated Emission of Radiation". In 1917 Einstein laid the foundation for the laser by introducing this novel idea concerning stimulated emission [1]. The phenomenon was supposed to occur by the transition of an atom or molecule to a lower energy state under influence of electromagnetic radiation.

In fact the basic principle of *amplification* is to create a population inversion between the ground and an excited state, by pumping atoms from the ground state to a higher energy level. Subsequently, stimulated emission takes place if an incoming photon, with an energy corresponding to the energy transition of the atom, causes the emission of a coherent photon. By using a resonant cavity there will be an avalanche of stimulated emission of photons and even more amplification takes place. The created beam can be transported from the cavity by using a semi-transparent mirror. Besides its coherence, the emitted light is highly monochromatic and directional, which enables very efficient focusing. It should be realized that it took roughly four decades before the idea of Albert Einstein became reality in practice. After the theoretical discovery of masers in 1958 by Schawlow and Townes [2], Maiman demonstrated in 1960 the very first laser by using a ruby crystal [3].

For surface treatments by lasers in material science and engineering both a high power density and a high total power are necessary, which restrict the type of lasers to be used. At present several types of high-power lasers are available on the market. The first type is the continuous wave CO_2 laser with a maximum power in the range of kilo-Watts. This laser contains a mixture of three gases: nitrogen, helium and carbon dioxide. Vibrational modes of the CO_2 molecule give rise to the laser effect with a wavelength of 10.6 μm. The efficiency of the laser is ~10 %, which is relative high in comparison to many other types of lasers. The second type is the Nd-YAG and also used in so-called fiber lasers as have been used in this study. It is possible to reach output powers in the range of kilo-Watts for this type of solid state laser. The active

element Nd3+ gives rise to the laser effect with a wavelength of 1.06 μm. This wavelength makes it possible to transport the beam by means of fibers. A wavelength of 1.06 μm is sufficient for materials strongly reflecting to a 10.6 μm wavelength, such as Ti and Al, so as to obtain the electromagnetic radiation, i.e. light, into the outer surface layer transported into the bulk of these metallic systems.

Besides the high power density, a high total power is essential for economically feasible materials processing, limiting the types of lasers that are used in materials processing to CO_2 and YAG/Fiber lasers. In industrial applications these lasers are mainly used for welding and cutting. Lasers are used to a lesser extent for heat treatments, melting and alloying of metals. The *Materiaalkunde* (MK) group has worked for decades on laser processing of coatings and cladding, which are at present discovered once again in trending wordings such as '3D- printing'. In fact the latter dates back more than 4 decades ago in cladding technology but indeed it sales better though 'marketing technology' , as 'additive manufacturing processing' and '3D-printing'.

The main aspect of the laser treatment of materials is the localized heat treatment of the surface material. This makes treatment of small surface areas possible without destroying the bulk properties of a material and limits the amount of expensive elements needed for alloying. Sometimes the localized melting is followed by a rapid self-quench with cooling rates of 10^5 - 10^8 °C/s. This results in further refinement of the grain size and may even produce metastable or amorphous phases. Laser transformation hardening (without melting) and alloying (with melting) have attracted considerable attention in recent years as methods to improve the chemical and mechanical surface properties of metals. Further, improvement of mechanical properties has been obtained by injecting ceramic particles into the laser melted metal. These ceramic particles are not always completely melted by the laser beam resulting in the formation of metal matrix composite surface layers [4,5,6,7].

This thesis builds on and completes all previous works by exploring a new 'challenge and opportunity' for lasers in the field of manufacturing processing, i.e. using a laser as an innovative tool for *materials forming* purposes. Indeed the laser have been used before as a sophisticated heat source for manufacturing products but the *processing-structure-property* relationships have been largely neglected. Here, we present a detailed and in-depth study of the structure-performance relationships in laser assisted and mechanically deformed advanced materials.

As far as the materials systems are concerned, we have concentrated mainly on Ti-base alloys. Indeed Ti is an exceptional and (at the same time) intriguing metal; it has in fact the largest specific strength of all the metallic systems in the periodic table (i.e. strength over density), i.e. light weight and high strength at the same time. Titanium was discovered by William Gregor [8] in 1791. He was interested in minerals and recognized the presence of a new element, now known as titanium, in menachanite, a mineral named after Menaccan in Cornwall (England). A couple of years later, the element was rediscovered in the ore rutile by a German chemist M.H. Klaproth and he named it titanium (Ti) [9], after the Titans, the powerful sons of Uranus and Gaea out of the (Greek) mythology (also τιτανοσ plaster of Paris). The element Ti is the fourth most abundant metal in the earth's crust. The high strength to weight ratio and its excellent corrosion resistance makes titanium extremely suitable as material for many applications in the field of aerospace, automotive and chemical engineering. In addition, Ti exhibits a high melting temperature and can be used at temperatures up to 550 °C with good fatigue, creep and toughness properties. The excellent corrosion resistance makes Ti a suitable material for propeller shafts, rigging, and other parts of ships exposed to salty water.

The request for specific demands is satisfied by the versatile range of Ti alloys. However, a more widespread use has frequently been inhibited as a result of its less-favored tribological properties. Therefore substantial research has been devoted to the surface engineering aspects in order to obtain protective coatings and thereby to widen the potential range of applications beyond that of construction materials in general by lasers [10,11,12,13].

As a structural material Ti-base alloys are therefore attractive in products but also the functional properties such as low thermal conductivity (about 5 times smaller than aluminum) makes it an interesting choice for local heating by lasers in manufacturing processing. As already mentioned, an advantage of laser processing is the capability to heat up or melt the surface layer locally. Another advantage of a laser system in manufacturing processing is the possibility to manipulate the laser beam by means of an optical system to modify the surface of complex geometrical objects. In addition, laser processing is *contactless* and the thermomechanical deformation of the substrate is generally low. In summary: the above motivation justifies the choice of using Ti-based materials in this thesis to explore the combination of intrinsic and attractive structural and functional material properties.

1.2 Outline of the Thesis

Chapter 2 discusses a number of experimental tools that have been used for the microscopy characterization. Not all the details will be presented but rather a summary for the non-experts so as to grasp the essentials in scanning electron microscopy and electron back scatter diffraction. For Digital Image correlation (DIC) techniques and (nano-) indentation techniques reference will be made to literature or else it will be explained later in the appropriate chapters.

Chapter 3 presents the temperature models of various laser heat treatments. The initial model develops from steady state and progresses towards a dynamic model with a multi-pass laser source and heat-treated Ti-material with temperature dependent material properties. The resulting model leads to a hypothesis about the dependence of laser forming on the experimental controllable parameters such as power, power density and laser scanning velocity. Several of the hypotheses will be verified against experimental observations in Chapters 5 and 6.

Chapter 4 is on the mechanical characterization of the effect of various forming processes applied to commercially pure titanium whereas

Chapter 5 presents the response of Ti microstructure in mechanical and laser forming processes.

Chapter 6 reports the *in-situ* digital image correlation observations of laser forming.

Chapter 7 sets aside by focusing, not on laser forming as such, but on the local stress states and microstructural damage responses due to deformation twins in Hexagonal Close Packed Metals such as Ti.

The thesis is concluded by a summary and some recommendations towards future research based on the new insights obtained.

1.3 References

[1] A. Einstein, Phys. Z., 18, 121 (1917).

[2] A.L. Schalow and C.H. Townes, Phys.Rev., 112, 1940-1949 (1958).

[3] T.H. Maiman, Nature, 187, 493 (1960).

[4] I. Hemmati, V. Ocelik, J.Th.M. De Hosson, Compositional modification of Ni-base alloys for laser-deposition technologies, in: Laser Surface Engineering, Processes and Applications, eds: J. Lawrence and D.G. Waugh, Woodhead Publishing is an imprint of Elsevier, Cambridge UK, 2015, pp.135-162.

[5] V. Ocelík and J.Th.M. De Hosson, 'Thick metallic coatings by coaxial and si-de laser cladding: processing and properties', in: J. Lawrence, J. Pou, D.K. Y. Low, and E. Toyserkani (eds.), *Advances in laser materials processing technology*, Oxford (UK)-West Palm Beach (USA): Woodhead Publishing Ltd. and CRC Press, 2010, Chapter 15, pp.426-458.

[6] J.Th.M. De Hosson, 'Laser synthesis and properties of ceramic coatings', in: N.B. Dahotre, T.S. Sudarshan (eds.), *Intermetallic and Ceramic Coatings*, New York: Marcel Dekker Inc., 1999, pp.307-441.

[7] J.Th.M. De Hosson and D.H.J. Teeuw, 'Laser deposition of ceramic coatings', in: N.B. Dahotre (ed.), *Surface Engineering Series*, Volume 1, Materials Park, Ohio: American Society for Metals, 1998, pp.205-255.

[8] W. Gregor, Chemische Annalen für die Freunde der Naturlehre, 1, p.40, 2, p.55, 1791.

[9] M.H. Klaproth, Beiträge zur chemischen Kenntnis der Mineralkörper, I, p.227, 1795.

[10] A.B. Kloosterman, PhD Thesis, *Surface modification of Titanium with lasers*, University of Groningen, 1998, 8-5-1998.

[11] J.A. Vreeling, PhD Thesis, *Laser melt injection of ceramic particles in metals*, University of Groningen, 16-11-2001.

[12] Uazir Orion Bezerra de Oliveira, PhD Thesis, *Laser treatment of alloys*, University of Groningen, 9-2-2007.

[13] O. Nenadl, PhD Thesis, *Laser surface modification and design in strip steel processing*, University of Groningen, 1-1-2016.

Chapter 2

Experimental methods

2.1 Scanning Electron Microscopy

Scanning Electron Microscopy (SEM) is a type of electron microscope that studies microstructural and morphological features of the sample surface by scanning it with a high-energy electron beam in a raster scanning pattern. The electrons interact with the sample matter producing a variety of signals that contain information about the sample surface topography, chemical composition and other structural quantities such as mechanical stress state and functional properties, e.g. electron conductivity and magnetism.

The first SEM image was obtained by Max Knoll, who in 1935 obtained an image of silicon steel showing electron channeling contrast [1]. The SEM was further developed by Sir Charles Oatley and his postgraduate student Gary Stewart and was first marketed in 1965 by the Cambridge Instrument Company as the "Stereoscan".

The signals produced by a SEM include secondary and back-scattered electrons (SE & BSE), characteristic X-rays, cathodoluminescence (light), specimen current and transmitted electrons. The SE detector is the most common one in SEM. As shown by the schematic Fig. 2.1 electrons are generated by the field emission gun using a high electrostatic field. They are accelerated with potentials between 1 kV and 30 kV down through the column towards the specimen. While the magnetic lenses (condenser and objective lenses) focus the electron beam to a spot with a diameter of approximately 10 nm, the scanning coils sweep the focused electron beam over the specimen surface. If the microscope is operated in the so-called back-scattered mode, the result is a lateral resolution of the order of nanometers. The number of back-scattered electrons produced is proportional to the atomic number of the element bombarded. The result is that material with a high(er) atomic number produces a brighter image. To capture this information a detector is required which can either be a metal, which is the least effective, but is versatile and used in environmental scanning electron microscopy (ESEM); a semi-

conductor, which is most common or a scintillator/ light pipe/ photo-multiplier, which is the most efficient.

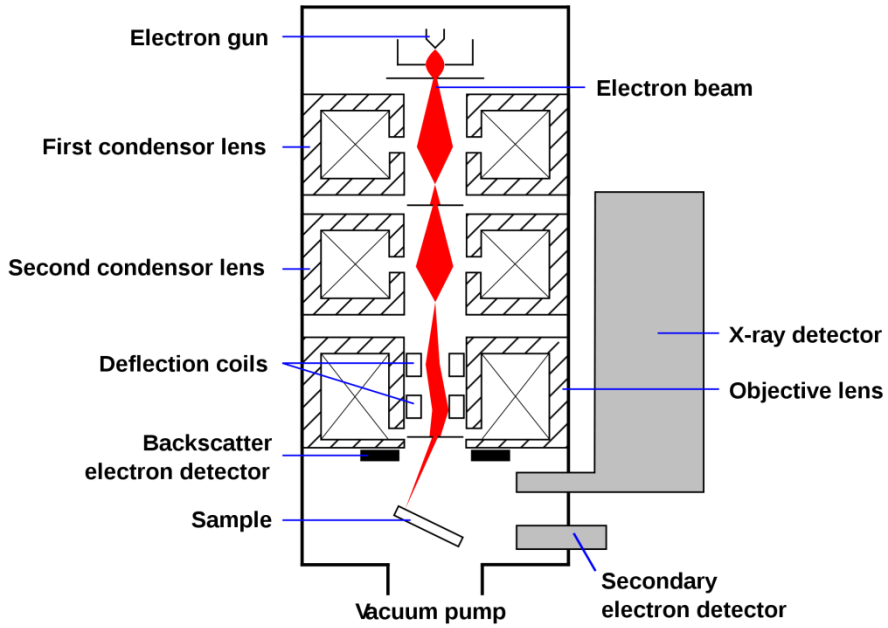

Fig. 2.1: Schematic figure of the Scanning Electron Microscopy

The primary electron current is approximately 10^{-8} to 10^{-7}A. The large penetration depth of the high energy electrons will cause the electrons to be trapped in the material. When studying conducting materials, the electrons will be transported away from the point of incidence. If the specimen is a non-conducting material, the excess electrons will cause charging of the surface. The electrostatic charge on the surface deflects the incoming electrons, giving rise to distortion of the image. To reduce surface charging effects, a conducting layer of metal, with typical thicknesses of 5-10 nm, can be sputtered onto the surface. This layer will transport the excess electrons, reducing the negative charging effects. An adverse effect of the sputtered layer is that it may diminish the resolving power of the microscope, since topographical information is no longer gained from the surface of the material, but from the sputtered layer. Charging of the surface is not the only factor determining the resolution of a SEM. The width of the electron beam is also an important factor for the lateral resolution. A narrow electron beam results in a high resolution. The spot size however, is a function of the accelerating voltage. The broadening of the spot size d_p in Eq. (2.1) is the sum of broadening effects due to several processes. The first contributor is the

beam itself, B is the brightness of the source, i is the beam current and α its divergence angle. The second part is the contribution due to diffraction of the electrons of wavelength λ by the size of the final aperture. The last two parts are the broadening caused by chromatic and spherical aberrations. Hence,

$$d_p^2 = \frac{1}{\alpha^2}\left[\frac{i}{B} + \lambda^2\right] + \left[\frac{\Delta E}{E_0} C_c\right]^2 \alpha^2 + \left[\frac{1}{2} C_s\right]^2 \alpha^6 \qquad (2.1)$$

where E_0 is the electron energy and ΔE is the energy spread, C_s represents the spherical aberration and C_c is the chromatic aberration coefficient. To achieve the smallest spot size, all contributions should be as small as possible. Decreasing the accelerating voltage will not only cause the wavelength of the electrons to increase, but the chromatic aberration will increase as well, resulting in increasing of the spot size and, as a consequence, a decrease in resolving power of the microscope.

A field emission gun has a very high brightness B, reducing the contribution in broadening due to the beam itself. The energy spread ΔE in the electron energies is also small. The fact that the coefficients C_s and C_c can be reduced by optimizing the lenses for low-energy electrons, provides the scanning electron microscope with very high resolving power. In this thesis scanning electron microscopy is carried out with a field emission gun (FEG).

2.2 Electron Backscattered Diffraction

Orientation Imaging Microscopy (OIM^{TM}) is based on automatic indexing of electron backscatter diffraction patterns (EBSD patterns or EBSPs) which can be produced in a properly equipped SEM. OIM provides a complete description of the crystallographic orientations in polycrystalline materials.

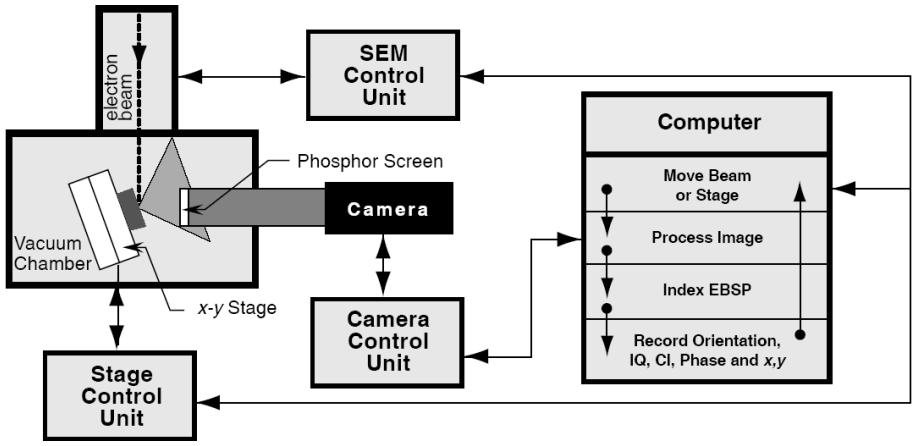

Fig. 2.2: OIM™ Hardware Configuration

OIM hardware

A camera is mounted on the SEM and images a phosphor screen inside the specimen chamber (Fig. 2.2). The electron beam is focused on a particular point of interest in the sample. The interaction of the beam and the microstructure results in an EBSD image forming on the phosphor screen, which is captured by the camera and then further processed and digitalized in a computer. The image is automatically indexed and the following data are calculated and recorded: the orientation of the crystal, a quality factor defining the sharpness of the diffraction pattern (IQ), a TSL-patented "confidence index" (CI) indicating the degree of confidence that the orientation calculation is correct, the phase of the material, and the location (in *x*,*y* coordinates) where the data was obtained on the specimen.

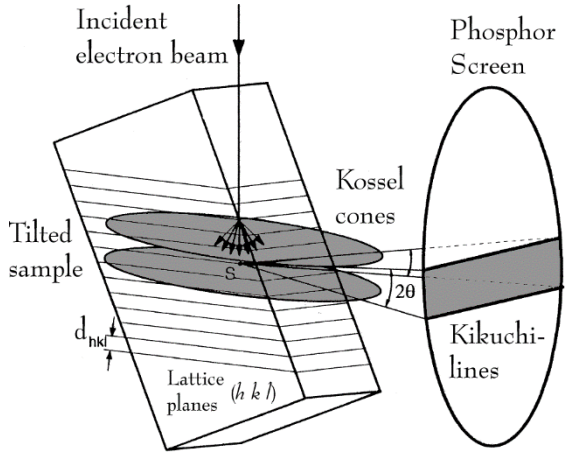

Fig. 2.3: Formation of Kikuchi lines for EBSD Pattern

Formation of EBSP

The EBSD technique relies on accurate/precise positioning of the specimen within the SEM chamber. Typically the surface is tilted 70° with respect to the horizontal to obtain a satisfactory compromise between a high electron scattering yield and a safe configuration in the chamber. This enhances the fraction of backscattered electrons that are able to experience diffraction by lattice planes in the sampled volume and to escape from the specimen surface. This can be understood considering the following: when the primary electrons enter a crystalline solid, the electrons disperse beneath the surface and subsequently they are diffusely and inelastically scattered in all directions.

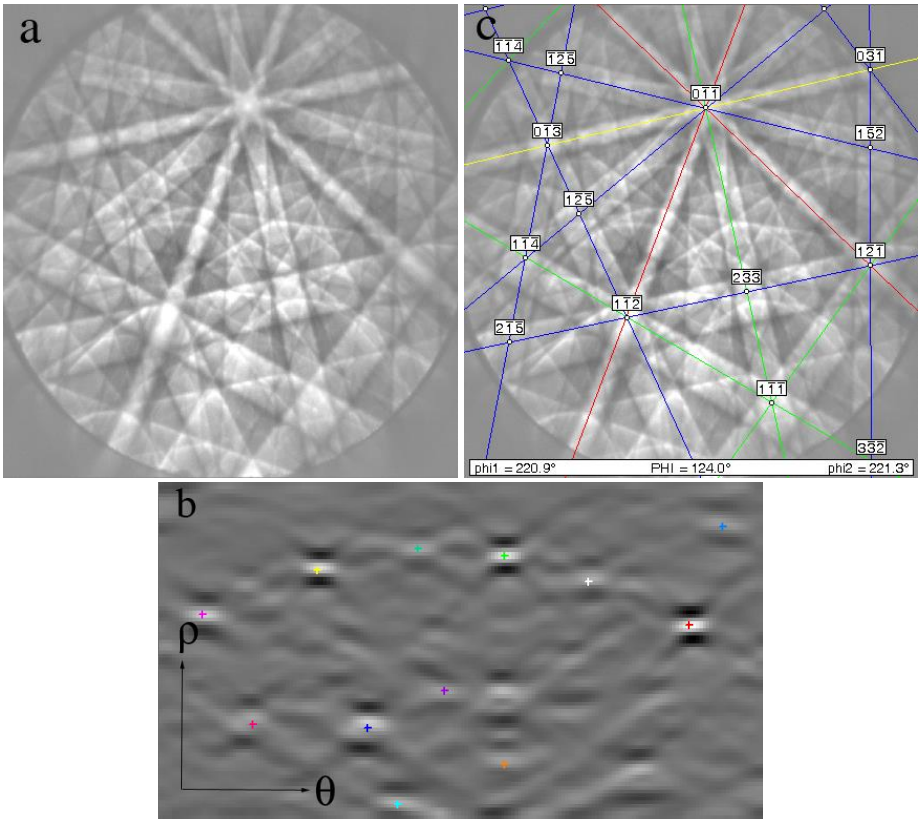

Fig. 2.4: Automated EBSD, a) Kikuchi patterns are transformed to b) Hough space where individual high intensity peaks are detected thereafter c) an orientation is indexed.

These diffracted electrons through the Bragg angle are occurring in all directions. From each family of planes the result are two cones with one from either side of the imaginary source (Fig. 2.3). The Bragg angle, for typical

values of the electron wavelength and lattice interplanar spacing, is found to be about 0.5°. Consequently, the apex angle of a diffraction cone is close to 180°, i.e. the cones are almost flat. When the phosphor screen intercepts the diffraction cones, a pair of parallel conic sections result, which appear as parallel lines, *i.e.*, the so-called Kikuchi lines.

Analysis of EBSPs

In commercial automated analysis of digital images, due to the imperfections in either the image data or the edge detector which is generally used for sharp brightness detection, a problem often arises of detecting the simple shapes, such as straight lines, circles or ellipses. There may be missing points or pixels on the desired shapes as well as spatial deviations between the ideal line/circle/ellipse and the noisy edge points obtained by the edge detector. To circumvent this problem one treats the data by applying the Hough transform which was developed to extract straight lines from digital images. In its current form the Hough transform analyzes the image grouping edge points into object candidates by performing an explicit voting procedure over a set of parameterized image objects [2]. The classical Hough transform was concerned with the extraction of straight lines from digital images, but later on it has been extended to identification of arbitrary shapes, for example circles and ellipses.

The equation governing the Hough transform is

$$\rho = x\cos\theta + y\sin\theta \tag{2.2}$$

where (x,y) describe a set of pixel coordinates forming a line in the digital image and the Hough parameter (ρ,θ) provides a wave like function in Hough space. As the intensity of each (x,y) pixel is added, the problem of finding a Kikuchi band is now reduced in finding a peak of relatively high intensity in the Hough space (Fig. 2.4b). Once the bands have been detected, the reflecting planes associated with the detected bands must be identified. Two band characteristics can be used for indexing; (1) the width of a band, which is a direct function of the d-spacing through Bragg's law; this option is a powerful tool for improved accuracy dealing with structures of low symmetry and for phase identification. (2) The angles between the (located) bands which are known and compared to a theoretical directory of interplanar angles; this is the standard method used in the OIM analysis software.

The indexing routine derives an orientation solution from just three Kikuchi bands and successively analyzes all possible combinations of band triplets. The selection of the most likely indexing solution is to use the voting scheme. That is, each time the angles in a triplet of bands are compared to the

look-up table of angles that are constructed from the crystallography of the sample allowing the Miler indices *(h k l)* associated with the bands to be identified, the solution receives a vote. The most probable solution is the one that receives the majority of votes.

To assess the reliability of the indexing, several parameters such as the *image quality* (IQ), the *confidence index* (CI) and the *fit* between the recalculated and the detected bands may be discerned. The IQ reviews the relative quality of the pattern using the intensities of the found Hough peaks. The CI is given by

$$CI = \frac{(V_1 - V_2)}{V_{total}} \tag{2.3}$$

where V_1 and V_2 are the number of *votes* for the first and second solutions and V_{total} represents the total possible number of votes from the detected bands. The CI will yield a value between 0 and 1. The comparison between the two highest numbers of votes gives this quantity a doubtful character and may be misleading. Especially in the case where V_1 equals V_2, results in a CI of 0. The pattern however may be properly indexed. In general, CI values higher than 0.1 *will* represent a proper indexed pattern. The *fit* parameter defines the average angular deviation between the recalculated and the detected bands. It is often simply a measure of how well the system is calibrated and the parameters defining the crystal structure are defined.

2.3 Energy Dispersive X-ray Spectroscopy

The elemental composition is determined by Energy Dispersive X-ray spectroscopy (EDS). The X-rays originate from the energy release when an outer shell electron is filling an inner shell vacancy created by the focused electron beam. The energy release created by the difference in energy of electron orbits is characteristic for each element.

The depth of information is approximately 1-10 μm depending on the acceleration voltage. A downside of this method is that the quantification of lighter elements is less accurate, e.g. C and O. The EDS system (EDAX, Utah, USA) used in this thesis is used in combination with a SEM environment in both the Philips XL30 and Lyra TESCAN SEM.

2.4 Pole Figure & Inverse Pole Figure

One way to represent the crystal orientation distribution is by projecting the 3D orientation data on a 2D reference surface. The pole figure (PF) and inverse pole figure (IPF) are such projections. The PF relates a specific crystal direction to the sample coordinate system. The IPF is switching that relationship as the name implies and relates the crystal directions to a specific sample plane. A full description of the orientation distribution can only be given by multiple PFs or IPFs. A more detailed description of the pole figure and inverse pole figure can be found in [3], [4] and [5].

The PF is constructed by looking at poles, belonging to a specific crystal direction for all the measured points and project these poles on a sample reference plane. The poles are made by looking at the intersection of the crystal directions with a reference sphere, for example the <001> has 3 intersections with the upper half of the reference sphere as seen in Fig. 2.5/2.6. The result is a PF. When this construction is repeated for all crystal orientations in the sample, one obtains the ensemble of all projections which represents the orientation distribution in the sample. The PF is especially useful to observe any rotational preference around a specific crystal direction.

The IPF is constructed by looking in a specific sample direction with respect to the crystal coordinate system. The construction is analogue to the construction of the PF, but the poles are made by the sample direction with the reference sphere in the crystal coordinate system.

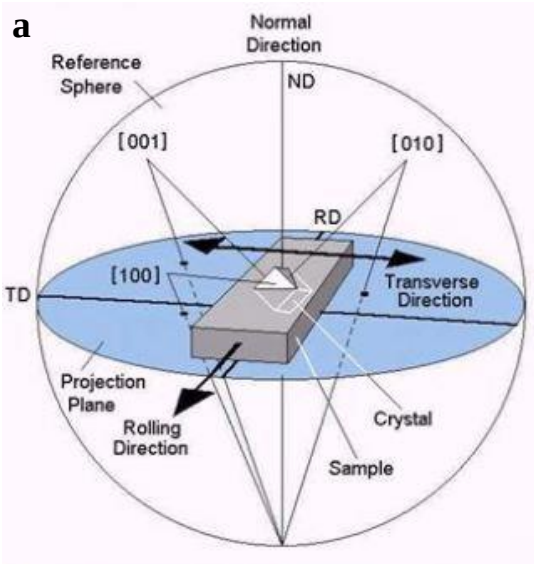

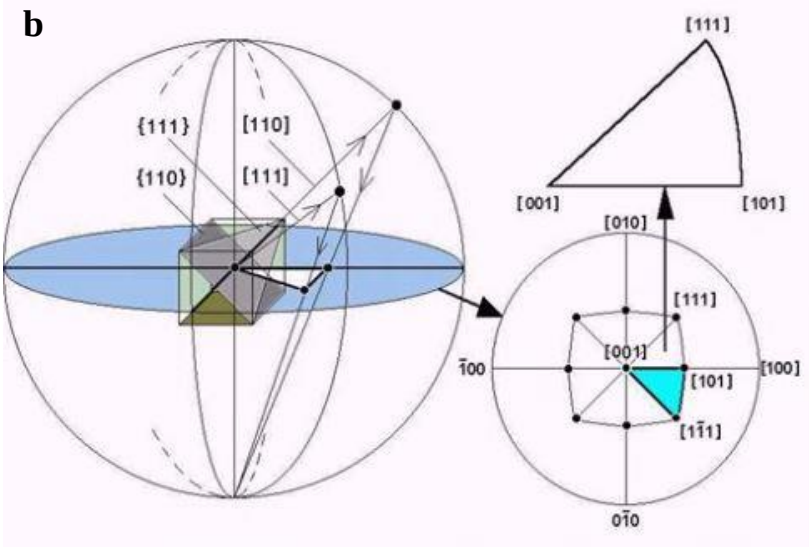

Fig. 2.5. a: PF: pole figure shows the orientation graphically whilst the specimen axes are convenient for the purpose of reference axes. b: IPF: inverse pole figure: The axes are crystallographic directions, not sample directions as in a pole figure. This conveniently shows the orientation of planes to a chosen surface. (Oxford Instruments)

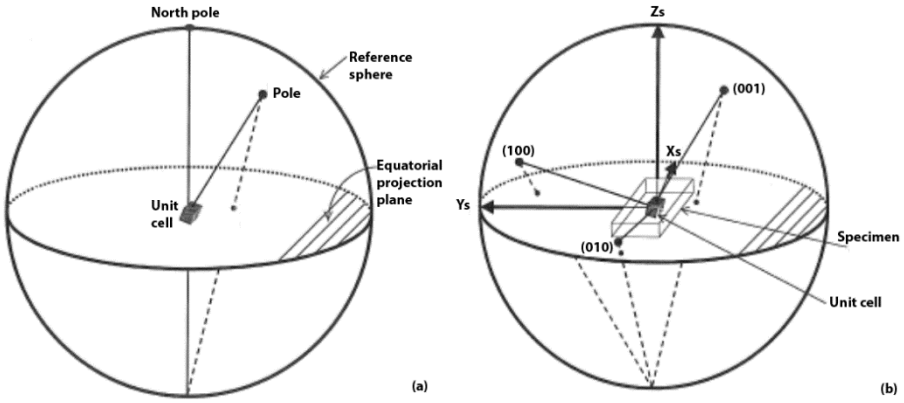

Fig. 2.6: Construction of a pole figure. (a) Poles represent a certain crystal direction and are constructed by the intersection of a crystal direction vector with the reference sphere. The projection of the pole on the reference surface gives the PF for that particular crystal direction. (b) For a crystal direction the multiplicity due to symmetry has to be considered and multiple poles can be constructed for a crystal direction, i.e. three poles can be constructed for the cubic <001> direction (from [4]).

The ensemble of projections forms the IPF and because of symmetry a reduced part of the reference plane gives the full orientation distribution. The IPF is especially useful to observe any preference of crystal direction with respect to a sample plane.

2.5 Microstructural maps: KAM, GAM, GOS, LAM, LOS, GROD

The microstructure measured by EBSD can be represented in microstructural maps in a number of manners. The most popular are inverse pole figure maps, where the crystallographic direction (detected in each individual scanned point) parallel to a given sample coordinate axis is shown in a color. Localized microstructural deformation has been studied in this text; therefore local misorientation maps will be presented due to their ability to characterize some aspects of microstructural localized strain [6]. These microstructural maps represent either global grain information or local information within a grain, depending on the chosen methodology. Typical nomenclature of misorientation maps has been used in the text, e.g. KAM. For more details reference is made to the PhD Thesis by Leo de Jeer [7].

The methodology is either based on the whole grain, in which all the points in the grain are considered, or based on an arbitrary sized kernel, in which only the points in the kernel are considered. However, the points of a kernel must lie in the same grain. The kernel approach gives local information and is formed by a center point plus the 1_{st} until n_{th} nearest neighbors, with n being an arbitrary integer larger than 0. The larger n, the more statistical averaging is performed. The values of these kernel based maps are highly dependent on the chosen step size of the scan.

The Kernel Average Misorientation (KAM) gives the average misorientation with respect to the center of the kernel and gives information on a local level. The misorientation values are calculated with respect to the crystal orientation of the kernel center. With KAM either the points at the kernel's perimeter or all the points in the kernel can be considered. The KAM is useful to calculate the long range and short range deformation within a grain (refer to Fig. 2.7a).

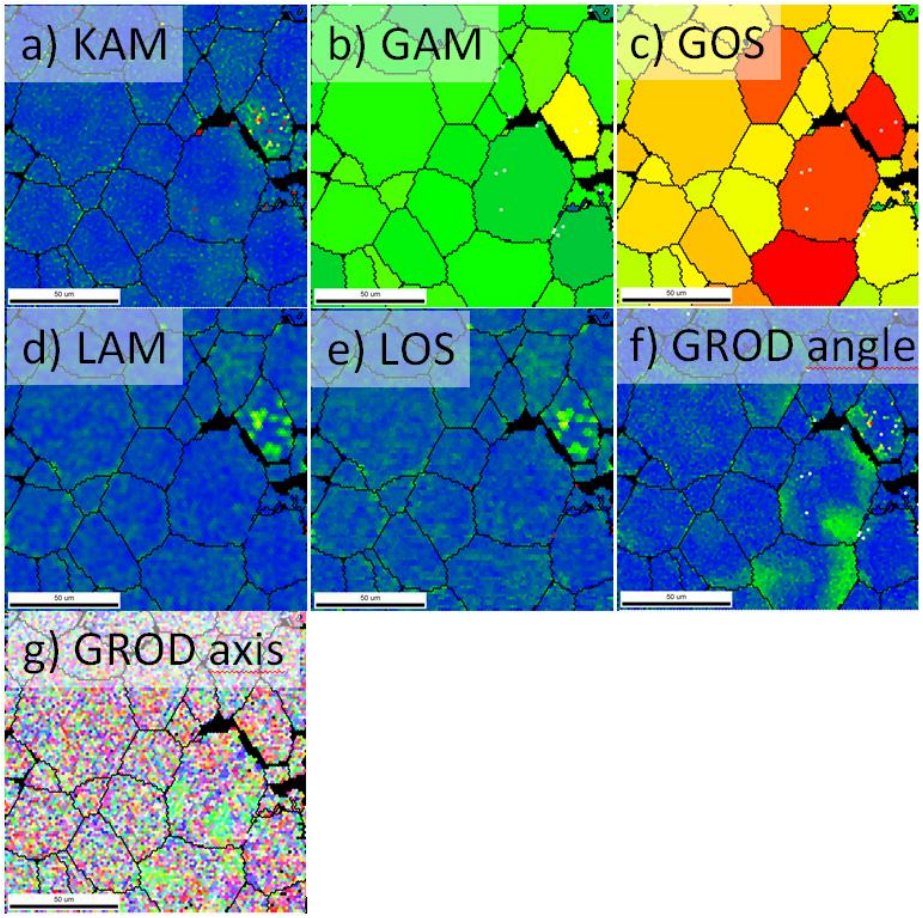

Fig. 2.7: Different microstructural misorientation maps of the same scanned area. (a) KAM : Kernel Average Misorientation, (b) GAM : Grain Average Misorientation, (c) GOS : Grain Orientation Spread, (d) LAM : Local Average Misorientation, (e) LOS : Local Orientation Spread, (f) GROD angle : Grain Reference Orientation Deviation Angle and (g) GROD axis : Grain Reference Orientation Deviation Axis [6]

The Grain Average Misorientation (GAM) and Grain Orientation Spread (GOS) give both grain level based information about the average and spread of the misorientation distribution within a grain, respectively. Examples of these maps are found in Fig. 2.7b and c and give a single value per grain. The misorientation distribution is formed by all the misorientation angles between a point and its neighbors within one grain. These two microstructural maps give insight in the degree of deformation per grain and are very useful for the comparison of deformation as function of the crystal orientation.

The Local Average Misorientation (LAM) and Local Orientation Spread (LOS) both give local level based information within an arbitrary sized kernel of points. Similarly to the GAM and GOS, the LAM and LOS give the average and spread of the neighbor to neighbor misorientation distribution within the kernel and these values are assigned to the center of the kernel of the respective maps. Examples of the maps are found in Fig. 2.7d & e. These two microstructural misorientation maps give insight in the degree of local deformation within the grain and are very useful to pinpoint site specific high strained areas.

The Grain Reference Orientation Deviation (GROD) axis or angle gives the misorientation axis or angle with respect to a reference orientation of a grain on a local level. The reference orientation can be either the average crystal orientation of the grain or the crystal orientation of the point with the lowest KAM value of the grain. An advantage of the latter approach is that the reference orientation represents a physical orientation. Examples of these maps are found in Fig. 2.7f & g. These types of maps give insight into the change in deformation with respect to a fixed crystal orientation in the grain.

2.6 References

[1] M. Knoll, Aufladepotentiel und Sekundäremission elektronenbestrahlter Körper. Zeitschrift für technische Physik 1935, 16, 467-475.

[2] R.O. Duda and P.E. Hart, Use of Hough Transformation to Detect Lines and Curves in Pictures. Communications of the Acm 1972, 15, (1), 11-15.

[3] U.F. Kocks, C.N. Tomé and H.-R. Wenk, Eds., *Texture and anisotropy: preferred orientations in polycrystals and their effect on materials properties*. Cambridge: Cambridge Univ. Press, 1998.

[4] Randle, V., *Microtexture determination and its application*, Second Edition. London, United Kingdom: Maney Publishing, 2003.

[5] Z. Chen, *Superplasticity of coarse grained aluminum alloys*, University of Groningen, 2010, 10-9-2010.

[6] S.I. Wright, M.M. Nowell & D.P. Field, A Review of strain analysis using electron backscatter diffraction, Microscopy and Microanalysis 17: 316-329, 2011

[7] L.T.H. de Jeer, Microscopy study of advanced engineering materials, PhD Thesis, University of Groningen, 2018, 12-1-2018.

Chapter 3

Thermal control: theoretical considerations

3.1 Optical properties and laser irradiation

A breakthrough in the application of lasers to the field of interface engineering is inconceivable without a thorough knowledge of the thermal control during laser processing [1,2]. Processes such as phase transitions and chemical reactions depend significantly on the peak temperature attained. In addition to the maximum temperature, the temperature gradients are of crucial importance. The cooling rate determines if the phase transformations that occur are conformable to the equilibrium phase diagram and it also influences the refinement of the microstructure [3,4]. Additionally, thermal stresses will be induced in the modified layer as a consequence of the thermal gradient [5]. Both the microstructural composition and the residual stress state will determine the final performance of the laser-modified layer. In order to gain insight into the thermal control, the present chapter describes those phenomena which are related to this. Therefore, in principle, the optical properties of a surface have to be examined in connection with the optical temperature measurements and the absorption of the laser radiation.

An analytical model is presented that is used to calculate the temperature field under different processing conditions by using Green's functions [6]. The mathematical treatment is quite general but will focus at the end on the laser forming process. Special attention is paid to the influence of finite-sized specimen. The temperature (T) of a body can be measured in several ways [7]. In principle, a distinction can be made as to which way detection occurs, that is, by either direct contact or contactless. The first method, involves the thermocouple and although it is a well-known tool, it has the disadvantage of low response time. The measurement is furthermore rather static. As a consequence, this method is not suitable for measuring locally high-temperature gradients. Therefore, the contactless way of measuring is preferable because it determines the temperature of a body by measuring its emitted radiation. In the past in the MK group we have measured the T-profile by optical means. Three different types of optical

pyrometer systems are available at the moment, namely monochromatic, two-color and multi-wavelength pyrometers [8]. The basic principle of the optical pyrometer involves measuring infrared (IR) radiation, which is related to temperature as described by Planck's radiation law. However, as most surfaces do not behave like perfect blackbodies, intensity also depends on emissivity. The latter two mentioned pyrometers circumvent the emissivity measurement issue by measuring at two or more wavelengths. In our work thermal imaging was recorded throughout the laser forming (LF) process by means of a forward-looking infrared (FLIR) camera. Additionally, a pyrometer was also used to measure the bottom area of the specimen during the LF process (Chapter 5).

Nonetheless, henceforth the temperature calculations are based on the assumption that the emissivity at both wavelengths and their temperature dependence are equal, which may introduce error. At first sight the monochromatic pyrometer measures only temperature accurately when the emissivity data are well known for the entire temperature range. However, when these data are not exactly known, it is still possible to measure the temperature accurately for metals by choosing the appropriate wavelength to detect. This is due to the fact that the IR radiation originating from a body depends more strongly on temperature than on emissivity. As a consequence, deviations in emissivity result only in relatively small errors in temperature.

To study the energy exchange at a surface, it is necessary to know the radiation properties, in particular absorption, reflection and emission characteristics [9]. In the theoretical descriptions usually an absorption coefficient is introduced which is rather a free parameter. In the case of blackbody radiation, these properties are well established. However, in practice one often has to deal with surfaces that do not behave like perfect blackbodies.

One of the fundamental laws of thermal radiation theory is Kirchhoff's law. This law expresses the relation between the emission and absorption of energy for a non-transmitting material. If the incoming hemispherical radiation is uniformly polarized and uniformly distributed over all angles, absorbance is equal to emittance. In that case, only one radiation property is actually independent. The emittance is defined by the ratio between the emitted energy of a surface and the emitted energy of a blackbody at the same wavelength and temperature. For metals, the monochromatic emittance decreases as a function of wavelength, whereas for insulators there is a tendency to increase. The aforementioned radiation properties concern energy exchange with a complete hemispherical space

above the surface. Radiation properties also exhibit an angular dependence and therefore the intensity is considered within a small solid angle $d\omega$.

In general different surface preparation techniques are applied for laser processing in order to maximize the absorption of the laser beam. For metals, this is necessary due to the relatively poor absorption of radiation. The main concern in measuring temperature with an optical monochromatic pyrometer is to be familiar with the emissivity of the different surface conditions of the specimen. Therefore, emittance measurements are usually performed in advance of the final temperature measurements during laser processing. In practice, the surface preparation consists of increasing the roughness and/or painting the surface in order to approximate a blackbody. Coarsening is realized by using sandpaper or by sand blasting. Painting is also done using a carbon spray as used in this study.

To know the absorbed amount of energy it is necessary to study the interaction of the laser beam with the specimen [10]. In case of an optically smooth surface, electro-magnetic theory predicts the monochromatic reflection in the specular direction. The description of the optical phenomena is different for metals and ceramics [11]. In our experiments titanium is used as material. Whereas in vacuum the refractive index n equals 1, it becomes equal to $n + ik$ for metals. The factor n represents the refraction index and k the extinction coefficient. When an incident wave arrives at the surface, it splits into a reflected and a transmitted wave. The specular reflection can be derived, by imposing the boundary conditions for the electromagnetic field at both sides of the interface. In case of normal incidence the normal specular reflectance for an optically smooth surface is given by [12]

$$R_0 = \frac{(n-1)^2 + k^2}{(n+1)^2 + k^2} \tag{3.1}$$

As this degree of smoothness is rarely achieved, a modification is required to compensate for the surface roughness. In order to get some idea of the influence of roughness, a surface is usually assumed to consist of planes of random size and shape, all aligned parallel to the mean surface level and located at random levels relative to the surface. In addition, the height distribution is considered to be Gaussian. In that case, the normal incidence at an isotropic opaque medium and for which results in the total reflectance is given by [13,14]

$$R = R_0\left[\exp-\left(\frac{4\pi\sigma}{\lambda}\right)^2 + \left(1-\exp-\left(\frac{4\pi\sigma}{\lambda}\right)^2\right)\left(1-\exp-\left(\frac{\pi^2\xi^2}{2\lambda}\right)^2\right)\right] \quad (3.2)$$

where σ is the root mean square (rms) roughness and ξ is the autocovariance length of the surface. The autocovariance is defined by the change of height as a function of the displacement in the plane parallel to the surface. The first term of Eq. (3.2) represents the specular reflection or the coherent reflection, whereby the second term represents the incoherent or diffuse reflection. As the wavelength of the CO_2 laser is a factor 10 higher than the wavelength of the YAG laser, the percentage of specular reflection will be much higher for the CO_2 laser than for YAG/Fiber. YAG/Fiber and CO_2 are used in this thesis.

When ground and sandblasted specimen are compared it can usually be concluded that the increased surface roughness considerably increases the absorption. Also the absorption is higher for the liquid state than for the solid state. The higher absorption can be explained by the disappearance of inter-band absorption upon melting [15]. In addition, it should be mentioned that the transition between solid and liquid states of Ti requires a certain amount of energy, represented by the latent heat. However, in the thesis we will avoid melting and only consider laser treatment without melting, i.e. lower than 1668 ^{o}C.

3.2 Temperature fields induced by heat sources

In this section, analytical solutions of the temperature field in a solid will be described that are induced by an instantaneous heat source of a laser. Subsequently, those influences of different energy distributions of the heat source will be examined as they correspond to the different types of lasers used in particular experiments. Because of the limited specimen size in practice, the influence of finite dimensions of the specimen will be incorporated into the solution by specific boundary conditions of zero heat flux. In addition, the effect of cooling will be incorporated into the model. This will be done for different sets of boundary conditions. In addition to the absolute temperatures, the temperature gradient also influences the final performance of the modified layer. Therefore, the cooling rate will also be discussed. Phase transformations and temperature-dependent physical properties will not be taken into account in detail. In this case numerical

methods have to be used as will be shown in Chapter 6. Parts of this work have been published earlier in review papers and MK theses [16,17,18].

Whenever a temperature gradient exists within a body, transport of energy takes place by means of heat transfer. There exist three distinct processes by which the transfer of heat occurs, namely conduction, convection and radiation. For temperature differences in a solid, the transport of heat is restricted mainly to conduction. The flow of heat in a rigid isotropic medium can be described by the heat conduction equation:

$$\nabla^2 T(\vec{r},t) = \frac{1}{\kappa}\frac{\partial T(\vec{r},t)}{\partial t} \tag{3.3}$$

where $T(\vec{r},t)$ is the temperature at position $\vec{r}$ at time *t*, and κ is the thermal diffusivity (=$K/\rho c_p$, K is the thermal conductivity, ρ is the density and c_p the specific heat, see appendices A, B and C). In order to solve the heat conduction equation, Green's functions will be utilized [19,20]. When applied in the field of heat conduction, the type of Green's function represents the temperature at a point (*x,y,z*) at time *t* due to an instantaneous point source of unity strength positioned at (*x',y',z'*) at time *t'*. Furthermore, the solid is supposed to be at zero temperature and the surface is at zero temperature. So, when we write *T* in the mathematical descriptions it stands for the *temperature difference, not for the absolute temperature!* The Green's function $G(|\vec{r}-\vec{r}'|, t-t')$ which satisfies the heat conduction equation is given by

$$G(|\vec{r}-\vec{r}'|, t-t') = \frac{1}{(4\pi\kappa(t-t'))^{3/2}} \exp\left(-\frac{|\vec{r}-\vec{r}'|^2}{4\kappa(t-t')}\right) \tag{3.4}$$

where t' < t. Further, $\lim_{t\to t'} G = 0$ at every point with the exception of the position of heat generation. In the event of the production of heat in the solid, e.g. by a laser which couples into the material at the surface layer, Eq. (3.3) can be replaced by a modified version with an additional term:

$$\frac{\partial T(\vec{r},t)}{\partial \tau} = \kappa \times \nabla^2 T(\vec{r},t) + \frac{\kappa \times Q}{K} \quad (\tau < t) \tag{3.5}$$

where *Q* describes the intensity distribution of the heat source, e.g. the power density of the laser beam P/A_0, with A_0 the area. The solution of the temperature field in an *infinite* solid due to the continuous heat source *Q* can

be obtained by the superposition in space of the fundamental solutions, represented by Eq.(3.4). Additionally, the heat source can be made continuous by integrating over the time interval where in between the heat is supplied. This results in the temperature field described by [19]

$$T(\vec{r},t) = \frac{\kappa}{K} \int_{0}^{t} \int_{-\infty}^{\infty} \int_{-\infty}^{\infty} \int_{-\infty}^{\infty} Q(\vec{r}',t')\, G(|\vec{r}-\vec{r}'|, t-t')\, \mathrm{d}x'\mathrm{d}y'\mathrm{d}z'\mathrm{d}t' \qquad (3.6)$$

Thus $T(\vec{r},t)$ gives the temperature (difference with respect to a reference) at time *t* and position $\vec{r}$ due to a continuous heat flux *Q* at time *t'* and position $\vec{r}$. Further, the fundamental solution $G(|\vec{r}-\vec{r}'|, t-t')$ can be split up for the different coordinate directions. In Appendix A the complete solution of the heat conduction equation is derived, including the initial surface temperature and an initial body temperature.

So far we have summarized the fundamental solution of the heat conduction equation for a stationary heat source. The moving heat source can be introduced by formulating a moving medium relative to a fixed source, which is described in more detail by Rosenthal [21]. This method implies that the source distribution *Q* does not become time dependent, *but the observer position does*. When the source is assumed to move along the *x*-direction in reality, the transformation towards a moving medium can be realized by defining the *x*-component as $x+\nu(t-t')$. As a consequence, the *x*-component of the temperature field is defined by

$$G(x) = \frac{1}{(4\pi\kappa(t-t'))^{1/2}} \exp\left(-\frac{(x+\nu(t-t')-x)^2}{4\kappa(t-t')}\right) \qquad (3.7)$$

The most convenient way to visualize the absorbed laser power is by an internal heat source. Furthermore, the heat is assumed to be generated within an infinitesimally thin surface layer. In this section different heat sources will be examined for the case in which the medium is infinite. First the different sources are assumed to be time independent, which corresponds to the continuous wave type of laser.

Point source: The most straightforward way to define an energy distribution is by means of a point source *Q*. At $\vec{r}'=0$ the distribution is given by $Q(\vec{r}') = (P/A_0)\,\delta(\vec{r}')$, whereby *P* is the generated power. Substitution of the source in Eq. (3.6) results in the temperature profile described by:

$$T(\vec{r}) = \frac{P}{2\pi Kr} exp\left(-\frac{v(r+x)}{2\kappa}\right) \tag{3.8}$$

where r is the radial distance from the point source. The temperature distribution is formulated in a coordinate system fixed to the source [22]. At r=0, $T(\vec{r})$ becomes infinite, which is of course not the actual distribution of a temperature field in reality. From Eq. (3.8) it can be seen that the exponential term including velocity v causes a radially symmetrical exponential decrease of temperature with increasing v, but an asymmetrical temperature change in the direction of movement. Fig. 3.1 depicts the temperature profile for a point source calculated for semi-infinite block of Ti.

Gaussian energy distribution: The more realistic representation of the heat source is given by the Gaussian energy distribution.

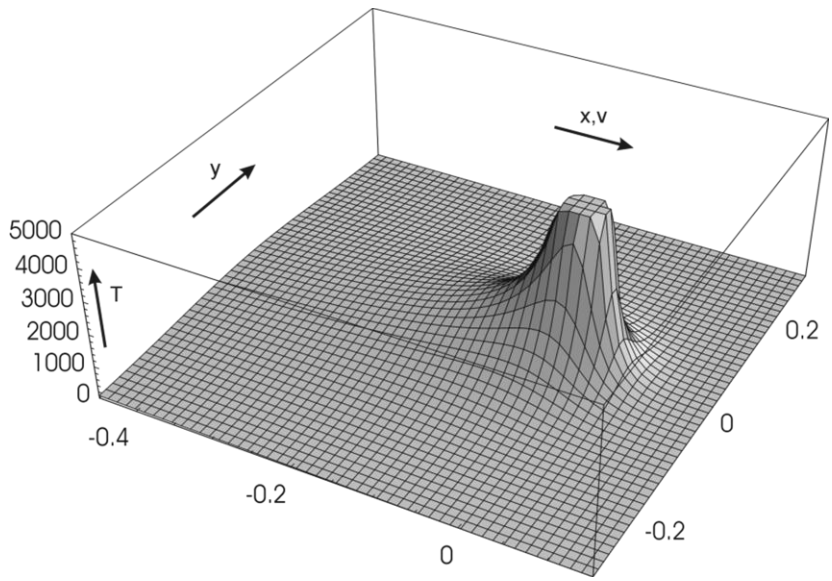

Fig. 3.1: Profile of the calculated temperature rise at z=0 for a point source. The absorbed laser power and scan velocity amounts to 500 W and 20 mm/s, respectively. For the substrate the thermophysical properties of Ti are used.

In contrast to the point source, there is no longer a singularity at $\vec{r}' = 0$. In practice, this distribution corresponds with the TEM_{00} mode for laser processing. If the total amount of absorbed power is P, then the energy distribution is described by

$$Q(\vec{r}') = \frac{P}{2\pi\rho^2}\exp\left(-\frac{x'^2+y'^2}{2\rho^2}\right) \qquad -\infty < x', y' < \infty \tag{3.9}$$

where ρ is the radius at which the Gaussian distribution has dropped to *1/e* of its peak value. Substitution of the distribution function in Eq. (3.6) and integrating over x',y',z' from $-\infty$ to ∞ yields

$$T(\vec{r},t) = \frac{AP\kappa}{4\pi K}\int_0^t \frac{(2\kappa(t-t')+\rho^2)^{-1}}{\sqrt{4\pi\kappa(t-t')}}\exp\left(-\frac{(x+v(t-t'))^2+y^2}{4\kappa(t-t')+2\rho^2}-\frac{z^2}{4\kappa(t-t')}\right)dt' \tag{3.10}$$

where A is the absorptivity. It can be seen that at a large distance from the heat source the temperature fields of point source and Gaussian beam will coincide (see also Section 3.4). In the near field, whereby the point source idealization fails, the temperature field is expected to be modulated by the Gaussian distribution. Fig. 3.2 depicts the temperature profile for a Gaussian intensity distribution of the heat source. The solution given in Eq. (3.10) is given for infinite beam size. If the size of the beam is finite, the solution will be modified as described in Appendix B.

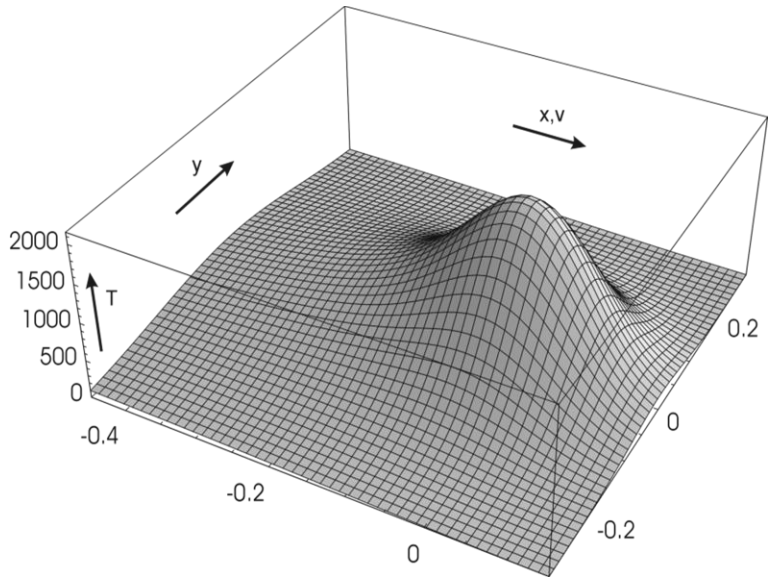

Fig. 3.2: Profile of the calculated temperature at z=0 for a Gaussian intensity distribution of the laser beam. The applied laser power and scan velocity amounts to 500 W and 20 mm/s, respectively. For the substrate the thermophysical properties of Ti are used.

Homogeneous energy distribution: Another realistic representation of the heat source is the homogeneous energy distribution. In laser applications this can be achieved by making use of beam integrators or by transport of the beam through fibers. If we assume the shape of the beam to be rectangular and the amount of absorbed power to be *P*, the intensity distribution is described by

$$Q(\vec{r}\,') = \frac{P}{4\rho_1\rho_2} \quad where - \rho_1 < x' < \rho_1 \ , - \rho_2 < y' < \rho_2 \tag{3.11}$$

where $2\rho_1$ and $2\rho_2$ are the length and the width of the beam, respectively. The source term has to be integrated only over its finite dimensions. Substitution of the energy distribution in Eq. (3.6) results in the temperature field given by

$$T(\vec{r},t) = \frac{AP\kappa}{8K\rho_1\rho_2} \int_0^t \frac{\mathrm{d}t'}{(\sqrt{4\pi\,\kappa\,(t-t')}} F(x)\,F(y) \exp\,(-\frac{z^2}{4\kappa\,(t-t')})dt' \tag{3.12}$$

where

$$F(x) = erf\ (\frac{x + v(t-t') + \rho_1}{\sqrt{4\kappa\,(t-t')}}) - erf\ (\frac{x + v(t-t') - \rho_1}{\sqrt{4\kappa\,(t-t')}}) \tag{3.13}$$

and

$$F(y) = erf\ (\frac{y + \rho_2}{\sqrt{4\kappa\,(t-t')}}) - erf\ (\frac{y - \rho_2}{\sqrt{4\kappa\,(t-t')}}) \tag{3.14}$$

Fig. 3.3 depicts the temperature profile for a heat source with a homogeneous intensity distribution.

Multiple passes: In most practical applications the laser treatment is not confined to single tracks. In order to modify a surface area, overlapping tracks are made. If the time between successive tracks is small, there already exists a temperature profile caused by the preceding laser track. Mathematically this can be described by a second source at a distance Δx and Δy removed from the first one. This can be done several times in the case of multiple tracks. Note that the time between successive tracks can be controlled by the distance Δx.

This method can be incorporated into the model by changing the source distribution for the Gaussian intensity distribution by

$$Q(x',y') = \frac{P}{2\pi\rho^2}\sum_m \exp\left[-\frac{\left(x'-(m-1)\Delta x\right)^2+\left(y'-(m-1)\Delta y\right)^2}{2\rho^2}\right] \quad (3.15)$$

Finite medium: This is the description given so far for the semi-infinite body. However, for industrial laser applications this situation is not realistic in many cases. Therefore, it should be worthwhile to make the influence of finite dimensions of the specimen visible. This can be done by making use of image sources [19].

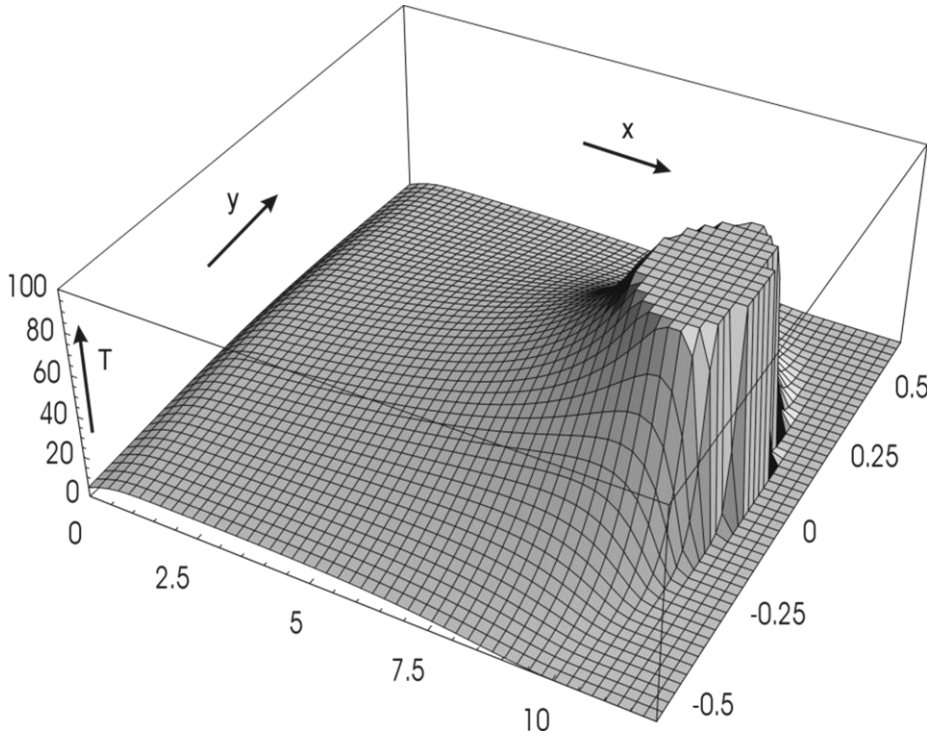

Fig. 3.3: Profile of the calculated temperature at z=0 for homogeneous intensity distribution of the laser beam. The applied laser power and scan velocity amounts to 550 W and 60 mm/s, respectively. For the substrate, the thermophysical properties of Ti are used.

Imagine that a point source scans with a velocity v in the *x*-direction of the specimen. In the *x*-direction the specimen is assumed to be infinite. The height of the sample amounts to *d* and in the *y*-direction the size amounts to

R_1+R_2, representing the distance between the source and the boundaries in the positive and negative *y*-direction, respectively. Starting from the fundamental solution, the temperature field, represented by Green's functions, has to be found for all directions. The temperature field in the *x*-direction is given by Eq.(3.7). In order to fulfil the boundary conditions in the *y*- and *z*-directions, multiple image sources are introduced. Fig. 3.4 illustrates the positioning of the imaginary sources.

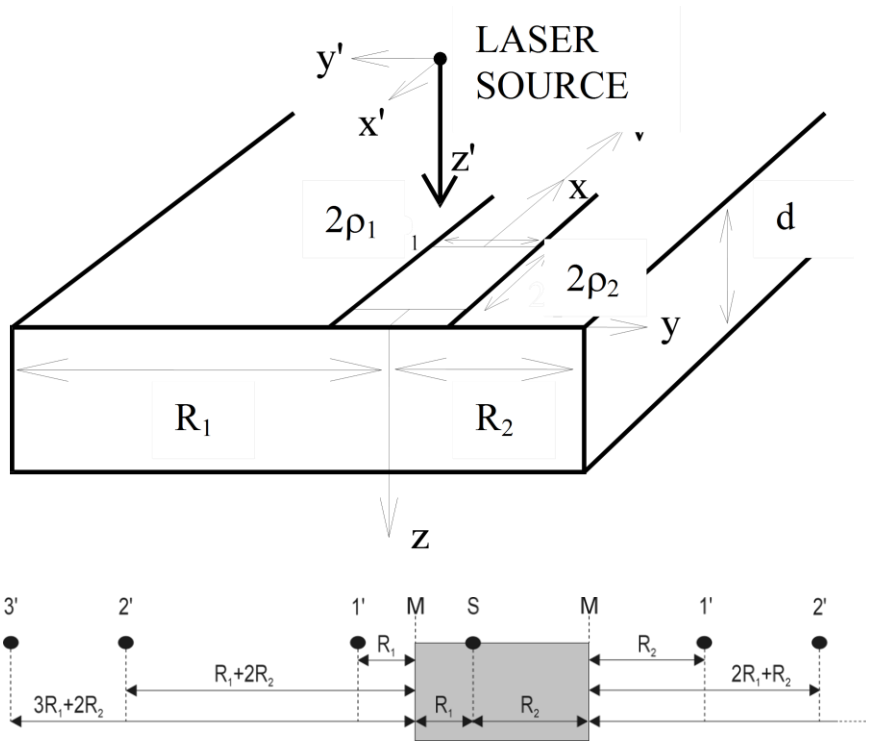

Fig. 3.4: Construction of image sources in the y-direction to fulfil zero heat flux at the boundaries of the specimen. The heat source interacts with the specimen at point S. The edges of the specimen act as mirror planes.

To provide zero heat flux, the image sources are positioned at $-2R_1$ and $2R_2$. However, these sources provide a heat flux at the opposite boundary. Therefore additional heat sources are required to cancel this out. When required, a sequence of image sources can be applied. As a result, the temperature field in the *y*-direction can be described by

$$G(y)=\frac{1}{\sqrt{4\pi\,\kappa(t-t')}}\Big[\sum_{n=-\infty}^{\infty}\exp\Big(-\frac{(y-y'-2n(R_1+R_2)^2}{4\kappa\,(t-t')}\Big)+\sum_{n=1}^{\infty}\exp\Big(-\frac{(y-y'-2nR_2-2(n-1)R_1)^2}{4\kappa\,(t-t')}\Big)+\sum_{n=1}^{\infty}\exp\Big(-\frac{(y-y'+2nR_1+2(n-1)R_2)^2}{4\kappa\,(t-t')}\Big)\Big] \tag{3.16}$$

In the *z*-direction the image sources are used as in the aforementioned method, which results in a temperature field in the *z*-direction

$$G(z)=\frac{1}{\sqrt{4\pi\,\kappa\,(t-t')}}\sum_{n=-\infty}^{\infty}\exp\Big(-\frac{(z-2nd)^2}{4\kappa\,(t-t')}\Big) \tag{3.17}$$

In Appendix B the complete solution of the temperature field is given for a Gaussian intensity distribution of the heat source, including the use of image sources to set the appropriate boundary conditions. Subsequently, the questions as to when it is necessary to use the image sources and how many are required will be asked. In principle, this is determined by the size of the specimen and the physical properties of the material. Therefore, a criterion should be formulated for the use of image sources that will be treated on the basis of two materials with completely different thermal conductivities. In our experimental part (Chapter 5, 6 and 7) finite size effects do not play a predominant role.

Heat loss: In the model so far the boundary conditions impose zero heat flux. In reality, energy transfer occurs at the surface due to temperature differences with surrounding media. For laser processing, the energy transfer takes place via different phenomena. If the specimen is in direct contact with a heat sink, conductive cooling takes place at $z=d$. As a consequence of the shielding gas, convective cooling, that is, Newtonian cooling, takes place at $z=0$. Furthermore, heat transfer also takes place by radiation at $z=0$, in accordance with the Stefan-Boltzmann law. In order to take into account the different kinds of heat transfer, an adaptation is made to the model.

To show effects of cooling, in our description, only cooling in the *z*-direction will be taken into account at $z=0$. When starting from the temperature field in the *z*-direction as given by Eq. (3.17), followed by the Laplacian transform, the transfer of heat can be incorporated by including an extra term in the following way:

$$\bar{G}_z = \frac{1}{2\sqrt{\kappa q}} \exp\left(-\sqrt{\frac{qz^2}{\kappa}}\right) + A\exp\left(-\sqrt{\frac{qz^2}{\kappa}}\right) \tag{3.18}$$

where A is a constant that can be determined by the boundary condition. If the transfer of heat is supposed to be linearly dependent on the temperature difference over the surface, the boundary condition can be represented by

$$\frac{dG}{dz} = \xi G \tag{3.19}$$

and

$$T_{corr}(\vec{r},t) = -\frac{\xi\kappa}{K}\int_0^\infty \exp\left[\xi z + \kappa\xi^2(t-t')\right] erf\left[\frac{z}{2\sqrt{\kappa(t-t')}} + \xi\sqrt{\kappa(t-t')}\right]$$
$$\int_0^\infty\int_0^\infty \frac{1}{4\pi\kappa(t-t')} \exp\left[\frac{(x+v(t-t')-x')^2+(y-y')^2}{4\kappa(t-t')}\right] Q(x',y')dx'dy'dt' \tag{3.20}$$

where $\xi=h/K$, with h representing the heat transfer coefficient and K the thermal conductivity. After performing the Laplace transform on the boundary condition and substitution of Eq. (3.18), the solution of the modified temperature field can be obtained. In fact, the former solution of the temperature field is extended by a temperature correction term represented [14] as shown in Eq. (3.20).

In reality, the description of the physical processes, corresponding to the different ways heat transfer occurs, often exhibits a non-linear temperature dependency. Where the transfer takes place by radiation, it depends on the fourth power of the temperature (Stefan's law). However, for convective cooling at $z=0$ caused by the shielding gas, the linear temperature dependency is a satisfactory approximation.

So far, the derivation of the temperature correction takes into account only the boundary condition at $z=0$. The boundary condition at $z=d$ can be incorporated simultaneously, by introducing an extra term with pre-factor B in Eq. (3.18). Furthermore, the use of image sources also can be included whereby the inverse Laplacian transformation becomes rather complex. A

disadvantage of the aforementioned description method is that factors *A* and *B* do not represent any physical property. Therefore, a different approach is used in which a representative cooling factor arises that has a more physical meaning.

First, we introduce the so-called Biot number [23]. In the general transient heat conduction formulations as put forward in the previous section, the temperature field varies *both with time t and position* $\vec{r}$. However, in various engineering applications, temperature variations within the materials can be neglected and the temperature is considered to be a function of only time *t*. Such assumptions are made in the so-called *lumped system formulation*. In order to provide some criteria for the range of validity, the internal thermal resistance is considered versus the external resistance. The former is described by *L/(K A)*, whereas the latter is equal to *1/(h A)* (*L*= characteristic length and *h* is the heat transfer coefficient). The ratio of the internal thermal resistance versus the external resistance is called the Biot number

$$B = \frac{hL}{K} \tag{3.21}$$

If the internal thermal resistance is small, i.e. the thermal conductivity is high, the temperature distribution remains sufficiently uniform during transients, that is, *B* is small and the lumped system formulation is valid. This formulation is applicable in most engineering systems if $B \le 0.1$. Now let us consider the solution of a homogeneous boundary value problem of heat conduction of a finite slab $(0 \le z \le L)$ initially at a temperature $T(\vec{r})$ that dissipates heat for times $t > 0$ into an environment at zero temperature (we are interested only in the temperature change). The mathematical formulation is described by Eqs. (3.3) and (3.5) with the boundary conditions

$$-K_1 \frac{\partial T}{\partial z} + h_1 T = 0 (z = 0, t \ge 0);$$

$$+K_2 \frac{\partial T}{\partial z} + h_2 T = 0 (z = L, t \ge 0);$$

and

$$T = T(\vec{r}) (\, for..t = 0..in..0 \le z \le L);$$

(3.22)/(3.23) /(3.24)

If the system dissipates heat at the boundary $z=L$ by convection or conduction and the boundary at $z=0$ is kept insulated, Green's function can be derived [24]:

$$G(|z-z'|,t-t') = \frac{2}{L}\sum_{m=1}^{\infty}\exp\left(\frac{-\beta_m^2\kappa(t-t')}{L^2}\right)\frac{\beta_m^2+B_2^2}{\beta_m^2+B_2^2+B_2}\cos(\beta_m\frac{z}{L})\cos(\beta_m\frac{z'}{L}) \tag{3.25}$$

where z' is the position of the heat source that operates at $t'>0$, κ is the thermal diffusivity, and the β_m values are the positive roots of

$$\beta_m \tan\beta_m = B_2 \tag{3.26}$$

with

$$B_2=h_2L/K \tag{3.27}$$

For $B_2 < 2$ the eigenvalues of Eq. (3.27) can be approximated by

$$\beta \approx \sqrt{3}\sqrt{\frac{B_2}{B_2+3}\left(1-\frac{B_2^2}{5(B_2+3)^2}\right)} \tag{3.28}$$

If the system dissipates heat by convection/radiation both at $z=0$ and $z=L$, Green's function can be derived by solving a special case of the Sturm-Liouville equation, as described in Appendix C.

Cooling rate: After the laser beam has passed, the cooling rate influences the final structure in several ways. First, the structure will change as a function of the rate. If we are in the melting regime near the solidification temperature the stability of the solidification front is directly related to the cooling rate. For high cooling rates the liquid may be undercooled, resulting in the formation of protrusions at the solidification front. These protrusions will develop as cellular or dendritic structures depending on the cooling rate. Besides, when during cooling down a phase transition takes place, the rate determines the degree of diffusion during this transition. For example, for titanium a martensitic phase transformation takes place only from the β to the α phase for high cooling rates. Secondly, the cooling rates determine the thermal stresses, which are induced in the layer. These could result in crack formation

when exceeding a critical stress state. Therefore, it is very important to get insight into cooling rates during laser processing.

In principle, the cooling rate is related to the temperature gradient in the direction of motion (multiplied by the velocity of the solidification front in case of the molten zone). In case of melting and if the velocity of the resolidification front is assumed to be equal to the laser scan velocity, the cooling rate is defined by

$$\frac{\partial T}{\partial t} = -v_l \frac{\partial T}{\partial x} \tag{3.29}$$

For most intensity distributions of the heat source it is rather complicated or impossible to obtain an analytical expression for the temperature gradient. As a consequence, the gradient has to be determined numerically. However, for one specific situation it is possible to derive an analytical expression. In case the observer is far removed from the center of the beam, an analytical expression for the derivative of the temperature field can be obtained for the point source.

Differentiation of Eq. (3.8) yields a temperature gradient defined by

$$\frac{\partial T}{\partial t} = -v_l \left[\frac{x}{r^2} + \frac{v}{2\kappa}\left(1 + \frac{x}{r}\right)\right] T \tag{3.30}$$

In our experiments the heating rate was approximately 2000 – 2700 °C/s and a cooling rate of approximately 1300 °C/s at the offset of the laser beam path (see Chapter 5).

3.3 Laser forming

In laser treatment of materials we basically have two external, extrinsic parameters to vary, i.e. power or power density and interaction time, e.g. laser dwell times or laser beam velocities. For that reason it is relevant to know how ‘laser forming’ depends on these two controlling parameters. In the experimental work, as will be shown in Chapters 4 to 6, we have concentrated on the bending of plates due to the movement (in one dimension) of a fast laser beam several times over the surface of a plate.

Bending can only occur due to gradients in the stress fields over thickness. Suppose we melt a plate along a laser track over the whole thickness and the metal in the track resolidifies, then tensile stresses will be set up near the surfaces on both sides, compensated by compressive stresses inside the bulk (otherwise the material will distort) but the situation in that case is still symmetrical. As a consequence stress fields are present but no resultant gradient and therefore the plate will not bend.

In our experiments we do not melt the material but heat treat the surface on one side *below melting point*. One of the reasons to do it in this manner was to see whether we could detect contributions to the bending moment due to the phase transition, which occurs in Ti below its melting point. The crystal structure of Ti at ambient temperature and pressure is hexagonal close-packed, called α, but at about 1163 K, Ti undergoes an allotropic transformation to body-centered cubic (β phase). The β phase remains stable up to the melting point of pure Ti of 1943 K. It can be tacitly assumed that the hcp-bcc phase transformation generates internal stresses and the question is whether the residual stress fields could also assist the bending phenomenon and bending rate in a positive sense.

Therefore, the next question is where these stress fields, setting up the bending moment, are coming from. The answer is simply: they are generated by the gradient in temperature over thickness by the passing laser beam. Obviously the interaction time matters and therefore we expect a strong influence of the laser beam velocity depending on the thermo-physical properties, such as thermal conductivity of the materials itself.

From a physics point of view and in a qualitative sense, we can argue as follows for the bending angle α_b : Taking linear elasticity as a starting point, a stress gradient $\partial\sigma$ can be converted to a gradient in thermal strain $\partial\varepsilon$ as a result of a temperature gradient ∂T:

$$\alpha_b \propto \delta\sigma \propto \delta\varepsilon \propto \delta T \tag{3.31}$$

As a consequence, the temperature gradient can be written as the product of heat density input, i.e., the heat input per unit area, and the heat resistance, which is nothing else than the thermal diffusion length l over the thermal conductivity K, i.e. a higher thermal conductivity means a lower heat resistance. With phonons as the crucial carriers of heat transport in metallic systems the thermal diffusion length is, in a first approximation, proportional to the square root of the product of thermal diffusivity and interaction/dwell

time τ involved. The latter is inversely proportional to the laser beam velocity v_l .

Besides the linear proportionality to the heat resistance the temperature gradient ∂T depends linearly on the heat density Q (see Eq. (3.9), i.e. the heat input by laser power P over the area.

In summary: the bending angle α_b becomes inversely proportional to the square root of the laser beam velocity v_l , and linearly proportional to the heat density or laser power P at constant area, i.e.:

$$\alpha_b \propto \delta\sigma \propto \delta\varepsilon \propto \delta T \propto \frac{Ql}{K} \propto P\sqrt{\kappa\tau_l} \propto \frac{P}{\sqrt{v_l}} \tag{3.32}$$

From a mathematical point of view, details of the temperature field of a moving heat source matter and indeed they can be described in a more sophisticated way based on solving the differential equations of heat conduction using the framework laid down in Section 3.2.

The starting point here is the basics of Eq. (3.5), Eq. (3.6) and Eq. (B.5) for a Gaussian energy distribution. Suppose the laser beam is moving at a velocity in the x-direction. If the velocity is relatively high we can treat the laser beam as a line source, with finite width in the y-direction and infinitesimally thin in the x-direction.

The advantage of this approximation is that an analytical solution is available for Eq. (3.5) and Eq. (3.6):

$$\delta T = \frac{P / v_l}{2\pi K\sqrt{t(t+t_0)}} \exp\left[-\frac{1}{4\kappa}\left(\frac{(z+z_0)^2}{t} + \frac{y}{t+t_0}\right)\right] \tag{3.33}$$

The new parameter t_o is the time taken for the heat $QA=P$ to diffuse over the beam half-width, r_b ,i.e.

$$t_0 = \frac{r_b}{4\kappa} \tag{3.34}$$

The temperature difference involving the peak temperature for $t>>t_o$ can be expressed as

$$\delta T = \frac{2P / v_l}{e\pi\rho c_p \left[\left(z + z_0 \right)^2 + y^2 \right]} \tag{3.35}$$

where ρ is the density, c_p the specific heat and κ is the thermal diffusivity (=$K/\rho c_p$, K is the thermal conductivity, see Appendices A, B and C). For y=0 and $z >> z_0$ Eq. (3.35) reduces to the point source moving over the surface as described by the Rosenthal equation [18]. z_0 is the distance away from the laser beam (an image source above the surface in order to avoid temperature singularities at the surface as was observed in Fig. 3.4 and Eq. (3.17)).

Eq. (3.35) is valid for $z^2 + y^2 \gg r_b^2$ where z is the distance away from the laser beam. With z_0 being the distance relatively far away from the laser beam, it follows that

$$z_o^2 = \frac{r_b}{e}\sqrt{\frac{\pi\kappa r_b}{v_l}} \tag{3.36}$$

The following proportionality then holds for the maximum temperature gradient:

$$\partial T \propto \frac{P}{v_l}\frac{1}{z_0^2} = \frac{P}{v_l}\sqrt{\frac{v_l}{\pi\kappa r_b}}\frac{e}{r_b} \tag{3.37}$$

thus implying that the bending angle is directly proportional to the inverse of the square root of the scanning velocity of the laser beam through the maximum temperature difference, i.e.

$$\alpha_b \propto \partial T \propto \frac{P}{\sqrt{v_l}} \tag{3.38}$$

leading to the same conclusion as derived on qualitative arguments earlier in Eq. (3.32).

It should be realized that usually the cooling down curve is the most important trajectory for the generation of bending stresses, i.e. the shrinkage will lead to the onset of bending or shape change of the substrate. Experimentally the thermal gradient is usually not a constant along the thickness of the substrate due to movement of the laser (see also discussion in Chapter 5, Section 5.2.7.).

Although we prefer analytical solutions to understand the effects of the various controlling parameters in the laser forming processing routes, insight of the heat flow within the material is also advancing through finite-element numerical calculations. In Chapter 6, 3D time dependent FEM results are presented and discussed using COMSOL Multiphysics, a commercially available computer software code.

3.4 Appendices

Appendix A

In this Appendix we follow for the sake of comparison the notation introduced by Carslaw and Jaeger [19], that is, Green's function is denoted by *u* and the temperature (difference with respect to a reference) by *v*. If the internal and surface temperatures are both equal to zero, the solution of the heat conduction equation is represented by

$$u\left(\left|\vec{r}-\vec{r}'\right|,t-t'\right)=\frac{1}{8\left[\pi\kappa(t-t')\right]^{3/2}}\exp\left[-\frac{(x-x')^2+(y-y')^2+(z-z')^2}{4\kappa(t-t')}\right] \tag{A.1}$$

In the limit for $t \rightarrow t'$, this solution is equal to zero with the exception at point (x',y',z'). Subsequently, the solution of the heat conduction equation will be derived when there is an initial temperature $v_i(x,y,z)$ and a surface temperature $v_s(x,y,z)$. Additionally, the heat generated in the body will also be taken into account. For this situation the heat conduction equation is given by

$$\frac{\partial v}{\partial t'}=\kappa\nabla^2 v+\frac{\kappa Q(\vec{r},t)}{K} \tag{A.2}$$

where v represents the solution of the temperature field for this situation. Combination of Eq. (A.2) and (3.3) yields the following expression

$$\frac{\partial(uv)}{\partial t'}=u\frac{\partial v}{\partial t'}+v\frac{\partial u}{\partial t'}=\kappa\left[u\nabla^2 v+\frac{Q}{K}u+v\nabla^2 u\right] \tag{A.3}$$

By integrating over the three dimensions x',y',z' and time t' at the interval from 0 up to $t-\varepsilon$ the following expression can be derived

$$\int_0^{t-\varepsilon}\left[\iiint\frac{\partial(uv)}{\partial t'}dx'dy'dz'\right]dt'=\kappa\times\int_0^{t-\varepsilon}\left[\iiint(u\nabla^2 v+\frac{Q}{K}u+v\nabla^2 u)dx'dy'dz'\right]dt' \tag{A.4}$$

In order to obtain an expression for the temperature field v, both sides of equation will first be manipulated.

Left side
Changing the order of integration yields:

$$\int\int\int (uv)_{t'=t-\varepsilon} dx'dy'dz' - \int\int\int (uv)_{t'=0} dx'dy'dz' \tag{A.5}$$

Taking into account that the point source is acting at x',y',z', Eq. (A.5) can be rewritten for the limit $\varepsilon \to 0$ by

$$[v]_t - \iiint (uv)_{t'=0} dx'dy'dz' \tag{A.6}$$

Right side
By applying Green's Theorem on the right hand side of Eq. (A.4), the following expression is obtained

$$\kappa \int_0^{t-\varepsilon} \left[\int\int \left(u\frac{\partial v}{\partial n} - v\frac{\partial u}{\partial n} \right) dS + \int\int\int \frac{Q}{K} u dx'dy'dz' \right] dt' \tag{A.7}$$

The integral is changed from a volume integral to a surface integral. As u vanishes at the surface the first term of the surface integral falls away. The total solution of the temperature field v is given by

$$[v]_t = \int\int\int u_{t'=0} v_{t'=0} dx'dy'dz' + \kappa \int_0^{t-\varepsilon} \left[-\int\int v\frac{\partial u}{\partial n} dS + \int\int\int \frac{Q}{K} u dx'dy'dz' \right] dt' \tag{A.8}$$

where $v_{t'=0}=T_i(x',y',z')$ and v at the surface is given by $T_s(x',y',z')$. With the use of Eq. (A.8), the solution of the temperature field can be obtained for *any initial condition and any type of heat source*. In case special boundary conditions are involved, the appropriate Green's function can be obtained by making use of the Laplacian transformation.

Appendix B

When the intensity distribution of the heat source has finite dimensions the analytical expression for the temperature field becomes increasingly complicated. This can be illustrated by substitution of the Gaussian energy distribution in the general solution of the temperature field, represented by Eq. (3.6). As in the previous appendix we follow here the notation for the Green's function introduced by Carslaw and Jaeger [19], that is, the Green's function is denoted by *u*. When we confine ourselves to the direction of movement, the following integral has to be solved:

$$\int_{-b}^{b} u\left(\left|x-x'\right|,t-t'\right)Q(x')dx' \cong \frac{1}{\sqrt{4\pi\kappa(t-t')}}\int_{-b}^{b}\exp\left(-\frac{x'^2}{2\rho^2}-\frac{(x+v(t-t')-x')^2}{4\kappa(t-t')}\right)dx' \tag{B.1}$$

After some mathematical manipulation the solution can be expressed with the use of Error Functions. If we assume the radius of the beam (*b*) to be equal to 2ρ, the solution is given by

$$\frac{\rho}{2\sqrt{2\kappa(t-t')+\rho^2}}\left[erf\left\{W\left(2-\frac{\rho(x-v(t-t'))}{2\kappa(t-t')+\rho^2}\right)\right\}-erf\left\{W\left(-2-\frac{\rho(x-v(t-t'))}{2\kappa(t-t')+\rho^2}\right)\right\}\right] \tag{B.2}$$

and *W* is defined as

$$W=\sqrt{\frac{2\kappa(t-t')+\rho^2}{4\kappa(t-t')}} \tag{B.3}$$

In a similar way the solution for the *y*-direction can be obtained. By substitution in Eq. (3.6), the total solution can be acquired. Finally, Eq. (B.4) describes the temperature field for Gaussian heat sources, inclusive image sources, with the temperature (difference) $v[x,y,z,t]=T\left[x,y,z,t\right]$:

$$T[x,y,z,t]=\frac{AP\kappa}{4\pi K}\int_0^t dt'\left[\frac{\left(2\kappa(t-t')+\rho^2\right)^{-1}}{\sqrt{4\pi\kappa(t-t')}}\sum_{n=-\infty}^{\infty}\exp\left(-\frac{\left(z-2nd\right)^2}{4\pi\kappa(t-t')}\right)\right]*$$

$$\sum_{n=-\infty}^{\infty}\exp\left[-\frac{(x+v(t-t'))^2+(y-2n(R_1+R_2))^2}{4\kappa(t-t')+2\rho^2}\right]F_y^{(1)}F_x+$$

$$\sum_{n=-\infty}^{\infty}\exp\left[-\frac{(x+v(t-t'))^2+(y-2nR_2-2(n-1)R_1)^2}{4\kappa(t-t')+2\rho^2}\right]F_y^{(2)}F_x+$$

$$\sum_{n=-\infty}^{\infty}\exp\left[-\frac{(x+v(t-t'))^2+(y+2nR_1+2(n-1)R_2)^2}{4\kappa(t-t')+2\rho^2}\right]F_y^{(3)}F_x$$

(B.4)

where the functions F are defined by:

$$F_x=erf\left[W\left(2-\frac{\rho(x-v(t-t'))}{2\kappa(t-t')+\rho^2}\right)\right]-erf\left[W\left(-2-\frac{\rho(x-v(t-t'))}{2\kappa(t-t')+\rho^2}\right)\right]$$

$$F_y^{(1)}=erf\left[W\left(2-\frac{\rho(y-2n(R_1+R_2))}{2\kappa(t-t')+\rho^2}\right)\right]-erf\left[W\left(-2-\frac{\rho(y-2n(R_1+R_2))}{2\kappa(t-t')+\rho^2}\right)\right]$$

$$F_y^{(2)}=erf\left[W\left(2-\frac{\rho(y-2nR_2-2(n-1)R_1)}{2\kappa(t-t')+\rho^2}\right)\right]-erf\left[W\left(-2-\frac{\rho(y-2nR_2-2(n-1)R_1)}{2\kappa(t-t')+\rho^2}\right)\right]$$

$$F_y^{(3)}=erf\left[W\left(2-\frac{\rho(y+2nR_1+2(n-1)R_2)}{2\kappa(t-t')+\rho^2}\right)\right]-erf\left[W\left(-2-\frac{\rho(y+2nR_1+2(n-1)R_2)}{2\kappa(t-t')+\rho^2}\right)\right]$$

(B.5)

Appendix C

For the solution of the homogeneous boundary-value problem of heat conduction for a slab, we assume a separation in the form

$$T(z,t) = F(z)\Gamma(t) \tag{C.1}$$

The solution for the function $\Gamma(t)$ is given as

$$\Gamma(t) = \exp\left(-\frac{\kappa\beta^2 t}{L^2}\right) \tag{C.2}$$

The space variable function *F(z)* satisfies the eigenvalue problem described in Eq. (3.3) and (3.23)-(25) and is actually a special case of the Sturm-Liouville problem:

$$\frac{d}{dx}\left[p(x)\frac{d\psi(\lambda,x)}{dx}\right] + \left[q(x) + \lambda\omega(x)\right]\psi(\lambda,x) = 0, \quad \text{for } a < x < b$$

$$A_1\frac{d\psi(\lambda,x)}{dx} + A_2\psi(\lambda,x) = 0, \quad \text{at} \quad x = a \tag{C.3}$$

$$B_1\frac{d\psi(\lambda,x)}{dx} + B_2\psi(\lambda,x) = 0, \quad \text{at} \quad x = b$$

with $p(x)=1$, $\omega(x)=1$, $q(x)=0$ and $\lambda=\beta^2$. Then the eigenfunctions $F(\beta_m,z)$ are orthogonal, that is

$$\int_0^L F(\beta_m,z)F(\beta_n,z)dz = 0 \text{ for } m \neq n \text{ and } N(\beta_m) \text{ for } m = n \tag{C.4}$$

The solution of the Eq. (C.3) is now constructed as

$$T(z,t) = \sum_{m=1}^{\infty} c_m F(\beta_m,z)\exp\left(-\frac{\kappa\beta_m^2 t}{L^2}\right) \tag{C.5}$$

where the norm is defined as

$$N(\beta_m) = \int_0^L \left[F(\beta_m, z)\right]^2 dz \tag{C.6}$$

The application of the initial condition gives

$$T(z,0) = \sum_{m=1}^{\infty} c_m F(\beta_m, z)$$

$$\text{with } c_m = \frac{1}{N(\beta_m)} \int_0^L F(\beta_m, z') T(z',0) dz' \tag{C.7}$$

Substitution of these equations into Eq. (C.5) yields the solution for the temperature *T(z,t)*

$$T(z,t) = \sum_{m=1}^{\infty} \frac{F(\beta_m, z)}{N(\beta_m)} \exp\left(-\frac{\kappa \beta_m^2 t}{L^2}\right) \int_0^L F(\beta_m, z') T(z',0) dz' \tag{C.8}$$

The eigenfunctions $F(\beta_m,z)$ of the eigenvalue problem are given as

$$LF(\beta_m, z) = \beta_m \cos(\beta_m \frac{z}{L}) + B_1 \sin(\beta_m \frac{z}{L}) \tag{C.9}$$

where the eigenvalues β_m are the roots of:

$$\tan \beta_m = \frac{\beta_m (B_1 + B_2)}{\beta_m^2 - B_1 B_2} \tag{C.10}$$

and the normalization $N(\beta_m)$ is given by:

$$N(\beta_m) = \frac{1}{2L}\left[\left(\beta_m^2 + B_1^2\right)\left(1 + \frac{B_2}{\beta_m^2 + B_2^2}\right) + B_1\right] \tag{C.11}$$

Substitution of Eq. (C.5) and Eq. (C.11) into Eq. (C.8) leads to Green's function formulation

$$u(|z-z'|,t-t') = \frac{2}{L}\sum_{m=1}^{\infty}\exp\left(-\frac{\beta_m^2\kappa(t-t')}{L^2}\right)\left[\beta_m\cos(\beta_m\frac{z}{L})+B_1\sin(\beta_m\frac{z}{L})\right]*$$

$$\frac{\left[\beta_m\cos(\beta_m\frac{z'}{L})+B_1\sin(\beta_m\frac{z'}{L})\right]}{(\beta_m^2+B_1^2)\left[1+B_2^2(\beta_m^2+B_2^2)^{-1}\right]+B_1} \qquad \text{(C.12)}$$

3.5 References

[1] M.Ignatiev, I. Smurov and G. Flamant, Meas. Sci. Technol., 5, 563 (1994).

[2] J .C. Ion, H.R. Shercliff and M.F. Ashby, Acta Metallurgica, 40 (7), 1539 (1992).

[3] W. Kurz and D.J. Fisher, Fundamentals of solidification, Trans Tech Publications, Switzerland, (1985).

[4] M.F. Ashby and K.E. Easterling, Acta Metallurgica, 32 (11), 1935 (1984).

[5] D.J. Johns, Thermal stress analysis, Pergamon Press Ltd., Oxford, (1965).

[6] J. Mathews and R.L. Walker, Mathematical methods of physics, Addison-Wesley, Reading, Ma, (1970).

[7] C.R. Darling, Pyrometry, Spon & Chamberlain, New York, (1920).

[8] I. Smurov and M. Ignatiev, NATO series E Appl. Sci., 307, 529 (1996).

[9] E.M. Sparrow and R.D. Cess, Radiation heat transfer, Wadsworth , California, (1966).

[10] M. von Allmen, Laser and electron beam processing of Materials, Academic Press, (1980).

[11] J.Th.M. De Hosson, X.B. Zhou, M. van den Burg, Acta Metallurgica et Materialia 40, S139-S142 (1992).

[12] A.V. Sokolov, Optical properties of metals, Blackie & Son, London and Glasgow, (1967).

[13] H.E. Benett and J.O. Porteus, J. of the Opt. Soc. of Am., 51, 123 (1961).

[14] J.O. Porteus, J. of the Opt. Soc. of Am., 53 (2), 1394 (1963).

[15] T.E. Faber, Theory of liquid metals, Cambridge Univ. Press, 309 (1972).

[16] J.Th.M. De Hosson, et al 'Structure and properties of heterophase interfaces', in: H.S. Nalwa (ed.), Handbook of Surfaces and Interfaces in Materials, Volume I, Amsterdam: Academic Press, 1999, chapter 1, pp.1-114.

[17] R.L.W.Popma, PhD Thesis, Sintering characteristics of nano-ceramics, University of Groningen,2002, 29-4-2002 .

[18] A.B. Kloosterman, PhD Thesis, Surface modification of Titanium with lasers, University of Groningen, 1998, 8-5-1998 .

[19] H.S. Carslaw and J.C. Jaeger, Conduction of heat in solids, Oxford University, 1959.

[20] E. Geissler and H.W. Bergmann, Laser Treatment of Materials, ed. B.L. Mordike, VDI Verlag, (1987). E. Geissler, PhD thesis, Un. Erlangen-Nürnberg, Germany, 1992.

[21] D. Rosenthal, Trans. of the A.S.M.E., 11, 849 (1946).

[22] H.E. Cline and T.R. Anthony, J. Appl. Phys., 48, 3895 (1977).

[23] F. Kreith, Principles of heat transfer, Harper & Row publishers, New York, (1973), and M. Necati Özişik, Heat Conductionr, Wiley, New Yoirk, second edition 1993.

[24] P.M. Morse and H.Feshbach, Methods of theoretical physics, McGraw-Hill, (1953), and J.V. Beck, K.D. Cole, A. Haji-Sheikh, B. Litkouhi, Heat conduction using Green's functions, Himishere Pub. Comp., London, 1992.

Chapter 4

Mechanical characterization of the effect of various forming processes applied to commercially pure titanium

4.1 Introduction

This chapter illustrates the effect of three forming processes on the mechanical properties of commercially pure titanium, i.e. laser forming, mechanical forming and a combination process consisting of a laser forming step followed by a mechanical forming step. All three processes produce specimens of a similar final radius of curvature. Evaluation of the samples includes residual stress measurements, fatigue testing, Charpy impact testing, micro hardness measurements and microstructure evaluation. All results were compared to the various forming methods in order to determine which method is more suitable for which type of loading condition i.e. impact loading or cyclic loading. Fatigue testing of components produced by these methods revealed that the laser forming process provided the best results when a high load was applied whereas at lower applied loads, the mechanical forming process showed the highest number of cycles to failure. Charpy impact testing done at room temperature and at a sub-zero temperature of −40°C revealed that the laser forming process negatively affected the toughness of the material. Residual stress measurements showed that the laser forming process resulted in the highest value of surface relieved residual stress values compared to the other two processes.

4.2 Forming processes applied to CP Ti

Titanium is mostly used in the aerospace industry due to its high specific strength and excellent corrosion resistance derived from its protective oxide film. Titanium and its alloys have been in use for more than fifty years in seawater and aggressive industrial environments (Titanium: A Technical Guide, [8]). Since its inception in the mid-1980's as a means of producing ship

hulls, the laser forming process (LF) has been studied in an effort to better understand the process mechanisms and its effect on the material performance [18,17]. LF makes use of a defocused laser beam to induce high thermal energy into a localized surface area of the material resulting in a controlled elastic–plastic distortion [21,20,22], for details reference is made to Chapter 3. Industrial sectors such as the aerospace, automotive, electronics and shipbuilding have shown much interest in this application because of process flexibility and automation capabilities [14]. The laser bending process as such on titanium and its alloys have been studied by many researchers and the difficulties associated with the process due to titanium's low thermal conductivity and resultant sluggish response to laser treatments have been documented [15,23,5,19].

This study lies within the framework of investigations which emanates from the long term vision of possibly using thinner gauge material (laser formed) for similar safety requirements when compared to mechanically formed counterparts. Previous investigations undertaken on a pearlitic–ferritic material showed enhancement of its mechanical properties and subsequent fatigue behavior [10,13]. The goal of this study is to investigate a similar enhancement in the mechanical properties and the process effects on commercially pure (CP) titanium (grade 2). This grade of titanium is mainly used for airframes, aircraft engines, marine chemical components, heat exchangers, condensing and evaporator tubing and has good formability, ductility, weldability and corrosion resistant characteristics (Titanium: A Technical Guide, [8]).

Another goal was to compare three different forming processes viz. laser forming (LF), mechanical forming (MF) and a combination of laser-mechanical forming (LMF) on the mechanical properties of titanium (grade 2). In addition, the process yielding the highest number of cycles to failure at high and low load settings is also determined.

4.2.1 Laser and mechanical forming setup

The 2D forming of the titanium plate samples (200 mm × 50 mm) was carried out using a 5 kW CO_2 Continuous Wave Trumpf laser system. Due to its long wavelength (10.6 μm) the sample surfaces were coated with a matt black spray (high temperature resistance) to ensure maximum heat absorptivity. Although burn-off is evident after the first scan, the irradiated surface remains sufficiently dark to prevent reflection of the laser beam. From previous reported work the fixed laser parameters chosen were: (i) the laser beam

diameter, (ii) the number of scans per location, (iii) the laser power, and (iv) interval spacing between consecutive laser lines [9], see Chapter 3 for details. An open mold was used whereby ten samples were positioned adjacent to one another. The gap between the samples being approximately 2 mm resulted in an irradiation length of approximately 520 mm. The sequence pattern of laser line scans was generated from bottom to top and again from top to bottom, as indicated schematically in Fig. 4.1. The 1st scan is indicated furthest to the left in Fig. 4.1. The 2nd scan was made furthest to the right, the 3rd scan was made adjacent to the 1st scan with a 50% overlap and the 4th scan was made to the left of the 2nd scan (also with a 50% overlap). This pattern was repeated until the final scan in the middle of the specimen.

The appearance of the formed samples after laser irradiation in the open mold setup is shown in Fig. 4.2. A number of forming trials were conducted in order to establish the optimum laser scanning velocity for producing a bend of approximately 120 mm radius of curvature. The final forming parameters chosen for the production of the samples were a laser power of 1.5 kW; laser beam diameter (spot size) of 12 mm; interval spacing of 6 mm; scanning velocity of 20 mm/s; and six consecutive laser scans per line. The resulting behavior of all samples was bending concave upwards towards the laser source. This behavior was observed repeatedly as shown in Fig. 4.2.

Mechanical forming (MF) was performed using a Rejva\Gosmeta mechanical bending press capable of a maximum force of 25 tons. The tool radius fitted to the mechanical press was 121.6 mm and that of the die radius was 118.4 mm. After setup of the mechanical press, the parent plate sample was inserted and fastened at each end to the fixture. After the mechanical press deformed the parent plate to a radius of approximately 120 mm, as shown in Fig. 4.3, the specimen was removed and inspected for any anomalies.

The laser-mechanical forming (LMF) process utilizes first the laser bending method and secondly the mechanical bending method. The laser forming process used is the same as described earlier, except that the number of scans per location was reduced to three. After the laser forming procedure was executed the average radius of curvature of the specimens was approximately 240 mm. Thereafter the mechanical forming procedure was employed to produce a final radius of curvature of approximately 120 mm.

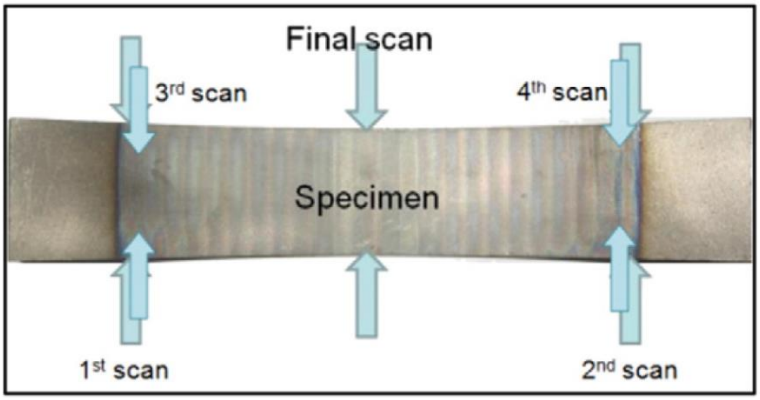

Fig. 4.1: Laser line scan sequence

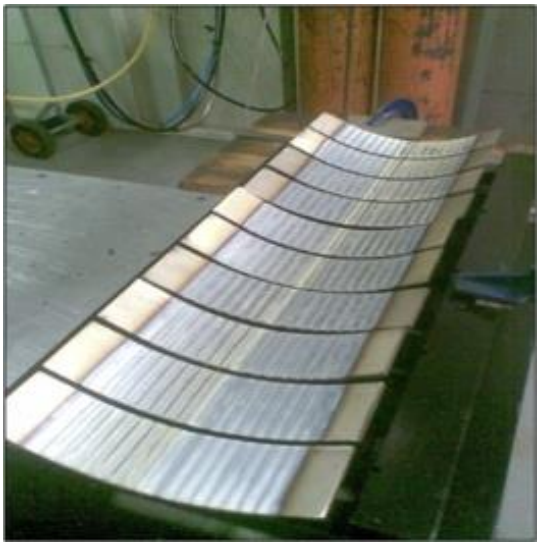

Fig. 4.2: CP Ti Grade 2 specimens irradiated in an open mould fixture.

Fig. 4.3: Sample after mechanical formed process.

4.2.2 Evaluation procedures

Vickers microhardness testing was done using a 300 g load and a 15 s dwell time and conducted according to [2]. Measurements were taken along the length of the laser formed samples as well as through the cross section of the thickness of the samples.

Samples were prepared for metallographic examination by following standard preparation techniques. After electrolytic polishing, the samples were etched in Kroll's reagent in order to reveal the microstructure. Samples were removed from the center position of the deformed sample in such a manner as to ensure that the region to be analyzed corresponds to the center of the position of the fatigue sample to be machined from the laser formed specimen.

The radius of curvature was measured by a Mitutoyo profile projector (PV-350) and manually verified through reverse engineering (drafting instrumentation). An arc length of 80 mm was chosen to ascertain the curvature as it spans the length of an hour-glass fatigue specimen to which these formed samples will be ultimately subjected. This arc length was taken as 40 mm to either side of the samples' midlength, i.e. considering the middle section of the formed sample.

Charpy impact samples were taken from each bending application as well as from the parent plate. Fig. 4.4 shows the positions where the samples were removed. Substandard Charpy impact specimens were machined and

tested according to ASTM E23-02 [1]. Four samples were removed from a single specimen (as shown in Fig. 4.4) and tested at two temperature settings i.e. −40°C and room temperature (21°C).

Residual stress measurements were performed using the hole drilling method. The following predetermined parameters were used in [9]:

- Drilling depth: 2 mm
- Evaluation method: Polynomial
- Number of incremental drilling steps: 20
- Drilling federate: 0.2 mm/min
- Delay time: 10 s

A strain gauge was applied in the center of the inner curve as it was previously determined that the maximum relieved residual stress magnitude corresponds to the inner surface. An EA-06-062RE-120 type strain gauge was used for this study and mounted according to the manufacturer's standard. After drilling, the eccentricity of the hole was measured and the principal stresses were calculated using ASTM E837-01 [4]. The Uniformed Stress Method [16] was used to compare the results obtained from the various samples.

Fatigue specimens from all three bending methods and the parent plate were machined according to ASTM E466-96 [3] dimensions, as shown in Fig. 4.5. The width of the specimen in the center was measured to be 19 mm. The parent plate and mechanically bent samples were water jet cut (to ensure minimal microstructure damage/change) and machined down to specification. Laser-mechanical and laser formed specimens were laser cut followed by a final machining step to ensure smooth surfaces in the radius of the samples.

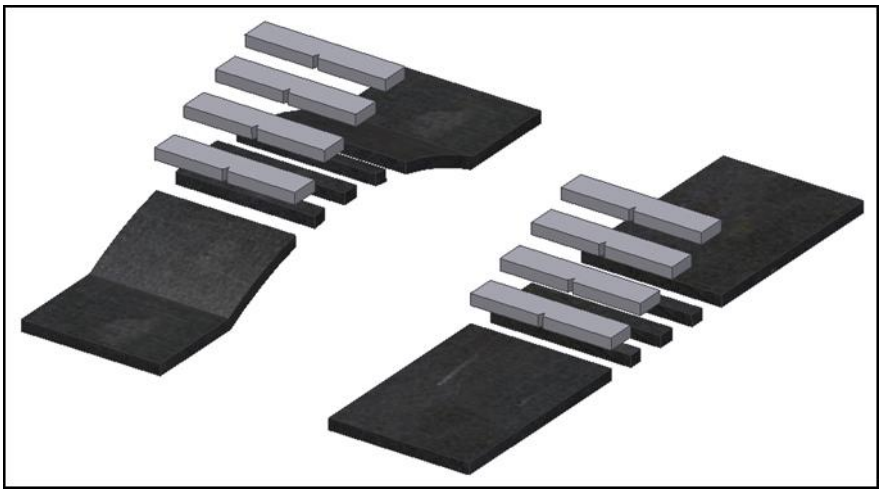

Fig. 4.4: Positions of Charpy V-notch samples.

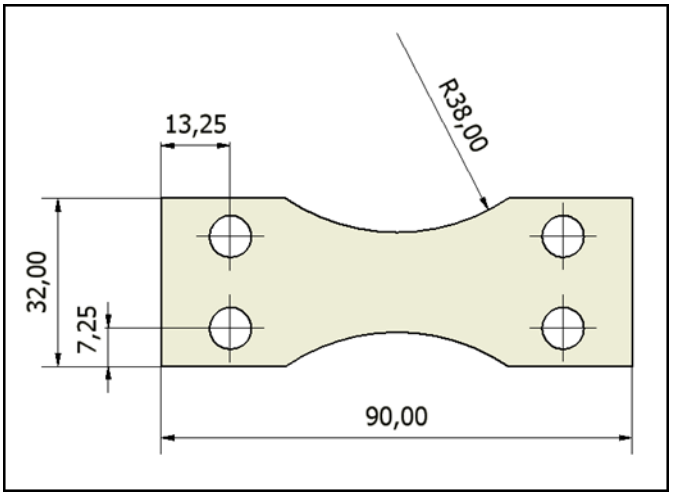

Fig. 4.5: Fatigue sample dimensions — wasted hour glass.

4.3 Results and discussion

4.3.1 Bending response analysis

In producing samples to ~120 mm radius of curvature (inside radius) a number of trials with varying laser scanning velocities were conducted. The overall bend angle achieved per scanned location was calculated at 3°, taking the arc length and interval spacing into account. The line energy was altered by changing the scanning velocity (varying between 1 m/min and 5 m/min) and keeping the other process parameters constant. The effect of line energy changes on both the radius of curvature and scanning velocity is shown in Fig. 4.6. The best fitted curve of the data plotted on Fig. 4.6 follows a polynomial function to the fourth degree and shows that it will be possible to produce samples with the same approximate radius of curvature using two different settings i.e. one setting with low line energy and one having high line energy.

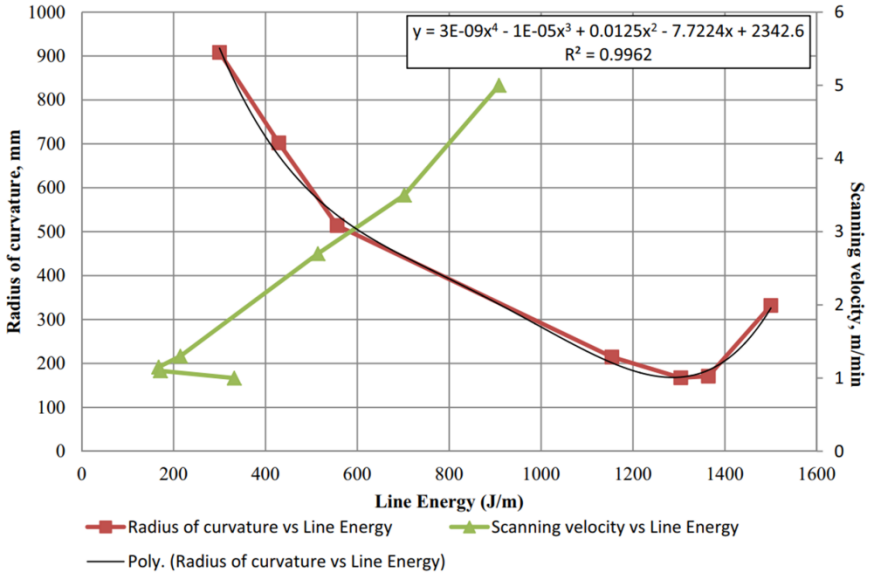

Fig. 4.6: Effect of line energy on the average radius of curvature.

4.3.2 Microstructure

The original microstructure of the CP Ti grade 2 consists of equiaxed alpha grains with an average grain diameter of 89.8 μm. The material was supplied in the hot rolled and pickled condition. The microstructures observed are shown in Fig. 4.7.

After laser forming (LF), the laser irradiated surface exhibited a microstructure consisting of very fine hexagonal martensitic phase (α') i.e. acicular martensite. This type of microstructure is typical for quenched CP titanium as observed by Ganesh and Ramanaih in their study on the effect of quenching and ageing on the tensile strength of CP titanium [11]. Mechanically formed (MF) specimens showed evidence of deformation twin (lenticular) in the grains near the surface which was in contact with the forming die. The microstructure observed is consistent with the microstructure formed during hot rolling of CP titanium as reported by other researchers [12]. The microstructure of the laser/mechanically formed samples showed a combination of the microstructures observed for the single processes i.e. a fine martensitic structure with some deformation twins clearly visible in the equiaxed grains. The depth of microstructure change associated with the laser forming process was measured to be 313 μm (measured from the laser irradiated surface). Twinning due to the mechanical forming process was observed to an approximate depth of 870 μm (also measured from the laser irradiated surface).

4.3.3 Mechanical properties

The maximum relieved residual stress values obtained, given in Table 4.1, are subject to errors below 10%, as specified by the Vishay Precision Group [16]. For the parent plate and all three forming processes three samples were used to determine the maximum residual stress. It is evident that the laser forming process induced the highest level of tensile residual stresses into the material compared to the other forming processes (measured on the inner radius surface).

The results of fatigue testing (zero mean stress conditions) at high and low loading conditions are given in Table 4.2. For the parent plate and Laser and Mechanical processes six samples were used for each load setting, whilst for the Laser/Mechanical process five samples were used per load setting. At both load settings the parent material performed the best with all the forming processes resulting in a decrease in fatigue life irrespective of load magnitude. Considering only the forming processes, the laser formed specimens performed superior at the highest load setting although it performed the weakest at the lowest load setting when considering fatigue testing. The improvement in fatigue resultant high load settings could be due to the fact that no twinning was observed after forming; therefore crack initiation was slower to develop. It has been documented that crystallographic anisotropy

has a strong influence on fatigue crack initiation [6]. It seems that microstructure is the most important factor to consider at high fatigue load settings whereas when considering the lower load setting, the residual stress magnitude seems to have a larger influence on fatigue crack initiation and propagation. The phenomenon of microstructure sensitivity was also encountered where an equiaxed microstructure achieved more cycles before failure than that of lamellar microstructures (Titanium: A Technical Guide, [7]).

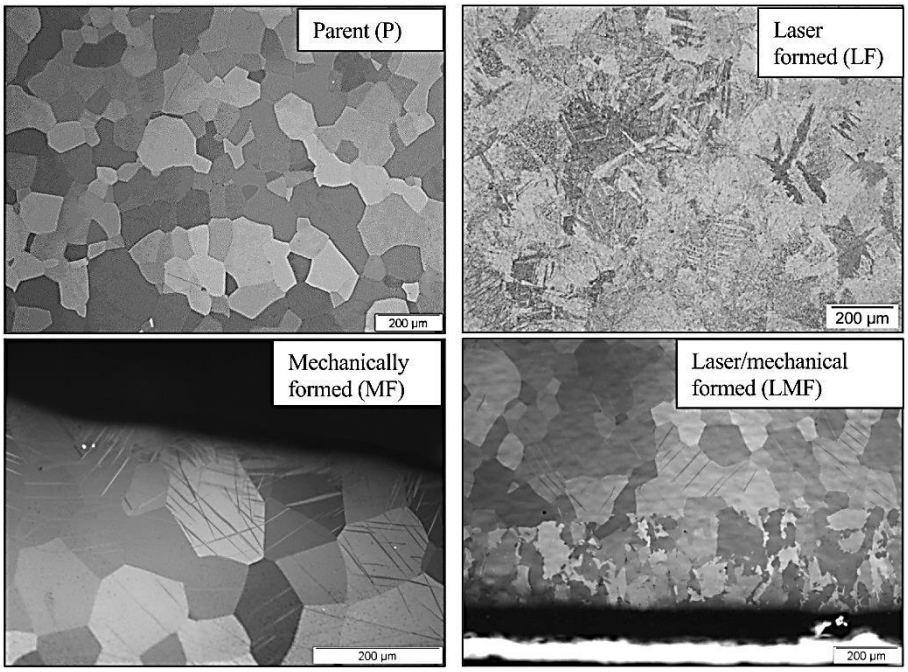

Fig. 4.7: Microstructure appearance of various samples.

Table 4.1: Relieved residual stress results.

Forming Process	Maximum stress (MPa)
Parent (P)	60.51 (± 6)
Laser formed (LF)	109.34 (± 11)
Mechanical formed (MF)	87.44 (± 9)
Laser/Mechanical formed (LMF)	87.76 (± 9)

Table 4.2: Fatigue results (N_f = average number of cycles to failure).

Forming process	Fatigue curve equations.	Fatigue life (high load 350 MPa) (N_f)	Fatigue life (low load 231 MPa) (N_f)
Parent (P)	$y = -185.6\ln(x) + 2328.9$	45 420	88 115
Laser (LF)	$y = -113.9ln(x) + 1439.2$	14 242	40 801
Mechanical (MF)	$y = -70.72ln(x) + 1008.6$	11 281	64 504
Laser/Mechanical (LMF)	$y = -86.26ln(x) + 1168.2$	13 382	55 998

Table 4.3: Results of impact (Charpy V-notch) testing.

Sample process	Room temperature Impact, J/mm^2	− 4°C (±5%) Impact, J/mm^2
Parent (P)	1.063	0.781
Laser (LF)	0.541	0.453
Mechanical (MF)	0.969	0.738
Laser/Mechanical (LMF)	0.623	0.445

Table 4.4: Vickers microhardness results, (HV0.3).

Sample process	HV0.3
Parent (P)	176
Laser (LF)	173
Mechanical (MF)	177
Laser/Mechanical (LMF)	169

Vickers microhardness testing showed that there was no significant difference in microhardness between the samples produced by the various forming

methods. The average results of Vickers microhardness testing are given in Table 4.4.

For the parent plate and all three forming processes three samples were used to determine the Vickers microhardness. The LMF samples were further evaluated to determine whether there is a significant difference between the twinned region and laser irradiated region (i.e. fine martensite). The results revealed that the twinned region has an average hardness of 171.1 HV0.3 compared to the laser irradiated microstructure which exhibited an average hardness of 172.2 HV0.3. The maximum average difference between the forming processes is 8 HV and can be considered as negligible as the Vickers micro-hardness test equipment has a deviation of 30 HV units. When all the properties are normalized against the values obtained for the parent material i.e. parent material equal to a value of one, it is evident that all the properties measured deteriorated due to the forming processes. The comparative results in relation (ratio) to the parent material are shown graphically in Fig. 4.8.

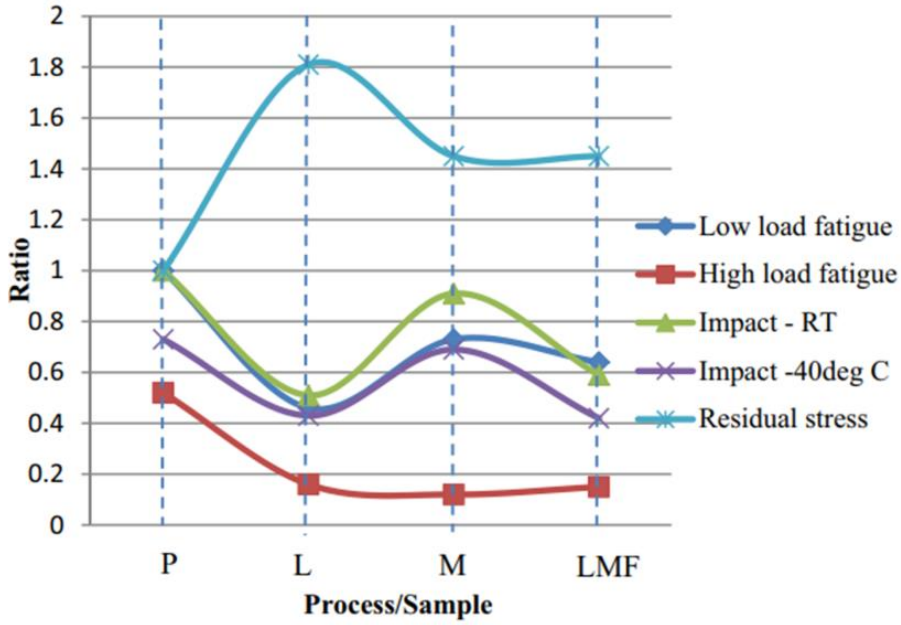

Fig. 4.8: Comparative results in relation to parent material properties.

4.3.4 Residual stress verses depth

The residual stress results of CP Ti were determined using the hole-drilling technique according to the average stress method (ASM) as described by ASTM E837-08e1 [4] and Schajer [24 - 25] which is summarized in Table 4.5. Tensile residual stresses (inner surface) of 115 MPa in LF and 94 MPa in MF plates were determined after a first step of deformation (240 mm radius of curvature).

Further bending to 120 mm curvature caused no significant changes in the stress magnitude; residual stresses of 109 MPa and 87 MPa were determined in LF and MF plate samples, respectively. The results for plate samples deformed by the combined laser and mechanical application showed the presence of tensile residual stresses of 88 MPa (Fig. 4.9). Similar trends were observed for the outer surfaces (see Table 4.5). Considering the bulk stress relief of the LF plate samples, the maximum stress of 115 MPa was relieved at a depth of approximately 1 mm.

In summary, the results obtained by this analysis show that bending by all three deformation methods resulted in the formation of tensile residual stresses; measured residual stress magnitudes varied between 5 and 30 % of the parent material's yield strength value. The values obtained by the mechanical and combined bending applications did not show any significant variance in magnitude (namely: 87 versus. 88 MPa), while the LF process resulted in slightly higher residual stress values.

It should be noted that deformation of Ti plate samples to the final curvature (~120 mm) did not reveal higher stress magnitudes in comparison to the first deformation step (~240 mm). In fact, stress relaxation occurred in both the LF and the MF plate samples (see Table 4.5). Similarly, a stress relaxation from 115 MPa to 88 MPa was observed in the LMF plates after the first and second step deformation.

Table 4.5: Maximum relieved residual stresses of LB, MB and LB/MB plate samples at various depths

Manufacturing Process	AVERAGE STRESS METHOD (ASM)	
	σ_{max} (MPa)	Relieved depth (mm)
As-Received	45	1.8
LB 240 mm (inner curve)	115	1.7
LB 240 mm (outer curve)	59	1.4
MB 240 mm (inner curve)	94	1.6
MB 240 mm (outer curve)	32	2
LB 120 mm (inner curve)	109	1.3
LB 120 mm (outer curve)	62	1.6
MB 120 mm (inner curve)	87	1.9
MB 120 mm (outer curve)	19	2
LB/MB 240/120mm (inner curve)	88	1.2
LB/MB 240/120mm (outer curve)	24	1.9

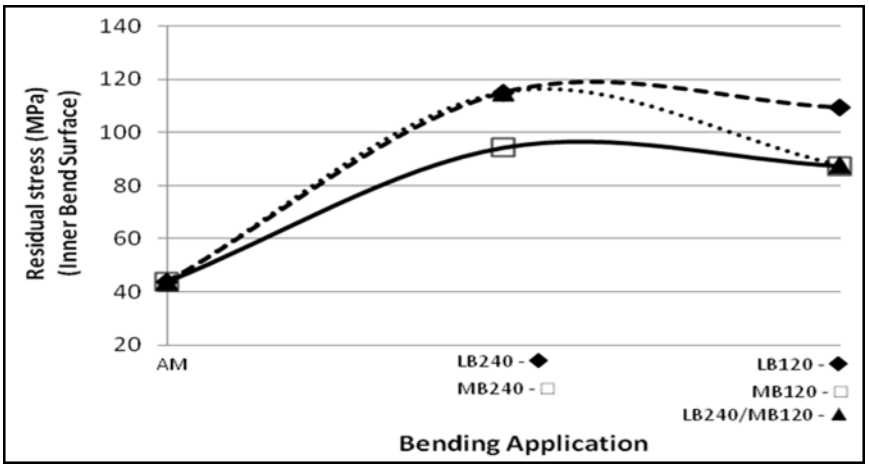

Fig. 4.9: Residual stress results of inner bent (i.e. 118.4 mm) surface obtained by Average Stress Method plotted for maximum relieved stresses from each bending process.

4.3.5 Fatigue Fracture and Secondary Fatigue Cracks

Fatigue fracture surfaces of all the samples were characterized by multiple crack initiation sites with a relatively rough surface appearance. The typical appearance of a fatigue fracture surface (representative of all samples tested) is shown in Fig. 4.10.

One fatigue sample (tested at high load conditions) from each forming process was evaluated by viewing the microstructure from the top surface i.e. normal to the original fracture path. This was done in order to determine whether the different type of microstructures observed influenced the crack path and amount of secondary fatigue cracks generated. The approximate position of microstructure evaluation in relation to the original fracture surface is shown schematically in Fig. 4.11.

The top surface view (using a stereo microscope) showing the amount of secondary cracks (bright lines) and their orientation in relation to the original fatigue fracture surface is shown in Fig. 4.12. The white arrows show the location of secondary cracks and the red arrows show the original fracture surface. It is evident that the laser formed sample showed a higher amount of secondary cracks that are aligned parallel to the original fatigue fracture surface. The LMF sample showed the least amount of secondary cracks.

Further evaluation of the secondary cracks on the top surface of the fatigue samples showed that the secondary cracks did not follow the twin

boundaries. It however seems that the twin boundaries influenced the direction of the crack path resulting in the jagged edges observed on the fracture surface. Scanning Electron Microscopy images of the top surface appearance are shown in Fig. 4.13.

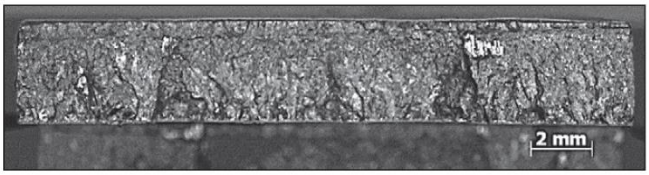

Fig. 4.10: Typical fatigue fracture surface appearance.

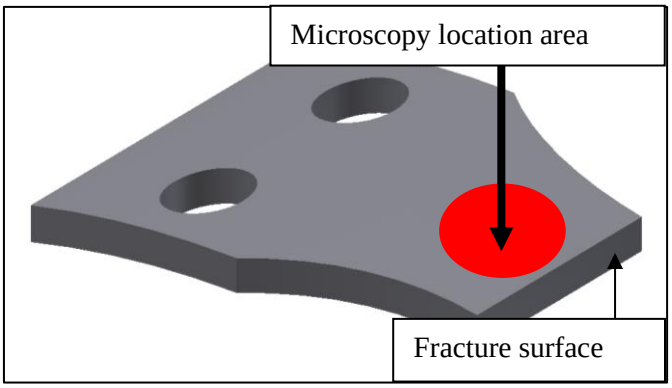

Fig. 4.11: Position of evaluation for secondary cracks.

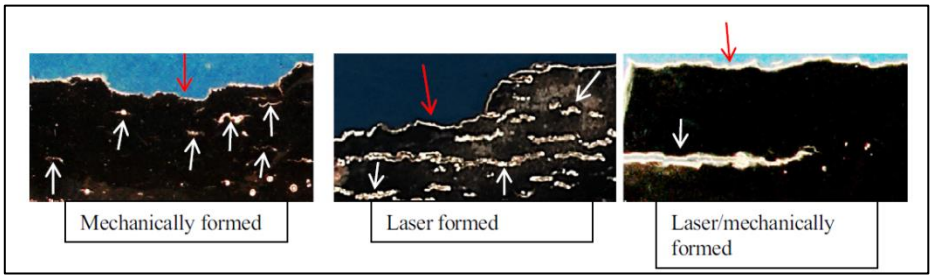

Fig. 4.12: Appearance of original fatigue fracture surface together with secondary cracks.

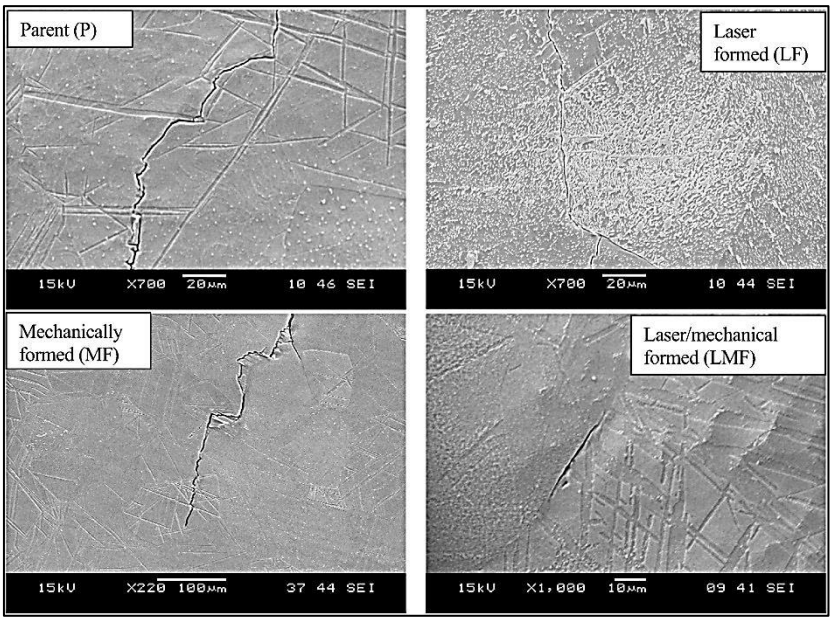

Fig. 4.13: Appearance of secondary cracks normal to the main fatigue fracture surface.

4.4 Conclusions

From the results obtained it is evident that the following conclusions can be drawn:

1. It is possible to produce the same radius of curvature by using two different sets of laser parameters for CP titanium within the approximate range of 150 mm to 350 mm.
2. All samples tested showed a similar trend in that the mechanical properties were decreased compared to the original parent material.
3. The resulting behavior of all samples was bending concave upwards towards the laser source.
4. Even though there is no significant change in hardness of the samples produced by the various forming processes, there was a noticeable difference in the appearance of the microstructure.
5. The mechanical forming process resulted in a lower value of surface residual stress than the laser formed samples.
6. There is no significant difference in fatigue results between samples produced by the various processes tested at a high fatigue load (350 MPa).

7. From the results obtained it would seem that at high fatigue load conditions, the microstructure is the dominant important factor whereas at low fatigue loads, the residual stress magnitude is the dominant factor.

4.5 References

[1] ASTM Standard E23, Standard Test Methods for Notched Bar Impact Testing of Metallic Materials, 23–02, ASTM International, West Conshohocken, PA, 2002, http://dx.doi.org/10.1520/E0023-02, (2002, www.astm.org . (n.d.)).

[2] ASTM Standard E384-99, Standard Test Method for Micro indentation Hardness of Materials, ASTM International, West Conshohocken, PA, 2002., http://dx.doi.org/10.1520/E0384-99 (www.astm.org . (n.d.)).

[3] ASTM Standard E466, Standard Practice for Conducting Force Controlled Constant Amplitude Axial Fatigue Tests of Metallic Materials, 466(96), ASTM International, West Conshohocken, PA, 2002, http://dx.doi.org/10.1520/E0466-07, (www.astm.org . (n.d.)).

[4] ASTM Standard E837, Standard Test Method for Determining Residual Stresses by the Hole-drilling Strain-gage Method, 837(01), ASTM International, West Conshohocken, PA, 2002, http://dx.doi.org/10.1520/E0837, (2002, www.astm.org . (n.d.)).

[5] K. Bartkowiak, S. Edwardson, G. Dearden and K. Watkins, 2-D Laser Forming Comparative Study on Nd:YAG of Titanium Alloy Ti-6Al-4V. ICALEO 2004, Laser Institute of America, San Franscisco, 2004.

[6] K.S. Chan, Roles of microstructure in fatigue crack initiation, Int. J. Fatigue 32 (9) (2010) 1428–1446.

[7] M.J. Donachie, Titanium: A Technical Guide, 2nd ed. ASM International, Materials Park, Ohio, 2000.

[8] M.J. Donachie, Titanium: A Technical Guide, 2nd ed. ASM International, Materials Park, Ohio, 2007.

[9] A. Els, Material Characterisation of Laser Formed Dual Phase Steel Components, (DTech thesis) Nelson Mandela Metropolitan University, Port Elizabeth, 2005.

[10] A. Els and P. McGrath, H. Pienaar, Bending behaviour of high-strength low-alloy steel, R&D J. SAIMechE 23 (1) (2007) 35–38.

[11] B.K. Ganesh and N. Ramanaih, Effect of rapid quenching and aging on tensile behavior of commercially pure (CP) titanium implant material, J. Eng. Technol. Res. 3 (9) (2011) 279–283.

[12] M. Hayashi, M. Ishii, H. Yoshimura and H. Harada, Recrystallization behaviour of commercially pure titanium during hot rolling, Nippon Steel Technical Report, 1994, (62).

[13] C.J. Hughes, Fatigue Behaviour of Laser Formed High Strength Low Alloy Sheet Material, (MTech thesis) Tshwane University of Technology, Johannesburg, 2004.

[14] J. Magee, K. Watkins and W. Steen, Advances in laser forming, J. Laser Appl. 10 (1998) 235–246.

[15] M. Marya and G. Edwards, A study on the laser forming of near-alpha and metastable beta titanium alloy sheets, J. Mater. Process. Technol. 108 (3) (2001) 376–383.

[16] Micro-measurements, Measurement of Residual Stresses by the Hole-drilling Strain Gage Method, Tech note (TN-503-3) Vishay Precision Group, 1988.
[17] Y. Namba, Laser forming of metals and alloys, Laser Advanced Materials Processing: Proceedings of the LAMP'87 conference, High Temperature Society of Japan, Osaka, Osaka, Japan, 1987, pp. 601–606.
[18] K. Scully, Laser line heating, J. Ship Prod. 3 (4) (1987) 237–246.
[19] D. Shidid, H. Hoseinpour Gollo, M. Brandt and M. Mahdavian, Study of effect of process parameters on titanium sheet metal bending using Nd:YAG laser, Opt. Laser Technol. 47 (2013) 242–247.
[20] S. Silve, B. Podschies, W.M. Steen and K.G. Watkins, Laser forming a new vocabulary for objects. In laser materials processing, in: P. Christensen, P. Denney, I. Miyamoto, K. Watkins (Eds.), Proceedings of the ICALEO'99 conference, Laser Institute of America, Orlando, San Diego, California, 1999, pp. F87–F96.
[21] F. Vollersten, Mechanisms and models for laser forming, in: M. Geiger, F. Vollersten (Eds.), Laser Assisted Net Shape Engineering: Proceedings of the LANE'94 conference, Meisenbach, Bamberg, 1994, pp. 345–360.
[22] F. Vollersten, I. Komel and R. Kals, The laser bending of steel foils for microparts by the buckling mechanism — a model, Model. Simul. Mater. Sci. Eng. 3 (1) (1995) 107–119.
[23] D. Walczyk and S. Vittal, Bending of titanium sheet using laser forming, J. Manuf. Process. 2 (4) (2000) 258–269.
[24] G.S. Schajer, Measurement of non-uniform residual stresses using the hole drilling method. Part I: Stress calculation procedures. J. Eng. Mater. Technol., 110, 338-343, 1988.
[25] G.S. Schajer, Measurement of non-uniform residual stresses using the hole drilling method. Part II: Practical application of the integral method. J. Eng. Mater. Technol., 110, 344-349, 1988.

Chapter 5

Response of Ti microstructure in mechanical and laser forming processes

5.1 Introduction

As a follow up of Chapter 4 microstructural deformation mechanisms present during three different forming processes in commercially pure Ti were analyzed in greater detail by microscopy methodology. Room temperature mechanical forming, laser beam forming and a combination of these two processes were applied to thick metal plates in order to achieve the same final shape. An electron backscatter diffraction technique was used to study the plate microstructure before and after applying the forming processes. Substantial differences among the main deformation mechanisms were clearly detected.

In pure mechanical forming at room temperature, mechanical twinning predominates in both compression and tensile areas. A dislocation slip mechanism inside the compression and tensile area is characteristic of the pure laser forming process. Forming processes which subsequently combine the laser and mechanical approaches result in a combination of twinning and dislocation mechanisms. The Schmid factor at an individual grain level, the local temperature and the strain rate are factors that determine which deformation mechanism will prevail at the microscopic level. The final microstructures obtained after the different forming processes were applied are discussed from the point of view of their influence on the performance of the resulting formed product. The observations suggest that possibly phase transformation in Ti is an additional microstructural factor that has to be considered during laser forming.

5.2 Titanium microstructure response after forming

The high specific strength and excellent corrosion resistance are what makes titanium-based alloys attractive material for use in the aerospace industry. In addition, Ti exhibits a high melting temperature and can be used at high

temperatures (around 800 K) with excellent toughness and creep properties. Despite the numerous advantages such as the highest specific strength (yield strength-to-weight ratio) of any metal, it exhibits poor tribological and less advanced fatigue properties. In the domain of manufacturing, mechanical forming (MF) is a frequently used industrial process on titanium. Rapid forming of metal components by laser forming (LF) is, however, becoming more popular due to the flexibility of laser systems. Laser forming of a sheet metal in two-dimensional shapes was first reported by Namba [1] in 1985. Laser forming has furthermore been applied to industrial processes in the naval construction industry using flat steel plates which have to be formed into three-dimensional shapes [2–5]. Numerical finite element and finite difference methods have been applied [6,7] to model laser forming, and a semi-empirical model has been suggested to predict the appropriate bend angles. A number of the developments, techniques and modelling procedures for laser forming have been reviewed in [8].

LF is achieved by thermal stresses being introduced into the substrate by means of an irradiated laser beam, which results in rapid localized heating without melting. As already explained in Chapter 3 and shown in Chapter 4, the onset of these thermal stresses exceeds the elastic strain of the material, which results in a controlled thermo-elastic plastic distortion. As a result, the plate can bend away from the laser due to the high thermal expansion. The local temperature and geometry of the induced thermal stress play a crucial role in the final desired shape of the substrate. The laser is then turned off or moved onto the adjacent area, depending on the laser sequence path, which also plays a key role in the desired final shape that will result in cooling or shrinkage. The shrinkage will lead to the onset of bending or shape change of the substrate. In [9], three mechanisms are presented that explain laser forming associated with geometries and processing. It comprises the temperature gradient mechanism (TGM), the buckling mechanism (BM) and the shortening or upsetting mechanism (UM).

Semi-empirical models have been derived for the TGM by Shen and Vollertsen [8] and Yau et al. [10] to calculate the bending angle. FEM simulations have been explored in [11] to predict the bending angle as predicted by the analytical model [8]. In this study, the temperature gradient mechanism will dominate since the material is considered a thick plate (greater than 1 mm). This means that the temperature of the top side is very high due to the irradiation of the laser compared to the bottom side where the temperature is low or even unaffected. Furthermore, the heat diffuses into the material relatively quickly from the top side, which depends on the thermal conductivity of the material. However, the thermal gradient is usually not a

constant along the thickness of the substrate due to movement of the laser. (see Chapter 3). Moreover, laser forming has a large number of processing parameters such as scanning speed, laser beam diameter, power density and wavelength. At the same time, the physical properties of the material such as absorption coefficient, thermal conductivity and thermal expansion play a vital role in the selection of the above-mentioned processing parameters.

Precise understanding of the thermal stresses created during the LF process is extremely vital in order to acquire a fundamental understanding of the material performance. Despite the availability of diverse techniques to observe the material behavior/bending capability such as digital image correlation and forward-looking infrared cameras, a relatively large uncertainty in the predictive power of these models is still present today [8]. In spite of the development of laser forming since the 1980s, scant work has been done to include microstructural behavior and applying it to modelling.

Electron backscatter diffraction (EBSD) is a technique used to characterize crystallographic properties such as grain size, grain orientation, misorientation and local deformation. This method will be explored in this study to accurately determine the microstructural changes from the substrate to that of the LF and MF processes in commercially pure titanium (CP Ti). Plastic deformation in metals during the forming process is primarily carried out by the nucleation and motion of dislocations. CP Ti has a limited number of slip planes when it is in the a-HCP phase (anisotropic) and gives rise to twinning as one of the deformation mechanisms. However, CP Ti undergoes an allotropic phase transformation at ~ 885 °C (α-HCP to β-BCC). During the LF process, the material is heated above the phase transformation temperature and then cooled down to room temperature in open air. The beta-to-alpha phase cooling rate therefore has an influence on the resulting microstructure which can also lead to a large amount of stored dislocations and can give rise to a residual stress state of the material. A phenomenon that is often overlooked during the LF processes is when the material undergoes a phase transformation during the constituent phases as this can lead to an increase or decrease in volume within the heated geometry. This may influence the performance of the bending angle considerably during the LF process and can give additional input to the analytical models as described in [5,8].

Research teams such as The Boeing Company and Massachusetts Institute of Technology (MIT) produced analytical methods that resulted in lower computed values for the LF bending angle compared to the experimental results [12]. For this reason, CP Ti was selected because of its phase transformation at high temperature during the LF process. EBSD was

chosen to characterize the detailed local strain behavior in this material due to the variations in the slow and fast deformation forming mechanism.

This study therefore aims at investigating the differences in microstructural behavior and variations in microstructural performance between mechanical forming (MF) and laser forming (LF). The microstructural properties of laser–mechanical forming (LMF) outlined in this study furthermore give additional insight when MF was performed after LF on a single specimen. These findings can extend the methodology of LF and can give additional input parameters to the empirical and analytical modelling of LF.

5.2.1 Mechanical and laser forming setup method

Mechanical forming was performed on CP Ti rectangular test samples (200 × 50 mm) with a thickness of approximately 3.2 mm (see also Chapter 4). A Rejva/Gosmeta mechanical press was used with a maximum force capacity of approximately 25 tons. The tool and die fitted was designed so that the mean curvature of the sample would be 120 mm in radius. The strain was calculated at the outer edges of the specimens to be approximately 18.2 % and a strain rate of approximately 0.54/s for the MF process. All MF processes were performed at room temperature. For the LMF process, LF was first utilized, after which the MF process was used. The LF process was carried out by using a 5-kW continuous CO_2 laser with a wavelength of 10.6 μm. The parameters that influence the curvature of the specimen during the laser process are (1) the laser beam diameter, (2) the number of scans per location, (3) the laser power, (4) the interval spacing between consecutive laser lines and (5) the scanning speed. Based on the previous work (see [13]), the selected LF parameters are listed in Table 5.1, which can generate a geometry of 240 and 120 mm radii as shown in Fig. 5.1. Fig. 5.1 also shows the sequence followed by the laser beam from the first scan until the last scan. The black dot indicates the starting position of the laser beam, and the grey/ brown dot indicates the furthest position before the beam returns or moves to the next track. Calculations of the strain per scan for the LF process were done by dividing the total strain amount by the number of scans, also incorporating any beam overlap per scan adjacent to it. The processing time can be calculated by dividing the laser beam diameter by the laser scanning speed. The total strain rate can be determined by dividing the strain per scan by the processing time. The strain rate for the 120 mm radii was 0.025/s and 0.038/s for the 240 mm radii.

The LF process used the same parameters and scanning sequence as described earlier in the LMF process. The number of scans per location was, however, increased to six, and the scanning speed was lowered to achieve the geometry of 120 mm radii. Ten test samples were positioned in an open mold adjacent to one another and were scanned during the LF process. Repeatability of the LF process was very high considering that only approximately five samples had small curvature deviations out of the approximate 100 samples produced with LF. The LMF and LF processes started at room temperature. For a better understanding of the behavior of the material during each forming process, EBSD was performed on the non-deformed substrate and on cross-sections of samples for all three forming processes. Fig. 5.2 shows the position where the samples for EBSD observation were removed from the substrate and the apex for each forming process while keeping the rolling and transverse directions the same. Fig. 5.2 also shows the areas of interest viz. top (inside the curvature radius, approximately 118.4 mm radii) (~ – 18.2 % strain), middle (at the neutral axis) and bottom (outside the curvature radius, approximately 121.6 mm radii) (~ + 18.2 % strain).

Thermal imaging was recorded throughout the LF process by means of a forward-looking infrared (FLIR) camera. Additionally, a pyrometer was also used to measure the bottom area of the specimen during the LF process. The transverse intensity profile of the laser beam TEM01 (defocused) was kept at a constant height during all scanning procedures. *No melting* of the material takes place during this forming process.

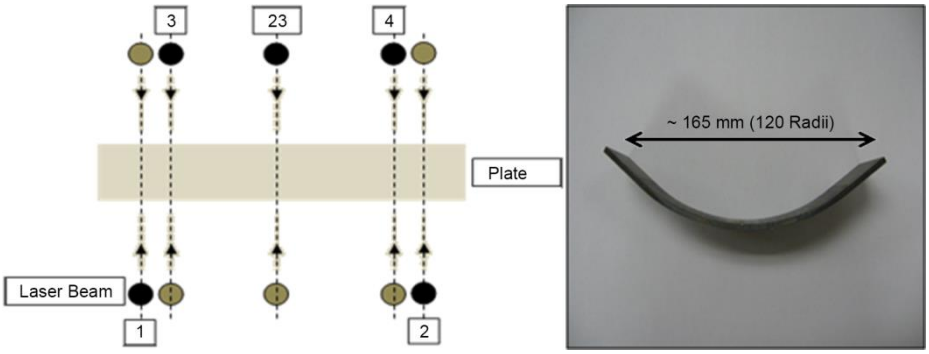

Fig. 5.1: The sequence of laser path (left) and side view of Ti specimen after applying the laser forming process (right).

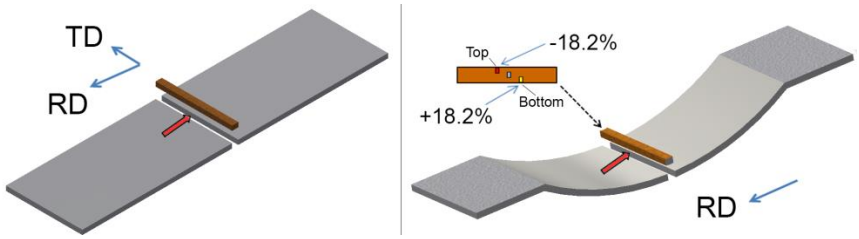

Fig. 5.2: Position of microstructural observations substrate (left), after bending process (right).

Table 5.1: The sequence of laser path (left) and side view of Ti specimen after applying the laser forming process (right).

Radius of curvature (mm)	Power (kW)	Scanning speed (mm/s)	Beam overlap (%)	No. of scans per location	No. of locations	Laser beam diameter (mm)
240	1.5	30	50	3	23	12
120	1.5	20	50	6	23	12

Temperatures within the laser spot and throughout the forming process were approximately 1050–1500°C. (Melting point of CP Ti Gr2 is ~ 1650°C). After radiation, the samples were air-cooled until room temperature. Fig. 5.3 shows the temperature at a point on the 1st scan of track 23 (see Fig. 5.1). It illustrates heating and cooling rates of the sample during the LF process. The 1st scan undergoes a sharp heating rate (within 100 ms) of approximately 10000–11000°C/s before the onset of the laser beam path when measuring from frame to frame. A cooling rate of approximately 4000–5300°C/s is observed after the offset of the laser beam path. The heating and cooling cycles at any given point through the laser path take place over a time frame of ~ 400 ms. The two peaks within the graph are due to the TEM_{01} beam profile. Fig. 5.3 also shows the same point but for the 6th scan of track 23, which is the final LF scan of this track. The heating rate was calculated to be approximately 2000–2700°C/s before the onset of the beam path and a cooling rate of approximately 1300°C/s at the offset of the laser beam path.

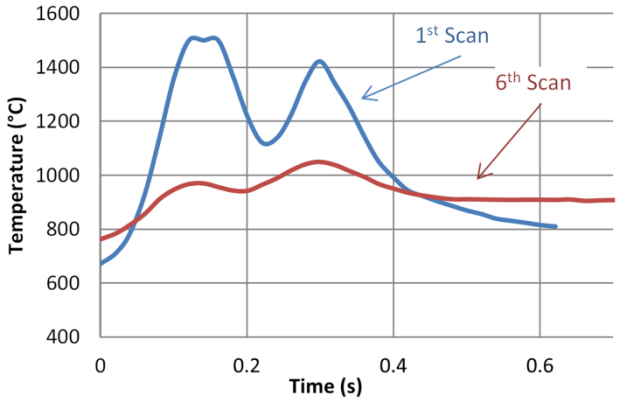

Fig. 5.3: Top surface temperature at a point on track 23 during the 1st and 6th scan measured with FLIR camera during the LF process.

The 1st track has a much higher peak/gradient value, which can be attributed to the high temperature of the black paint that was applied to the samples to promote better in coupling of the light into the material. However, after the 1st scan was performed, most of the paint was burned off which revealed CP Ti material. A thin oxidation layer was present after the LF processes was completed. This can be attributed to the burned-off paint and the fact that no shielding was used during the process. The 6th scan shows an increase in the temperature of approximately 100°C during the onset of the laser compared to the 1st scan, which is due to the heat transfer in the material by previous scans (i.e. 5th scan). For making TGM effective, it is very important to keep the temperature within a specific range since a too hot specimen can melt.

CP Ti specimens were prepared for EBSD analysis by mechanical polishing and finished with a 0.04-µm sized polishing agent [14]. A field emission gun (SEM-TESCAN, Brno, Czech Republic) in combination with an EBSD system (Edax Inc., Draper, UT, USA) equipped with a fast Hikari super EBSD camera was used for the crystallographic and microstructural characterization. Crystallographic orientations were achieved by detecting the 10 strongest Kikuchi bands and indexing of the HCP alpha phase in conjunction with a step size of 1 µm (hexagonal grid) using an acceleration voltage of 25 kV. EBSD data were analyzed using the orientation imaging microscopy TSL OIM Analysis 7.3 software. Before orientation imaging microscopy (OIM) data analysis, the data cleaning procedure was applied to remove speckle points from the OIM maps. A confidence index (CI) standardization with a grain tolerance of 5° and a minimum grain size of 5 pixels were used for the first step, followed by neighbor orientation

correlation cleaning when the crystallographic orientation of points with low CI (< 0.1) has been modified to an orientation defined by the majority of neighboring points with CI higher than 0.1. Finally, all points with CI < 0.1 have been removed from OIM maps. These points are shown as white points in OIM maps. During the cleaning procedure, no more than 2% of the scanned point orientations have been modified.

5.2.2 Experimental results

Fig. 5.4 shows the [001] inverse pole figure (IPF) maps of the cross section of the plate (refer to Fig. 5.2) before and after the three forming processes. The substrate material was supplied in the hot-rolled condition and consists of equiaxed alpha grains with an average grain diameter ranging from approximately 70–100 μm, as seen in Fig. 5.4A. Deformation twins are present through the whole plate thickness. The microstructure of the plate after mechanical forming is shown in Fig. 5.4B which shows the top, middle and bottom sections, with a dimension of 360 x 750 μm for each individual area of interest. The grain size did not change in comparison with the non-deformed plate, but the density of the deformation twins increased in both, top and bottom subsurface areas. Figs. 5.4C, d illustrate the microstructure after laser forming and laser–mechanical forming of the plate from top to bottom, each with dimensions of 700 x 3200 μm. The original microstructure substantially changed through the whole thickness of the laser-formed sample and the inside top area of the laser–mechanical-formed plate. The laser forming and partial of the laser–mechanical forming show a very fine hexagonal martensitic phase (a′), i.e. acicular martensite which is a typical effect for quenched pure titanium [15]. Laser–mechanical forming, Fig. 5.4D, showed clear evidence of deformation twinning near the top and bottom, while the average grain diameter in the middle and bottom parts of the plate is similar to that of the initial substrate.

The literature indicates that multiple deformation twinning modes can be realized in CP Ti and split into two categories, viz. compression and tension deformation twins [16–18]. Compression and tension deformation twins are understood to be the primary mechanisms for c-axis compression/shorting and tension/elongation on bulk samples. Also, prismatic slip and tension twin types are easier to activate under tensile conditions compared to compression twin types under compression conditions along the c-axis of the grain [19].

Our EBSD observations revealed that five twinning systems were active within all the samples. The results are summarized in Table 5.2, in which the twinning plane and direction are shown together with the rotation axis and angle for each observed twinning system. Only two twinning systems were observed in the microstructure of plates before forming. However, after the forming processes three additional twinning systems were visible throughout the specimens. All the detected active twinning systems within the CP Ti samples are listed in Table 5.2 for the substrate and substrate after the application of the forming processes. Twins were detected in OIM analysis through the identification of boundaries with a characteristic theoretical rotation angle (as shown in Table 5.2) with a maximum angular deviation of ± 5°.

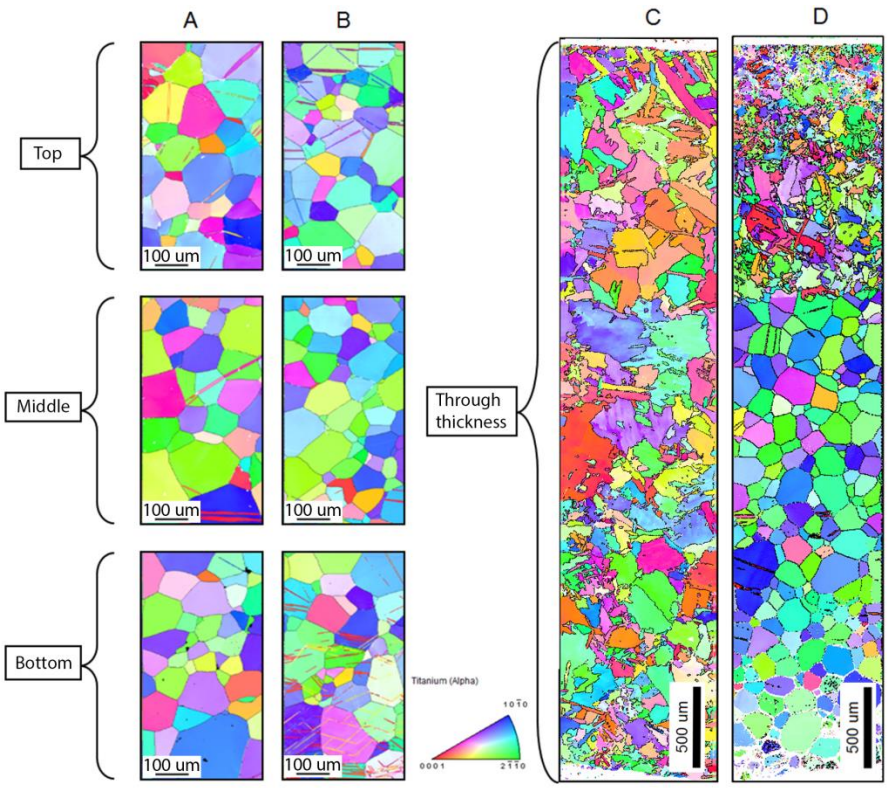

Fig. 5.4: OIM [001] inverse pole figure maps of a) substrate, b) after mechanical forming, c) substrate after laser forming, d) substrate after laser-mechanical forming.

Table 5.2: Active twinning systems present at different forming processes

Twinning system Rotation angle @ Axis	Twin type	Substrate	Mechanical forming	Laser forming	Laser – Mechanical forming
{11-21} <11-2-6> 34.80° @ <1-100>	Tensile	X	✓	✓	✓
{10-11} <10-1-2> 57.00° @ <11-20>	Compression	X	x	✓	✓
{11-22} <11-2-3> 64.30° @ <1-100>	Compression	✓	✓	X	✓
{11-24} <22-4-3> 76.70° @ <1-100>	Compression	X	✓	X	x
{10-12} <10-1-1> 84.70° @ <11-20>	Tensile	✓	✓	✓	✓

5.2.3 Substrate

Fig. 5.5 shows OIM Image quality (IQ) maps combined with highlighted twins and orientation deviation angle maps of the top and bottom sections of the substrate. Henceforth, only the top and bottom parts of the samples will be considered, where most deformation (strain) was performed during the forming processes. The attributes due to the manufacturing procedure and possibly due to the coiling and uncoiling processes can be observed in the IQ maps throughout the twinning in the substrate. The orientation deviation map describes the misorientation of each point relative to the average orientation of the corresponding grain. This quantity is quite useful to visualize the distribution of local misorientation build-up (local strain) as seen at the triple points and various twinning tips. Comparing the top and bottom IQ maps in Fig. 5.5, it is clear that more active twins are present at the top rather than at the bottom of the sample. Furthermore, the most dominant deformation twinning was the 84.70° tension system and small traces of the 64.30° compression twinning system were found at the top and bottom of the sample. The orientation deviation map confirms also a presence of local deformation due to dislocation motion, mostly in the vicinity of triple points and intersections between twin and grain boundaries.

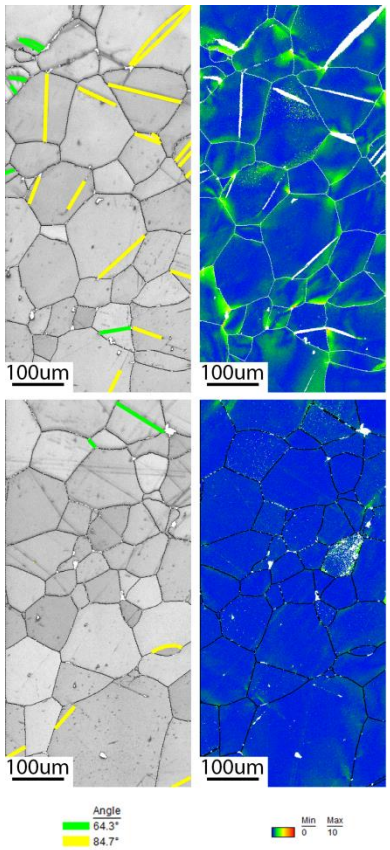

Fig. 5.5: Image quality maps with highlighted twins (left), and orientation deviation angle maps (right) of the same area at the top (top) and bottom (bottom) of the plate.

5.2.4 Mechanical forming

Fig. 5.6 shows IQ maps with highlighted twins and orientation deviation angle maps of the top section of the mechanically formed specimen. As the top part of the specimen experienced a majority of compression strain, the maximum deformation was recorded at the outer sections. Most deformation was observed from the top surface to a depth of approximately 400 µm. As a result of a low symmetry of the HCP structure, it often exhibits anisotropic deformation behaviour due to the lack of slip deformation modes along the c-axis. When comparing the microstructure formed during the MF process to the microstructure of the substrate, it is evident that twinning deformation was favored due to the fast forming speed and room temperature. Furthermore, the

orientation deviation angle map shows that some grains do exhibit plastic slip together with twinning in a single grain. The majority of the twinning deformation system is the 64.30° compression, while a minority of 76.70° compression together with 84.70° tension twins are also present. These microstructural features can be described as quilted looking structures due to the apparent crossing twinning systems after deformation [20]. The quilted structure forms through the blocking and propagation of the above-mentioned active twinning systems. These features have been widely observed within orthotropic materials [21–29]. Twin broadening was observed from the top surface to a depth of ~ 400 µm. The 64.30° twin system exhibited the most broadening/growth compared to the 84.70° and 76.70° twin systems under the compression load. Furthermore, due to the increase in strain from the neutral axis to the outer edge of the top surface, the OIM data show that twin broadening increases with strain. Twinning also appeared to be more frequent in higher grain sizes, which has been reported in several metals as the size effect [30]. The size effect is quantified by calculating a Hall–Petch coefficient for twinning based on a macroscopic yield stress.

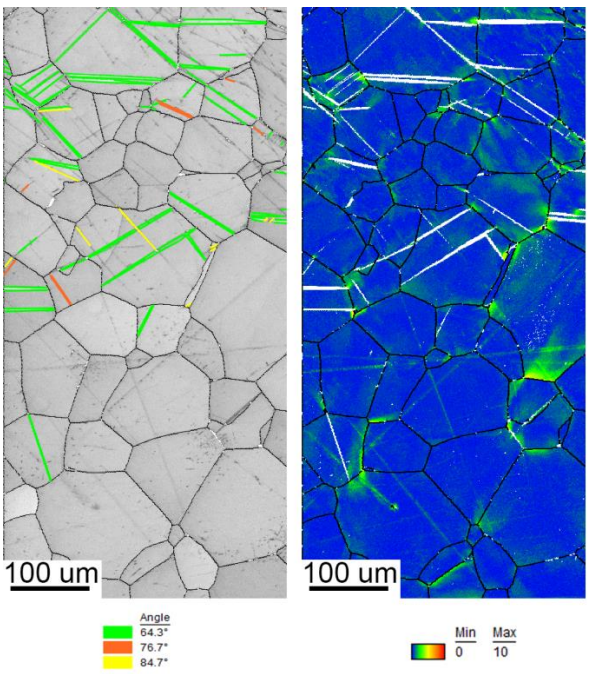

Fig. 5.6: Image quality map with highlighted twins of different types (left) and orientation deviation angle map (right) for top part of mechanically formed plate.

The distribution of the twinning was evaluated for approximately 20 grains that only contained twinning deformation within the MF top section. Fig. 5.7A–C shows the distribution for each scenario by color. It colorizes the grains that contain only 64.30° (a) twins together with grains containing both 84.70° + 64.30° (b) and 76.70° + 64.30° (c) twinning for each individual grain. The most dominant distributed twinning system was the 64.30° (grains contain only 64.30°) as seen in Fig. 5.7A where a significant colored area of twinned grains is evident, whereas the minority of grains contain a combination of two types of twinning. Additionally in Fig. 5.7, the Schmid factor was also evaluated for each individual twinned grain. Individual color of grains that contain twinning with a Schmid factor ranging from 0 to 0.5 is shown in Fig. 5.7A–C. It is clear that all twinned grains in Fig. 5.7 have a high Schmid factor.

The amount of the strain accumulated in the grain by twinning could be evaluated by measuring the twinned volume due to twin boundary motion that involves the glide of twinning dislocations in multilayer twin lamellae. Furthermore, lateral thickening of twinning occurs during loading stresses along the twin shear plane of the parent region which gives rise to deformation volume.

In Fig. 5.8, the Schmid factor is correlated with the daughter/parent area ratio for approximately 25 individual grains from Fig. 5.7. All grains which contain twinning systems of 64.30°, 76.70° and 84.70° or a combination of these within a single grain were included in this graph. It is clear that there are grains with a high Schmid factor which do not contain any twins. On the other side, all twinned grains have a Schmid factor higher than 0.35. Fig. 5.8 also shows that there is no correlation between the amount of twinning strain and the Schmid factor of a particular grain, since a wide distribution of the twinned area fraction (from 4 to 11 %) was observed in the 0.35–0.5 range of the Schmid factor. The fact that mostly compression type of twins is observed could be explained by the present texture. It has been reported that CP Ti plate has a strong alignment of the basal planes of the grains parallel to the rolling plane [31].

A similar analysis has been performed for the bottom area of the MF plate. Fig. 5.9 shows the IQ map with highlighted twins and the orientation deviation angle map of the bottom section of the MF sample. This part of the plate experienced mainly tension (see Fig. 5.3). Similar to the top section, high deformation was found to be ranging from a depth of approximately 500 μm to the outer bottom edge surface. The majority of deformation is attributed

to twinning and localized strain associated with twins in their vicinity. The most prominent twinning deformation system was the 84.70°, while a minority twinning system was found to be 34.80°. A small amount of 64.30° compression twinning was also observed. When the number of twins observed in Figs. 5.6 and 5.9 are compared, it may be concluded that much more twins generated near the surface underwent a tensile strain. This may, however, be attributed to the lesser twinning shear component needed for nucleation of the 84.70° twinning system [32].

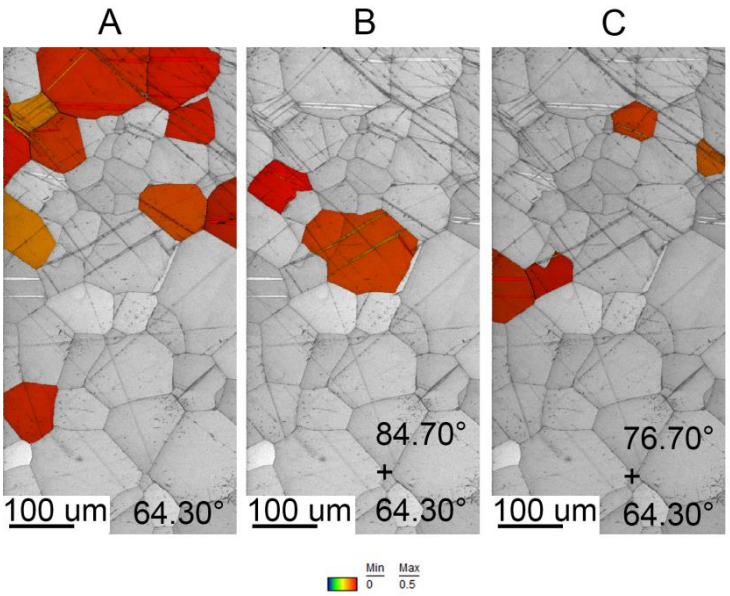

Fig. 5.7: Highlighted grains with different twinning systems and their Schmid factor values for the top section of mechanically formed plate.

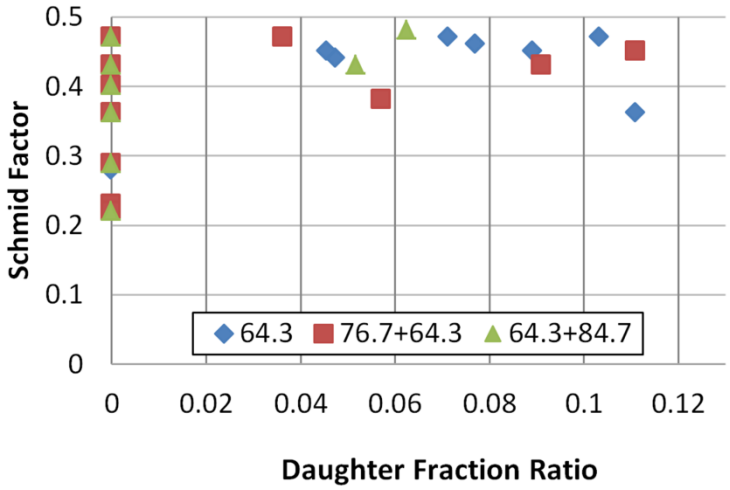

Fig. 5.8: Schmid factor of selected grains versus their daughter/parent area ratio for the top part of mechanically formed plate.

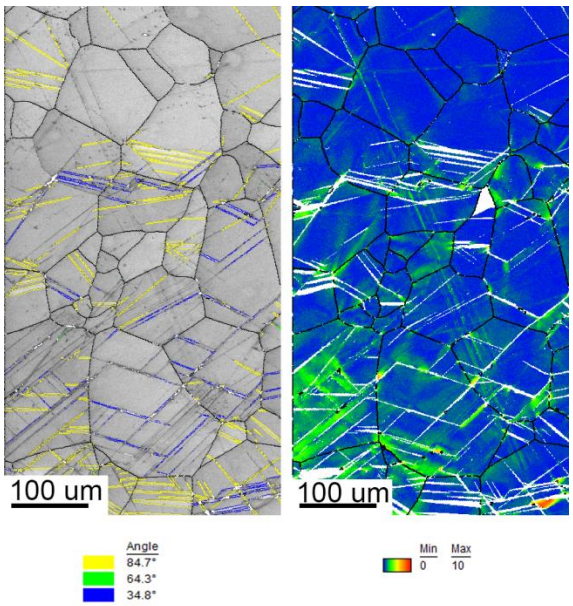

Fig. 5.9: Image quality map with highlighted twins of different types (left) and orientation deviation angle map (right) for bottom part of mechanically formed plate.

Similarly to the top section, twinning distribution was also evaluated for approximately 30 individual grains. Single active twinning modes of either 84.70° or 34.80° within a single grain have a lower quantity compared to a combination of twin systems that contained both of the 84.70° and 34.80° twinning. Additionally, the Schmid factor was also evaluated for each of these individual grains that contained twinning. Comparable to the top section, a high Schmid factor is associated with twinned grains at the bottom of the MF plate. Fig. 5.10 shows the Schmid factor versus daughter/parent area ratio calculated for approximately 38 individual grains. Grains which contain only 84.70° or 34.80° twin systems and a combination of both 84.70° and 34.80° twins were plotted. The spread of approximately 5–36 % is observed for an individual grain, while 34.80° and 34.80° + 84.70° twin systems ranged between 5 to 15 %. When only the 84.70° twin is present within an individual grain, it tends to occupy more area by broadening as the Schmid factor increases. It is suspected that when only the 84.70° twin mode is present, it tends to nucleate, propagate and grow faster compared to when different twinning systems are active within the same grain.

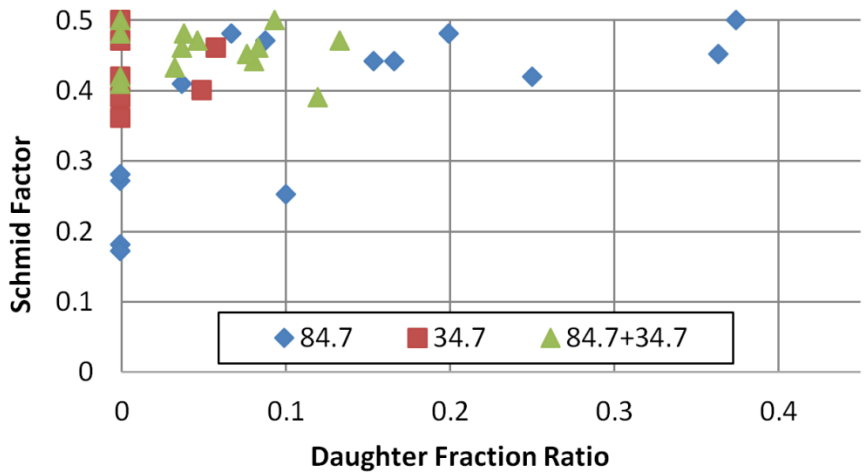

Fig. 5.10: Schmid factor of selected grains versus their daughter/parent area ratio for bottom part of mechanically formed plate.

5.2.5 Laser Forming

Fig. 5.11 shows the IPF maps, IQ maps with highlighted twins and orientation deviation angle maps of the top and bottom sections of the LF specimens. During this complex forming process, the specimen experiences deformation due to heating and cooling cycles, which gives rise to multiple microstructural changes. These changes can be slip, grain fragmentation, recovery, grain boundary sliding due to alpha-to-beta transformation, phase transformation recrystallization and twinning. Fine-grained acicular alpha structures were found on the top of the specimen followed by a columnar grain growth towards the center. Moreover, the microstructural boundaries can also be described as irregular grain sizes and serrated with interlocking grain boundaries. Random fine-grained acicular and columnar grains exhibit grain boundaries with non-coherent twinning, more specifically the 57° compression twin. This could be attributed to the cooling down process (contracting) of the material during which twinning systems formed and were then distorted thereafter due to the ongoing slip deformation. A small amount of 84.70° and 34.80° tension twinning modes were also recorded at the top and bottom. The orientation deviation angle maps in Fig. 5.11 also show the deformation changes within a single grain and throughout the specimen. More importantly, the deformation mechanism in the LF process is deformation at high temperatures by dislocations through the whole thickness.

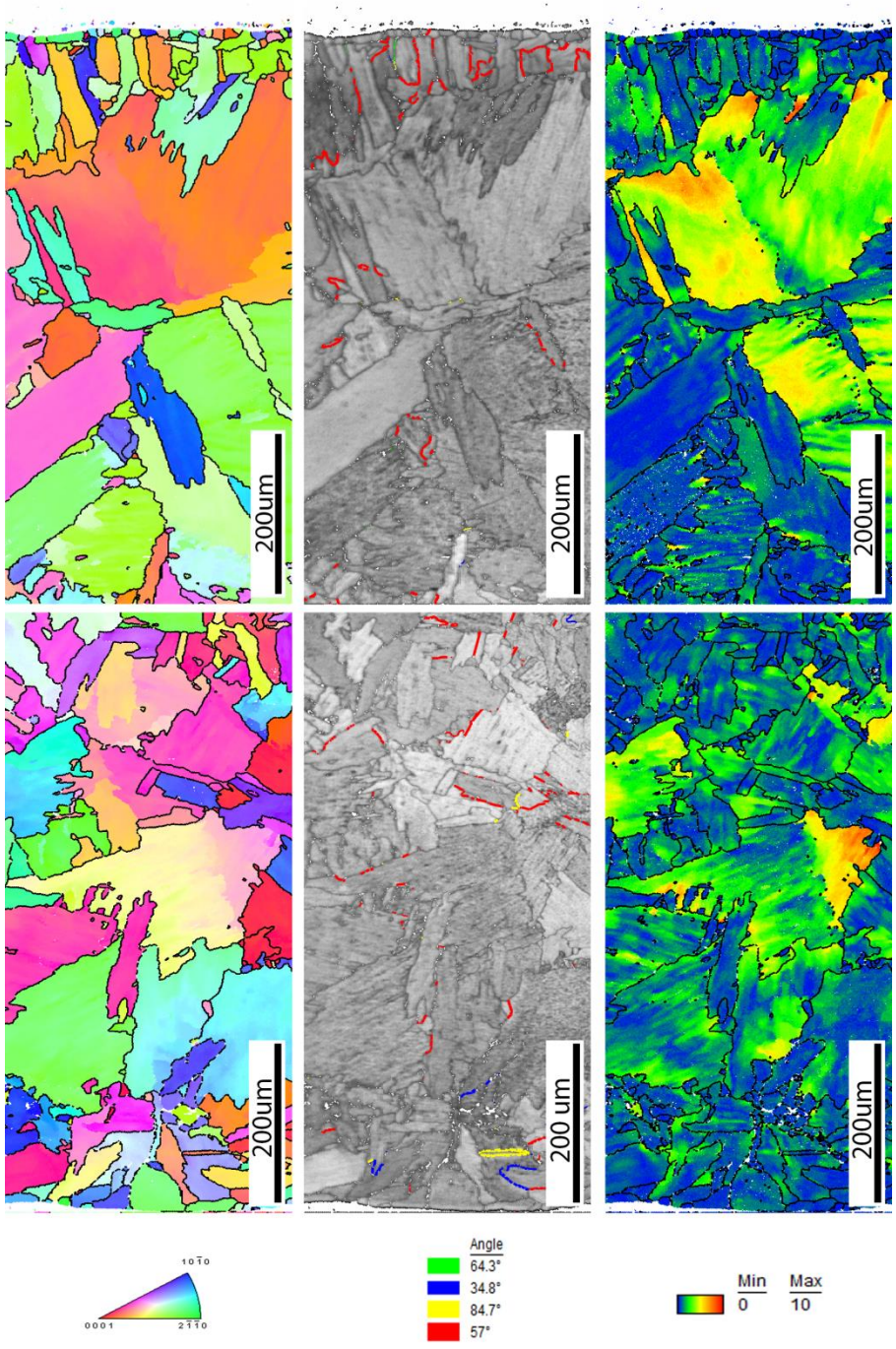

Fig. 5.11: OIM [001] inverse pole figure map (left), image quality map with highlighted twins (middle), orientation deviation angle map (right) at the top (top) and the bottom (bottom) of laser-formed sample.

5.2.6 Laser-mechanical forming

The LM method was included to achieve a midpoint process between laser and mechanical processes. It can also be used to compare the laser and mechanical forming processes and assess the interface behavior between the laser forming microstructure after mechanical deformation. Furthermore, this technique demonstrates when LF is used to achieve a rough desired shape after which the MF process is used to complete the final shape when LF was not capable due to geometric constraints.

Due to a faster scanning rate and the lower number of scans per location, a more relaxed radius of 240 mm was produced compared to the 120 mm radii of the LF process. Fig. 5.12 shows the IPF maps, IQ maps with highlighted twins and orientation deviation angle maps of the top and bottom sections of the LMF specimen. The IQ maps revealed a more refined microstructure at the top region compared to the LF process due to the lower heat input. However, the microstructural changes at the top part of the plate have a similar behavior to that of LF. It can be concluded that the higher scanning speed resulted in a finer acicular alpha phase.

Furthermore, the orientation deviation map from the top part of the plate showed a similar trend to that of the LF process, but again with a more refined/localized arrangement. Twinning was also observed in the refined microstructure of the top section which may be attributed to the mechanical forming which followed afterwards. The most active twinning system in the top section was the tensile 84.70° mode with a minority of 64.30° and 57° twin systems. The bottom section of the LMF sample shows an equiaxed alpha grain structure with traces of twinning and slip deformation which is similar behavior to that of MF. Only the 84.70° tensile systems were detected in the bottom section. As shown in the experimental results (p 77), Fig. 5.4D shows a distinct line that separates the finer acicular and equiaxed grain microstructure. This line appears at a depth of ~ 1.5 mm from the top surface. It is suspected that this line separates the volume which experienced alpha–beta–alpha allotropic phase transformation during the thermal cycling from the bottom part of the plate, where the local temperature does not achieve the value required for such transformation. Twinning distribution was recorded for all grains which have visible twinning in the LMF bottom section. Twinning behavior is similar to that of the MF specimen, i.e. twinning volume and broadening due to the tension deformation.

Individual Schmid factors were calculated for individual grains which showed correlation between twinned grains and a high Schmid factor.

Individual grains were used to calculate the Schmid factor versus daughter/parent area ratio for the bottom section as shown in Fig. 5.13. The parent grain area that contained daughter twinning modes where plotted to represent the twin area covered for each individual grain. The area ranged from approximately 1.5 % to as high as 9.5 % covered by the twin system within the grain. Similar to that of the MF process, the 84.70° twin system tends to occupy more area as the Schmid factor increases. Interestingly, the LMF process occupied approximately half the twinned area compared to the MF process.

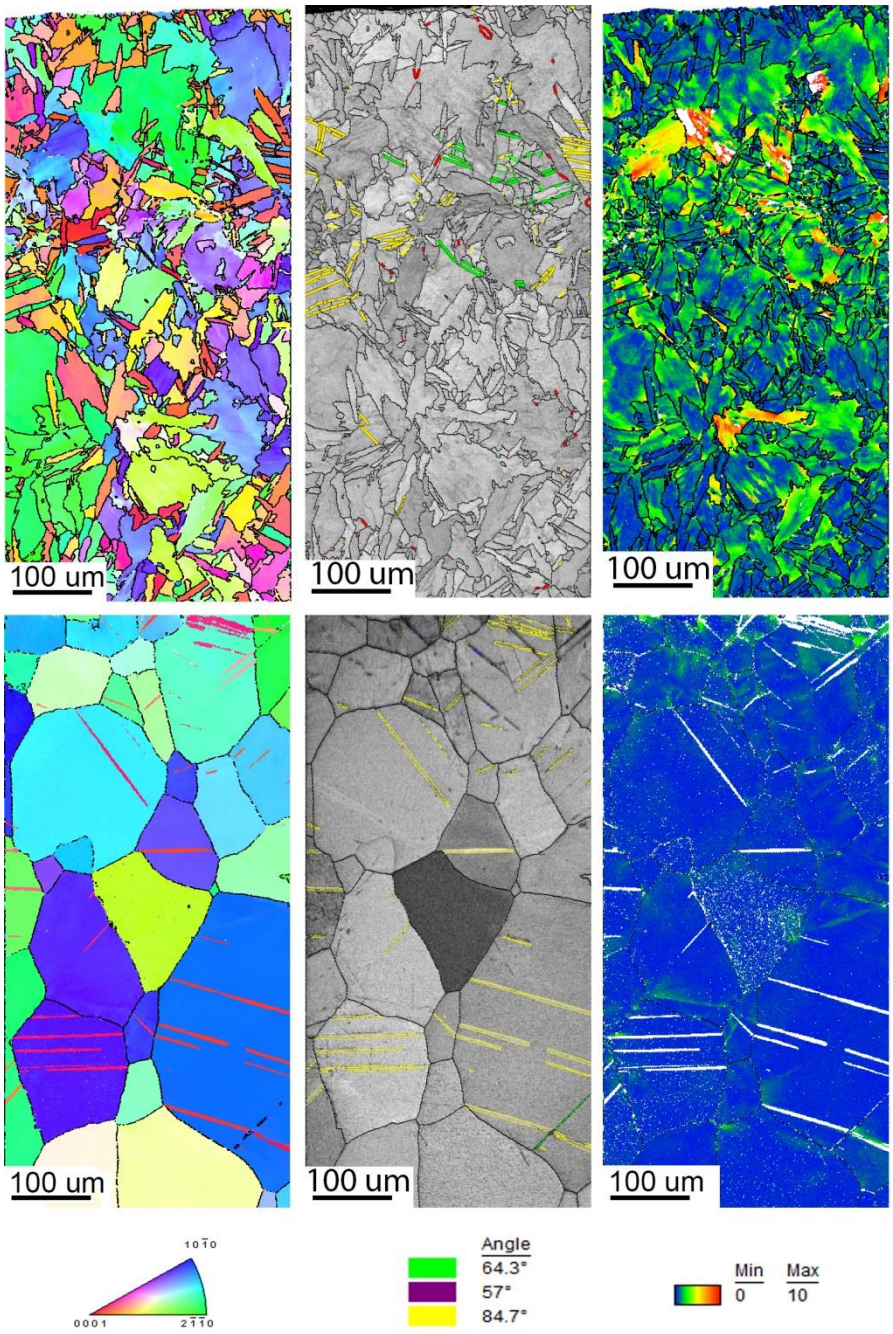

Fig. 5.12: OIM [001] inverse pole figure map (left), image quality map with highlighted twins (middle), orientation deviation angle map (right) at the top (top) and the bottom (bottom) of laser–mechanical formed sample.

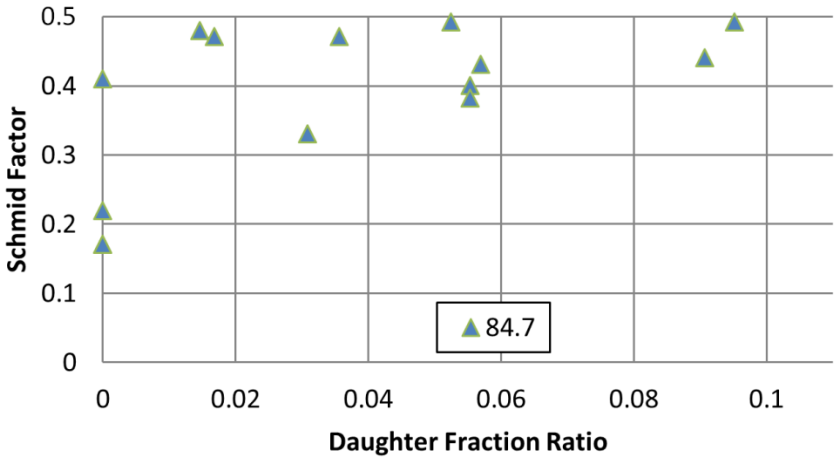

Fig. 5.13: Schmid factor of selected grains versus their daughter/parent area ratio for the bottom part of laser–mechanical formed plate.

5.3 Discussion

A general observation is that laser forming utilizes plastic deformation at high temperatures, while mechanical forming at room temperature is characterized by plastic deformation at low temperature. The present results show a large variation between the microstructural deformation upon comparing the traditional MF to that of the LF. Overall, the MF top and bottom sections displayed predominant twinning deformation. More specifically, the top section that experienced compression due to external loading gave rise to a majority of compression twinning systems. The bottom section displayed similar trends, as the majority of twinning was tensile. Grain size seemed to play a role in deformation twinning if twin nucleation and propagation developed, as some grains did not show evidence of twin deformation. For twinned grains, the number of twins increased with an increase in grain size although not all grains contained twins. Twin thickening is observed for the compression and tensile twin systems.

However, it would appear that if a single twin system is present within a grain, it tends to broaden more compared to multiple twin systems within a single grain. This may be attributed to the resolved shear stress component distributing easier through the grain when it is subjected to a single twinning mode compared to multiple twinning modes under tension/compression of the parent crystal. Moreover, when a grain contains

multiple twinning systems (compression and/or tensile), it would appear that only one variant is favored, as that particular variant occupied more twinned area within the individual grain. However, it is worthwhile mentioning that back-stress within the grain will have an influence on the twinning behavior. Comparison of the Schmid factor with each observed twinning system within the individual grains revealed that twins are observed at higher Schmid factors. No correlation is observed between the Schmid factor and daughter fraction ratio when subjected to a compression force (top section) giving an onset to compression twinning. A similar response is also observed at the bottom section when either the 34.80° or a combination of 34.80° and 84.70° is present when subjected to a tensile stress. However, when only the 84.70° twin system is present within an individual grain, correlation is seen between the daughter fraction ratio and an increase in the Schmid factor.

Laser forming utilizes a transient temperature distribution in order to produce contactless deformation. This process utilizes thermal stresses established in the material to yield a bending behavior using the material thermo-physical and thermo-mechanical properties. The effect of this process on the microstructure can be seen in the IPF maps and orientation deviation angle maps in Figs. 5.4, 5.11 and 5.12. Single grains exhibit heterogeneity in the deformation behavior after recrystallization. More importantly, data show that the bigger grains can exhibit misorientations of up to 17° (point to origin) within an individual grain due to heterogeneity. As a result, higher strain storage can lead to an increase in residual stresses and can have a negative influence on the fatigue life of the component [13] for CP Ti. A heat treatment for stress relieve could benefit the LF components afterwards.

During LF, the material's yield strength becomes lower as a result of increasing temperature and can be more easily plastically deformed, which will result in a higher bending angle. Important material properties such as the increase in the thermal expansion coefficient and a decrease in value of the product of heat capacity and density can assist the bending response during the LF process [33]. However, the previous research in LF excludes the phase change effect that can occur during the heating cycle. Additionally, analytical and finite element models [8] for the TGM, BM and UM that describe the bending angle prediction do not take the phase transformation effect into account. Phase transformation can give onset to either a decrease or increase in density. This phenomenon is graphically described in Fig. 5.14. The top part of Fig. 5.14 describes the first stage of laser forming via TGM as explained in the literature [8, 10]. However, when heated HCP material

experienced temperature over phase transformation temperature, the local temperature thermal expansion is superposed with a change in volume due to the phase change. This effect is depicted in the middle part of Fig. 5.14. If the phase transformation is associated with a decrease in density, then a positive contribution to the local thermal expansion (ε_{th}), plastic deformation (ε_{pl}) and bending moment (M) could be expected. The bottom part of Fig. 5.14 only shows the second part of the process, i.e. when cooling occurs, and the material is positively bent.

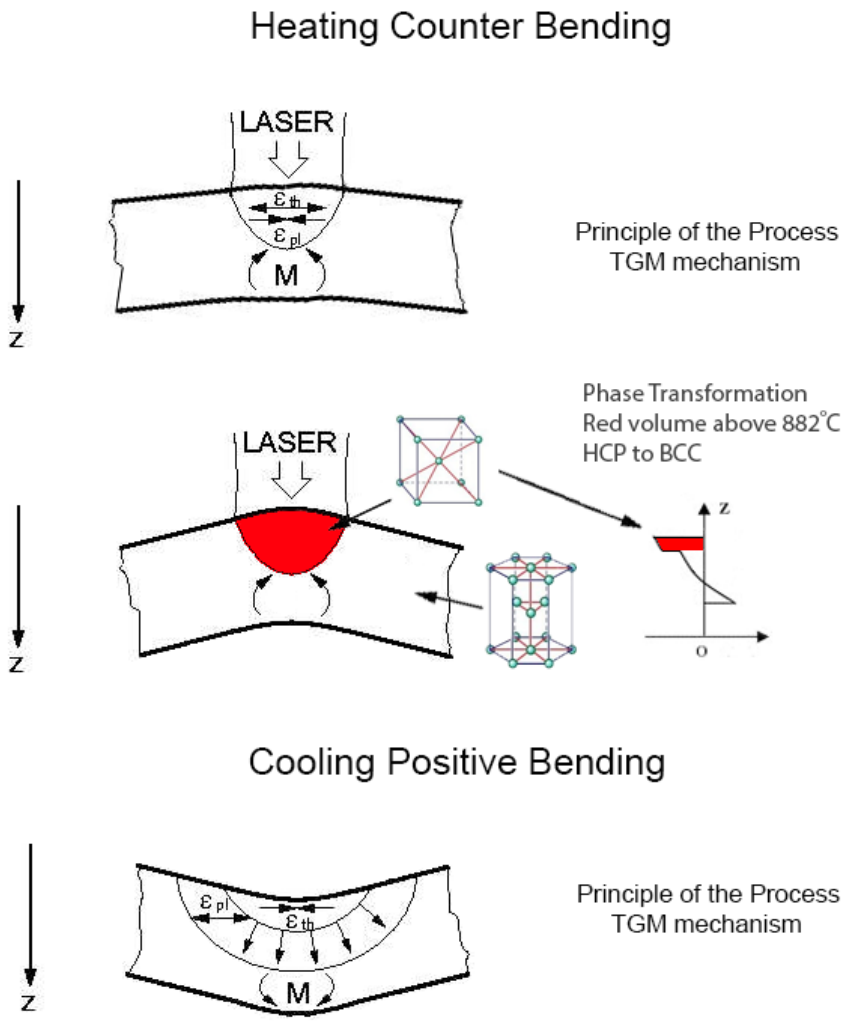

Fig. 5.14: Schematic of temperature gradient mechanism of laser forming process with the phase transformation effect through thickness of specimen.

To estimate the phase transformation effect in CP Ti, a density calculation comparison can be done. The density of a phase at room temperature is ~ 4.507 g/cm^3 [34]; however, the density changes to ~ 4.41 g/cm^3 when heating occurs from room temperature until 885°C due to the thermal expansion. The density of the β phase at 885°C has been reported to be ~ 4.35 g/cm^3 [34], hence, resulting in a density decrease of ~ 1.3 % at the same temperature. If no phase transformation occurs in the material, the α phase would have to be heated to ~ 1433°C to achieve the density of 4.35 g/cm^3, leading to an increase in temperature of approximately 548°C.

Phase transformation can either assist the response of the bending angle or have a negative/counter effect on the bending angle. Consequently, there is a need to alter the bending response by including the role of phase transformation during LF in the constitutive modelling approach.

A first order approach is used to calculate the heat dissipation temperature throughout the thickness of the samples during the application of the LF process. This can be correlated with the forward looking infrared radiometer (FLIR) camera for the top surface and pyrometer used for the bottom surface. The applicability of a basic equation for heat flow (Eq. (5.1)), giving the relationship between the initial surface temperature, T_0 and the sub-surface temperature, T, as a result of the laser heat input was explored in [35]. Experimental data was used for the initial temperature T_0 that was recorded by the FLIR camera before each heat cycle. At any depth z below the center of the beam and any time t, the temperature field $T(z,t)$ is given by (see Chapter 3, Eq. (3.32), ignoring for the moment the finite width in the y direction):

$$\delta T(z,t) = T - T_0 = \frac{AP / v_l}{2\pi K\sqrt{t(t+t_0)}} \exp\left[-\frac{1}{4\kappa}\left(\frac{(z+z_0)^2}{t}\right)\right] \tag{5.1}$$

where K is the thermal conductivity (16 J.s^{-1}.m^{-1}.K^{-1}), A the absorptivity of the surface (0.7), κ the thermal diffusivity (6.58 x 10^{-6} m^2.s^{-1}) and z_0 is the distance over which the heat can diffuse during the beam integration time (0 – 3.2 mm).

Fig. 5.15 shows the maximum temperature through the thickness of the specimen for the LF process. Using the LF initial recorded temperatures (T_0), the theoretical approach indicates a temperature $T(z)$ of ~ 940°C on the 6th scan at a depth of 3.2 mm. The pyrometer recorded temperatures ranging from 900 °C to 1000 °C at the bottom section, which is in close

approximation to the theoretical value. Using the same approach, Fig. 5.15 also shows the theoretical maximum temperature though the thickness of the LMF process using the initial temperatures, T_0, that was recorded by the FLIR camera. At a depth of 2 mm, the calculated temperature shows a value of ~ 875 °C which is 10 °C below the allotropic phase transformation. Therefore the distinct microstructural changes observed from the top side (0 mm) to a depth of approximately 1.5 mm in Fig. 5.4D (p 77) are due to the phase transformation.

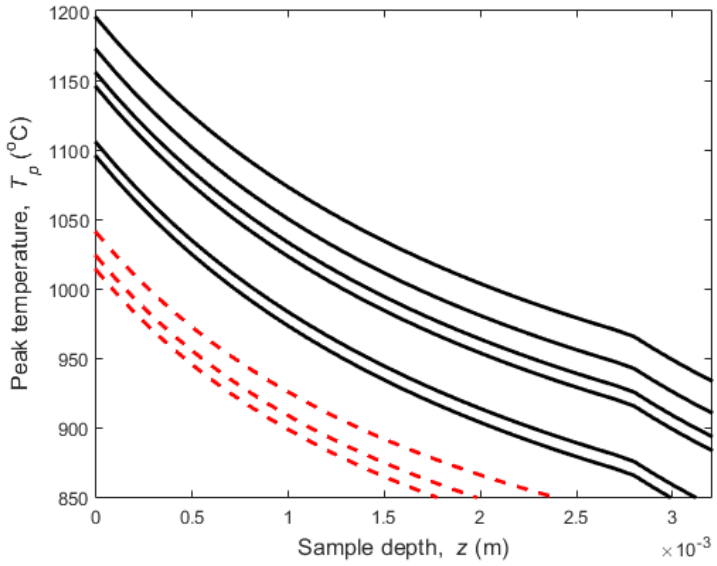

Fig. 5.15: Maximum temperature through the thickness of the specimen achieved during subsequent scans for laser forming process (full lines) and laser–mechanical forming process (dashed lines).

5.4 Conclusions

A correlative comparison is presented between classical mechanical forming and laser forming utilizing the EBSD method for obtaining specific microstructural differences within commercially pure titanium. Furthermore, laser–mechanical forming was introduced to investigate the changes within the microstructure. The differences can play a critical role during the service life of the material and may offer industry supporting information when choosing advanced forming techniques.

The mechanically formed microstructure showed predominantly coherent twinning modes. Laser forming can be a practical process for shaping pure titanium, especially as it is a local, fast and contactless process which can be easily operated by optical means. Microstructural changes, however, do show a high degree of dislocation glide deeply inside the top and bottom sections due to the thermal stresses and induced local plastic buckling. The combined forming process produces results consisting of a mixture of that obtained for the laser forming and mechanical forming processes, while no microstructural tearing or voids developed after the mechanical forming.

As expected, it was found that the processing parameters play a critical role in the microstructural changes as the cooling rate dictates the microstructural behavior for the laser forming process.

1. A general conclusion is that laser forming utilizes plastic deformation at high temperatures, while mechanical forming at room temperature is characterized by plastic deformation at low temperature. Very different final microstructures are achieved in materials which exhibit a change in mechanism of response with temperature (such as titanium).
2. Laser-formed specimens show a high degree of heterogeneity throughout the material which will result in higher residual stresses. Therefore, it is anticipated that the mechanically formed specimens would produce a better service life (strength, fatigue life) than the laser-formed specimens. However, post-processing heat treatment of the laser-formed specimens could be beneficial and may lead to an enhanced strength and fatigue lifetime.
3. Alpha-to-beta transformation in Ti heating gives a decrease in density that can aid the bending response during the laser forming

process for CP Ti. This can be applied to all materials that undergo appropriate phase transformation at heating during the LF process.

5.5 References

[1] Y. Namba, Laser Forming of Metals and Alloys, in: Proc LAMP87, Osaka, 1987: pp. 601–606.

[2] K. Masubushi and W.H. Luebke, Phase II Report Laser forming of plates for Ship Construction, Massachusets Institute of technology, 1995.

[3] J. Lawrence and J. Pou, eds., Advances in laser materials processing: technology, research and applications, CRC Press, Boca Raton, Fla., 2010.

[4] K. Scully, LASER LINE HEATING., J. Ship Prod. 3 (1987) 237–246.

[5] F. Vollertsen, I. Komel, and R. Kals, The laser bending of steel foils for microparts by the buckling mechanism-a model, Model. Simul. Mater. Sci. Eng. 3 (1995) 107. doi:10.1088/0965-0393/3/1/009.

[6] H. Arnet and F. Vollertsen, Extending Laser Bending for the Generation of Convex Shapes, Proc. Inst. Mech. Eng. Part B J. Eng. Manuf. 209 (1995) 433–442. doi:10.1243/PIME_PROC_1995_209_107_02.

[7] H. Shen and F. Vollertsen, Modelling of laser forming – An review, Comput. Mater. Sci. 46 (2009) 834–840. doi:10.1016/j.commatsci.2009.04.022.

[8] M. Geiger and F. Vollertsen, The Mechanisms of Laser Forming, CIRP Ann. 42 (1993) 301–304. doi:10.1016/S0007-8506(07)62448-2.

[9] C.L. Yau, K.C. Chan and W.B. Lee, Laser bending of leadframe materials, J. Mater. Process. Technol. 82 (1998) 117–121. doi:10.1016/S0924-0136(98)00012-0.

[10] Z. Hu, R. Kovacevic and M. Labudovic, Experimental and numerical modeling of buckling instability of laser sheet forming, Int. J. Mach. Tools Manuf. 42 (2002) 1427–1439. doi:10.1016/S0890-6955(02)00075-5.

[11] N.B. Dahotre and S.P. Harimkar, Laser fabrication and machining of materials, Springer, New York, N.Y, 2008.

[12] Yung-Chin Hsiao, Finite element analysis of laser forming, Massachusetts Institute of Technology, 1997. https://scholar.google.nl/scholar?cluster=5681393484429220906&hl=en&as_sdt=0,5&as_vis=1 (accessed January 20, 2018).

[13] A. Els, H. Fidder, S. Woudberg and P.J. McGrath, Mechanical Characterisation of the Effect of Various Forming Processes Applied to Commercially Pure Titanium, Mater. Charact. 96 (2014) 206–212. doi:10.1016/j.matchar.2014.08.012.

[14] B. Taylor and E. Weidmann, Metallographic preparation of titanium, Struers application notes, Denmark, 2016. https://www.struers.com/-/.../Struers.../Application_Note_Titanium_2015_ENG.pdf.

[15] M.J. Donachie, Titanium: A Technical Guide, 2nd Edition, ASM International, 2000.

[16] C.N. Tomé, I.J. Beyerlein, J. Wang and R.J. McCabe, A multi-scale statistical study of twinning in magnesium, JOM. 63 (2011) 19–23. doi:10.1007/s11837-011-0038-x.

[17] I.J. Beyerlein, R.J. McCabe and C.N. Tomé, Effect of microstructure on the nucleation of deformation twins in polycrystalline high-purity magnesium: A multi-scale modeling study, J. Mech. Phys. Solids. 59 (2011) 988–1003. doi:10.1016/j.jmps.2011.02.007.

[18] L. Wang, Y. Yang, P. Eisenlohr, T.R. Bieler, M.A. Crimp and D.E. Mason, Twin Nucleation by Slip Transfer across Grain Boundaries in Commercial Purity Titanium, Metall. Mater. Trans. A. 41 (2010) 421. doi:10.1007/s11661-009-0097-6.

[19] G. Proust, C.N. Tomé and G.C. Kaschner, Modeling texture, twinning and hardening evolution during deformation of hexagonal materials, Acta Mater. 55 (2007) 2137–2148. doi:10.1016/j.actamat.2006.11.017.

[20] Q. Yu, J. Wang, Y. Jiang, R.J. McCabe, N. Li and C.N. Tomé, Twin–twin interactions in magnesium, Acta Mater. 77 (2014) 28–42. doi:10.1016/j.actamat.2014.05.030.

[21] R.W. Cahn, Plastic deformation of alpha-uranium; twinning and slip, Acta Metall. 1 (1953) 49-52,IN1-IN5,53-70.

[22] Y. Xin, M. Wang, Z. Zeng, M. Nie and Q. Liu, Strengthening and toughening of magnesium alloy by {10−12} extension twins, Scr. Mater. 66 (2012) 25–28. doi:10.1016/j.scriptamat.2011.09.033.

[23] A. Fernández, A. Jérusalem, I. Gutiérrez-Urrutia and M.T. Pérez-Prado, Three-dimensional investigation of grain boundary–twin interactions in a Mg AZ31 alloy by electron backscatter diffraction and continuum modeling, Acta Mater. 61 (2013) 7679–7692. doi:10.1016/j.actamat.2013.09.005.

[24] B.E. Reed-Hill and E.R. Buchanan, Zig-zag twins in zirconium, Acta Metall. 11 (1963) 73–75. doi:10.1016/0001-6160(63)90133-0.

[25] L. Jiang, J.J. Jonas, A.A. Luo, A.K. Sachdev and S. Godet, Influence of {10-12} extension twinning on the flow behavior of AZ31 Mg alloy, Mater. Sci. Eng. A. 445–446 (2007) 302–309. doi:10.1016/j.msea.2006.09.069.

[26] A.L. Oppedal, H. El Kadiri, C.N. Tomé, G.C. Kaschner, S.C. Vogel, J.C. Baird and M.F. Horstemeyer, Effect of dislocation transmutation on modeling hardening mechanisms by twinning in magnesium, Int. J. Plast. 30–31 (2012) 41–61. doi:10.1016/j.ijplas.2011.09.002.

[27] E. Roberts and P.G. Partridge, The accommodation around {10$\bar{1}$2} 〈$\bar{1}$011〉 twins in magnesium, Acta Metall. 14 (1966) 513–527. doi:10.1016/0001-6160(66)90319-1.

[28] P.L. Pratt, Cleavage deformation in zinc and sodium chloride, Acta Metall. 1 (1953) 692–699. doi:10.1016/0001-6160(53)90027-3.

[29] H. El Kadiri, J. Kapil, A.L. Oppedal, L.G. Hector, S.R. Agnew, M. Cherkaoui and S.C. Vogel, The effect of twin–twin interactions on the nucleation and propagation of {101$\bar{2}$} twinning in magnesium, Acta Mater. 61 (2013) 3549–3563. doi:10.1016/j.actamat.2013.02.030.

[30] M.A. Meyers, O. Vöhringer and V.A. Lubarda, The onset of twinning in metals: a constitutive description, Acta Mater. 49 (2001) 4025–4039. doi:10.1016/S1359-6454(01)00300-7.

[31] A.M. Garde and R.E. Reed-Hill, The importance of mechanical twinning in the stress-strain behavior of swaged high purity fine-grained titanium below 424°K, Metall. Trans. 2 (1971) 2885–2888. doi:10.1007/BF02813267.

[32] M.H. Yoo, Slip, twinning, and fracture in hexagonal close-packed metals, Metall. Trans. A. 12 (1981) 409–418. doi:10.1007/BF02648537.

[33] Y. Guan, S. Sun, G. Zhao and Y. Luan, Influence of material properties on the laser-forming process of sheet metals, J. Mater. Process. Technol. 167 (2005) 124–131. doi:10.1016/j.jmatprotec.2004.10.003.

[34] G. Welsch, R. Boyer and E.W. Collings, Materials Properties Handbook: Titanium Alloys, ASM International, 1993.

[35] M.F. Ashby and K.E. Easterling, The transformation hardening of steel surfaces by laser beams—I. Hypo-eutectoid steels, Acta Metall. 32 (1984) 1935–1948. doi:10.1016/0001-6160(84)90175-5.

Chapter 6

In-situ digital image correlation observations of laser forming

6.1 Introduction

In this study experimental and modelling methods were used to examine the microstructural and bending responses of laser formed commercially pure titanium grade 2. The in-situ bending angle response is measured for different processing parameters utilizing 3D digital image correlation. The microstructural changes are observed using electron backscatter diffraction. Finite element modelling is used to analyse the heat transfer and temperature field inside the material.

The work shows that the laser bending process is controlled by processing parameters such as laser power and laser beam scanning speed, but also by surface absorption. Grain size appears to have no influence on the final bending angle; however, sandblasted samples show a considerably higher final bending angle. Experimental and simulation results indicate that the laser power has a larger influence on the final bending angle than the laser beam velocity. The microstructure of the laser heat affected zone consists of small refined grains at the top layer followed by large elongated grains. Deformation mechanisms such as slip and twinning were observed in the heat affected zone, where their distribution depends on particular processing parameters.

6.2 In-situ digital image observations of laser forming

Laser forming (LF) was first reported in the 1980's within the ship building industry using flat steel plates which has been formed into three-dimensional shapes as reported by [1,2]. It was also further reported that laser forming can advocate as a highly versatile tool for a broad range of material processing applications. LF is a contactless method of producing controlled deformation of metallic and non-metallic structures through introducing laser energy at specific parameters as described by [3,4]. LF can be described as a process in

which thermal stress is introduced into the substrate structure by means of a laser beam. This results in quick local heating without melting. Thermo-elastic plastic distortions will occur due to the onset of thermal stresses (temperature and geometry dependent) exceeding the yield elastic limit (temperature dependent) of the substrate material. The laser is then switched off or shifted in a specific pre-determined pattern which plays an important role in the final shape that will result after cooling. The cooling will lead to the start of bending or shape change of the material substrate. The three bending mechanisms that are associated with LF are the temperature gradient mechanism (TGM), the buckling mechanism (BM) and the shortening or upsetting mechanism (UM) as proposed by [5,6]. In this study the TGM will be dominant since the substrate is considered to be a thick plate i.e. due to the ratio between thickness of the substrate and the depth of laser beam heat affected material. Furthermore, laser forming has numerous processing parameters such as transverse speed, laser beam diameter, distribution of power density (for example TEM_{01}) and wavelength. The physical properties of the material and surface such as the absorption coefficient, crystallographic orientation, thermal conductivity and thermal expansion also play a vital role in the final desired shape of any material that will undergo LF. The selection of the above-mentioned processing parameters is therefore crucial as previously reported by [7,8]. More recent studies deal with laser forming involving, e.g. the edge effect [9], three dimensional laser forming [10,11] and modelling of multiple scans [12]. However, these studies fall beyond the scope of the current investigation.

A two layer TGM model has been used in numerous comparative studies as stated by [3]. There are also a number of analytical models available as given by [4, 5, 13] that have been developed to describe and expand on the main LF mechanisms associated with the TGM. One of the analytical bending angle models (e.g. [4]) assumes a delivered energy approach to the temperature field and results in the following formula for the final bending angle:

$$\alpha_b = \frac{3\alpha_{th} A}{\rho c_p s^2}\left(\frac{P}{v_l}\right) \tag{6.1}$$

where α_{th} is the coefficient of thermal expansion, P is the laser power, A is the surface absorption coefficient, ρ is the material density, c_p is its specific

heat capacity, v_l is the laser scanning speed or beam scanning velocity and s is the sample thickness. The model was extended by [14] to include the counter-bending effect in order to account for some of the purely elastic straining. The modified Vollertsen equation for the bending angle as proposed by [14] is

$$\alpha_b = \frac{21\alpha_{th}A}{2\rho c_p s^2}\left(\frac{P}{v_l}\right) - \frac{36LY}{sE} \tag{6.2}$$

where L is the half length of the laser track, Y is the yield stress and E is Young's modulus. When comparing Eq. (6.1) with Eq. (6.2), it is clear that the solution includes some material and geometrical parameters to calculate the bending angle. The bending model of [5] only takes into account laser power, sample thickness and beam scanning velocity. The model of [13] additionally takes into account the flow stress at the heated region as variable with the entire equation appearing as a cube root.

Both above mentioned approaches deal with the final bending angle observed after processing by a laser beam. However, for a better understanding, the flow of the thermal strain created during the LF process, which is driven by the TGM, a digital image correlation technique (DIC) [15] could be applied in-situ to characterize the movement made by the specimen during processing. Emphasis may be placed on any disordered movement and torsional moments that may lead to an offset when compared to the initial stage. An advantage of DIC is that it can also be used to evaluate any sudden movement during the heating and cooling period.

Furthermore, commercially pure (CP) Titanium (Ti) experiences an allotropic phase transformation throughout the LF process as the material is heated above the alpha to beta region which is associated with a volume change and therefore influencing the LF process as shown in previous Chapter and reported by [8]. This phase transformation always needs to be taken into account when laser processing of Ti or its alloys is studied [13 – 15]. [19] shows that changes in the deformation bending angles of up to 0.1° can occur in steel when the phase changes from ferrite to austenite. This phase transformation and all other microstructural changes developed during the LF process can be characterized with the aid of Electron Back-Scatter Diffraction (EBSD) when considering crystallographic properties of the laser heat affect zone (LHAZ) within the specimen. The study of [20] showed that the global

relieved residual stresses can be ~ 25 % higher for the LF process when compared to that of traditional mechanical forming processes. As stated in [21], local microscopic deformation resolved stress within CP Ti can be as high as ~ −180 MPa.

The novelty of our approach lies in using in-situ DIC equipment that can be used to visualize the bending angle response (e.g. counter bending, buckling, etc.) in real time when executing laser forming. Furthermore, the bending response can be linked to the microstructural changes (i.e. allotropic phase transformation, grain growth, grain misorientation changes, etc. via EBSD) within each sample that was subject to specific laser processing conditions. Furthermore, the microstructural changes can give an indication of how the flow of thermal strain was created during the laser forming process which can also be linked to the final temperature distribution within the sample. According to the knowledge of the author, the combined above-mentioned techniques and direct experimental link between bending angle and microstructural changes have not been performed elsewhere in the literature. More specifically, the bending angle response behavior will be compared for different processing parameters and different grain sizes. The surface roughness will also be altered in order to investigate the influence of an increased absorptivity coefficient due to surface sandblasting. These observations provide additional insight to the semi-empirical and analytical modelling of LF.

6.2.1 Setup method

The laser used for the laser forming process is a 3 kW Yt:YAG continuous fibre laser from IPG Photonics. The laser optics with 120 mm focal length is set to a distance of +35 mm out of the focus position, resulting in a laser beam radius of about 2.8 mm, with a Gaussian intensity distribution. Argon shielding gas flow of 15 L/min, positioned approximately 45 mm from the sample, is used to prevent any influence of oxidation on the surface during the laser forming process. The CP Ti sample is fixed with multiple clamps on one side, while leaving the other side free to move, as displayed in Fig. 6.1. The specimen with dimensions of approximately 200 mm in length, 50 mm in width and 3 mm in thickness is raised about 1 mm at the side of the clamps to avoid contact with the aluminum base to prevent any heat transfer. This is shown in Fig. 6.1 together with track 1 being the first laser track, 2 the second, up to the n^{th} laser track. Due to the fact that the plate is fixed on one side parallel to the aluminum base C (see Fig.6.1) and bending occurred along

the axis located inside the laser track, only the free end of the plate is moving, i.e. increasing the detected angle α between the side of the plate and horizontal line marked on the base C. The laser beam is scanning the plate surface along the *X* direction and the center of the beam is shifted 6 mm in the *Y* direction between every single laser track, starting with the first laser track about 50 to 60 mm from the free end of the sample. Therefore, the surface heated by the laser is always on the same *XY* plane at the start of every individual laser track.

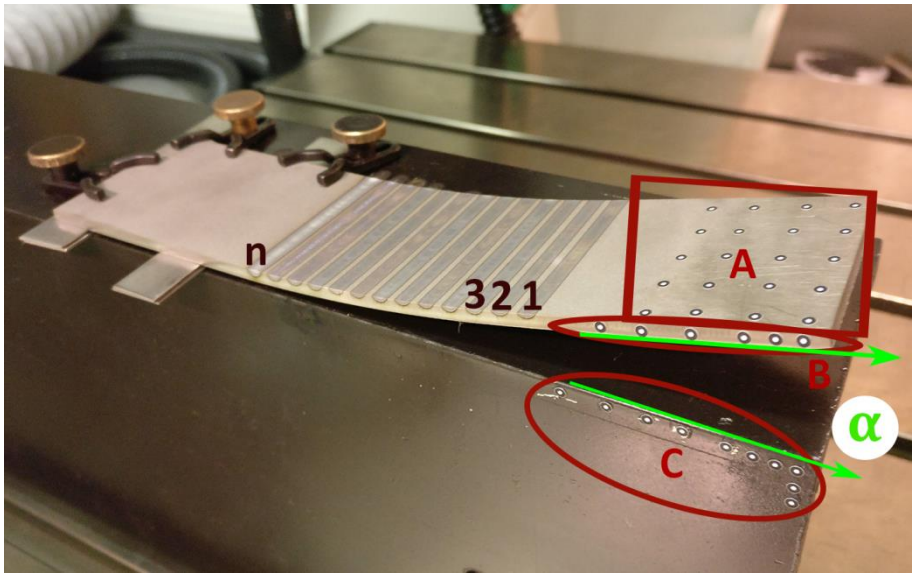

Fig. 6.1: Experimental setup for DIC observation of Laser forming sample with tracking markers for in-situ measurements on the top (A) and side (B) of the sample and on the base (C). The laser processing sequence in the X direction starts behind the markers; track #1 is followed by the 2nd and 3rd tracks until track n is reached, towards the fixed end. The angle α is the cumulative bending angle between the side sample markers line (B) and the base markers line (C). Spacers were placed below the sample at the fixed end on the left hand side to minimize any direct heat conduction from the sample into the base.

The bending angle for each individual track *i* as a function of processing time is therefore given by:

$$\alpha_i(t) = \alpha(t) - \sum_{k=0}^{i-1} \alpha_k^f \tag{6.3}$$

where $\alpha(t)$ is an instantaneous bending angle value observed during the DIC experiment, and the second term represents the accumulated final bending angle due to laser processing of all the previously processed laser tracks.

The DIC setup used for the in-situ measuring of the bending angle is a commercially available DIC-Aramis system from GOM GmbH, Germany. It is equipped with two 4 MP cameras with a resolution capability of 2400 x 1728 pixels per camera. For optimal lighting conditions, with a high intensity and contrast, two special blue lights are used. This blue light also enables the software to filter interfering ambient light and possible reflections from the laser surface processing. The frame rate used during the in-situ experiments ranged from 30 to 60 frames per second (fps). The total number of frames per track varied between 500 and 1500, depending on the scanning speed of the laser beam and the DIC frame rate. The DIC cameras were arranged in such a way that the processing laser track was always out of their field of view in order to avoid any direct beam reflection.

The samples used in the laser forming experiments are all of CP Ti grade 2. During the laser forming process, five parameters are varied namely; traverse speed, power of the laser beam, multiple 100% overlapped laser scans, grain size, and surface roughness. The laser scanning speed varied from 20, 15 and 10 mm/s, with a range of laser powers depending on the speed, as summarized in Table 6.1. This table shows only a part of the entire experimental study.

Some experiments were repeated 5 to 6 times with the same laser power and laser scanning speed to estimate variation in the final bending angle with position on the sample. The range of the laser power varied from the lowest possible setting, ~ 400 W, which would still result in bending but with minimal effect on the microstructure or LHAZ. The highest possible power setting used was ~ 1000 W before the onset of melting of the surface.

Other processing parameters such as scanning speed and beam diameter have been selected to achieve TGM conditions in all experiments. By repeating the same power, scanning speed and Y starting position settings, multiple scans with 100% track overlapping was achieved while waiting approximately 5 minutes for the specimen to cool down to room temperature before initiating the next overlap scan.

Table 6.1: Variation of power, scanning speed, final bending angle and experimental error for individual laser scans on 3 mm thick CP Ti samples. The track names are formulated by the first scanning speed followed by the laser power.

Track Name	Laser Power (W)	Laser Speed (mm/s)	Bending Angle (degree)	Experimental error (degree)
20/1100	1100	20	1.25	0.01
20/1060	1060	20	1.29	0.02
20/1000	1000	20	1.29	0.02
20/940	940	20	1.18	0.04
20/880	880	20	1.13	0.04
20/820	820	20	1.09	0.04
20/760	760	20	0.94	0.04
20/680	680	20	0.84	0.03
20/620	620	20	0.83	0.03
20/560	560	20	0.67	0.01
20/500	500	20	0.46	0.02
20/720	720	20	0.84	0.03
20/1300	1300	20	1.39	0.03
20/1400	1400	20	1.52	0.02
10/580	580	10	0.96	0.01
10/580	580	10	1.10	0.01
10/550	550	10	1.05	0.02
10/530	530	10	0.96	0.01
10/500	500	10	0.87	0.01
10/470	470	10	0.76	0.01
10/440	440	10	0.66	0.01
10/410	410	10	0.54	0.02
10/380	380	10	0.33	0.02
15/795	795	15	0.99	0.01
15/705	705	15	1.00	0.01
15/615	615	15	0.82	0.01
15/570	570	15	0.69	0.02
15/510	510	15	0.44	0.01
15/420	420	15	0.23	0.02

The influence of the grain size was tested by comparing the response of the as-received and grain grown samples during the LF process to the overall bending angle. The grain grown samples were prepared by heat-treating them for 120 hours at ~ 830°C i.e. just before the onset of the allotropic phase transformation to achieve the biggest possible grain sizes. Finally, the influence of an increased absorption coefficient was tested by lightly and evenly sandblasting the surface of the specimen to promote better in coupling of the laser radiation into the material.

CP Ti specimens were prepared for EBSD analysis as described in previous chapter using the same field emission gun, EBSD camera, EBSD data analyzed software techniques and acceleration voltage to determine the crystallographic orientations. A step size of 0.7 μm and hexagonal grid was used for measurements. During this EBSD data cleaning procedure, crystallographic orientation of no more than 2% of all scanned points has been modified.

In order to simulate the heating of the CP Ti grade 2 metal sheets with a laser beam (as heating source), a time-dependent 3D model was used in the FEM (Finite Element Method) COMSOL Multiphysics® model. The dimensions of the samples used in the model were 200 x 50 x 3 mm and a Gaussian laser power density distribution (radius of 2.8 mm) was selected. CP Ti grade 2 material properties were used. For simulation of the laser heating model the COMSOL "Heat transfer in solids" was used, which includes computation of the heat conduction, convective heat flux and general inward heat flux. The mesh used for the laser heating model was substantially refined in the area of the laser track. The model has 76005 degrees of freedom (+21662 internal). The model is solved for a time range depending on the laser beam speed, with a step size of 0.01 seconds. The processing time of the model was between 6 and 10 minutes on a standard PC. There was only one calibration constant in the FEM calculation which is the laser beam absorption coefficient. It was empirically calibrated with the experimental data by observing the first melting features in the center of the laser track.

6.2.2 Experimental results

Table 6.1 shows the range of bending angle dependence with respect to laser powers and scanning speed, which varied from 20, 15 and 10 mm/s, with an experimental error estimated from final bending angle noise ranging from 0.01° to 0.04°. By repeating the experiments (5-6 times) with the same laser

power and scanning speed, standard deviations not exceeding 10 % of the final bending angle were obtained.

The movement of the markers placed on the sample and basement during laser forming is recorded in-situ as illustrated on a single frame image in Fig. 6.2, which is at the free end of the sample. An overlay is constructed with the ARAMIS software containing the lines and angles of interest that are pre-defined from the markers. Line 1 and Line 2 are used to construct Angle 1, which is used to measure the overall bending angle from the first frame until the last frame (first/reference frame versus last frame). Also, Lines 3, 4 and 5 are used to inspect any torsional effect during the LF process by comparing them to one another i.e. Angle 2 versus Angle 3 versus Angle 4. It has been observed in all experiments that there was no difference in time response for all four pre-defined bending angles. The bending response is uniform over the whole width of the specimen during the LF process and no variances are seen for the final bending angle, therefore no torsional effect is encountered.

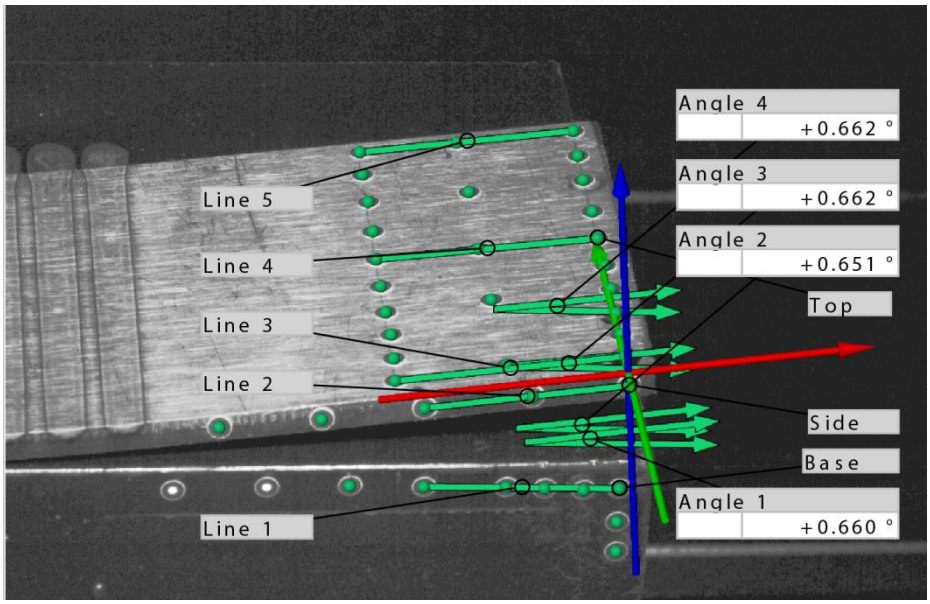

Fig. 6.2: Aramis DIC software representing a single left CCD camera frame collected during the in-situ measurement. An overlay containing the calculated angles with respect to the markers are shown.

Fig. 6.3 shows the bending angle response of three different samples and different LF processing conditions. At the beginning of each experiment the

bending angle is close to zero with a noise of about 0.01°. DIC also registers small vibrations at the instant when the laser head mechanism starts to move towards the sample. At the moment when the beam hits the sample edge, the sample starts to bend with almost a constant bending rate. Furthermore, it was observed during the bending angle response that a small amount of counter bending is present with the onset of the laser beam onto the sample. However, the data recorded in this study shows that the counter bending is not an important factor during the LF process for a 3 mm thick plate. This bending rate depends on the laser beam power and transverse speed. Close to the end of the bending process, just before the laser beam leaves the sample (between region 2 to 3 in Fig. 6.3), the bending rate is increased for a short period of time. The entire bending process of the sample stops instantaneously when the laser beam moves off the sample.

The bending angle maintains a constant value over time which includes some vibration effects due to the three axis machine movements. The vibrations are represented by small valleys and peaks during region 1 and 3. Fig. 6.3 clearly demonstrates that each combination of processing parameters results in a different final bending angle measured with an experimental error of approximately 0.01° to 0.04° as indicated in Table 6.1. For a better understanding why the bending rate changes its value, the derivative of the bending angle with respect to time of sample 15/570 shown in Fig. 6.3 is plotted in Fig. 6.4.

The bending response starts with a small amount of counter bending as predicted by [22], followed immediately by positive bending at a constant speed (region 1 to 2 in Fig. 6.4). When the laser beam moves onto the edge of the sample, the bending response accelerates (region 2 to 3 in Fig. 6.4). Studying this behavior for all possible combinations of processing parameters resulted in the conclusion that bending acceleration occurs when the laser beam approaches the end edge of the sample, where heat removal is restricted and the temperature inside the processing zone within the material is higher. The increase in bending response directly after region 1 is attributed to the rise in temperature from room conditions, which indicates the onset of the flow of thermal strain.

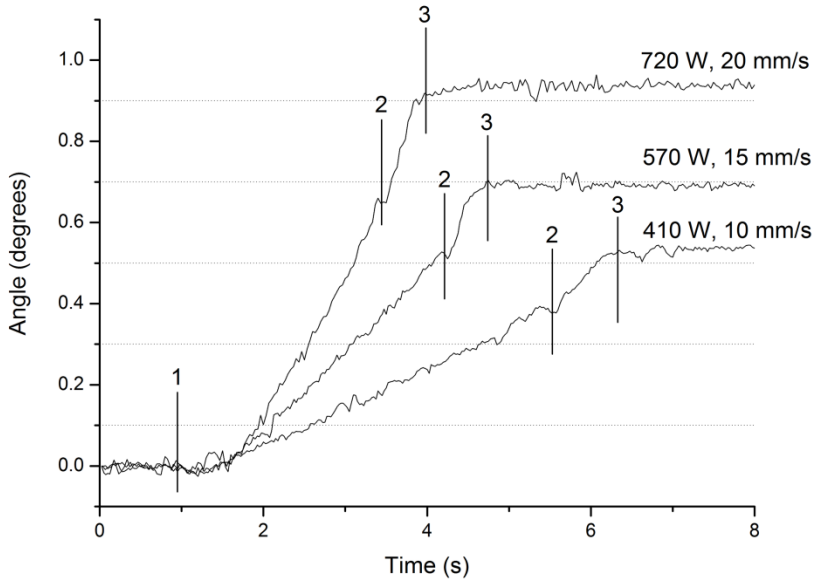

Fig. 6.3: Bending angle detected in-situ by DIC for three different processing conditions. Two distinct behaviors can be seen with respect to the slope of the bending angle in region 1 to 2 and region 2 to 3.

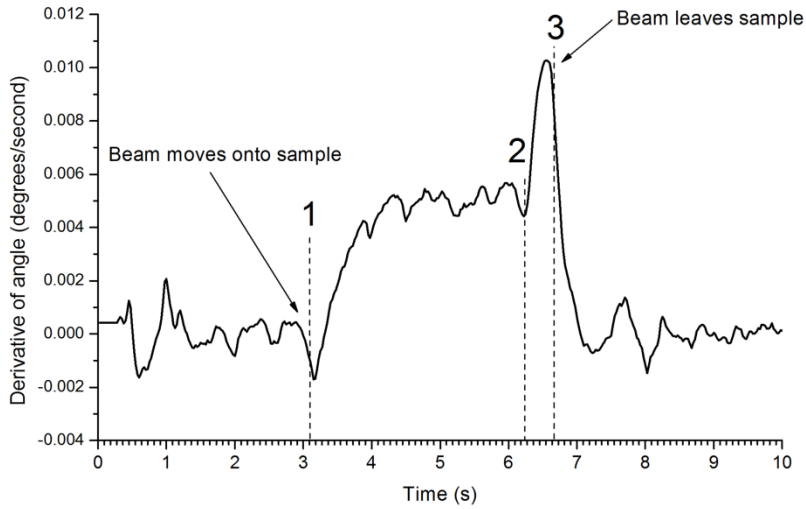

Fig. 6.4: The derivative of the bending angle with respect to time on sample 15/570 from Fig. 6.3 is shown. The bending response starts with a small amount of bending in the -Z direction, as predicted by theory, followed immediately by bending with a constant speed in the +Z direction (region 1 to 2). At the moment the laser beam moves onto the edge of the sample, the bending response accelerates.

The mechanisms by which process parameters and plate thickness affect the bending angle during the LF process are similar to that of flame heating and arc welding as described by [2]. As a result thereof, the primary factors in LF are laser power (P), scanning speed (v) and plate thickness (s). If only the laser parameters P and v would be varied in Eqs. (6.1) and (6.2), the size of the final bending angle should be, according to these models, linearly proportional to the ratio P/v, referred to as the line energy due to its dimensions (J/m) [23].

To compare the measurements for different values of laser power and transverse speed, the bending angle versus the line energy is presented in Fig. 6.5. One can clearly see that for the same transverse speed the final bending angle increases almost linearly with increasing line energy (the three surface melting data points for the 20 mm/s scanning speed should not be considered).

However, the laser bending angle in experiments with higher scanning speeds, results in a higher final bending angle for the same line energy, which is in contrast to the model proposed by Vollertsen (Eq. (6.1)). The final bending angle does not scale with the line energy parameter. Fig. 6.5 also illustrated that for each scanning speed there exists a slightly different interval of line energies resulting in a detectable laser bending angle without surface melting.

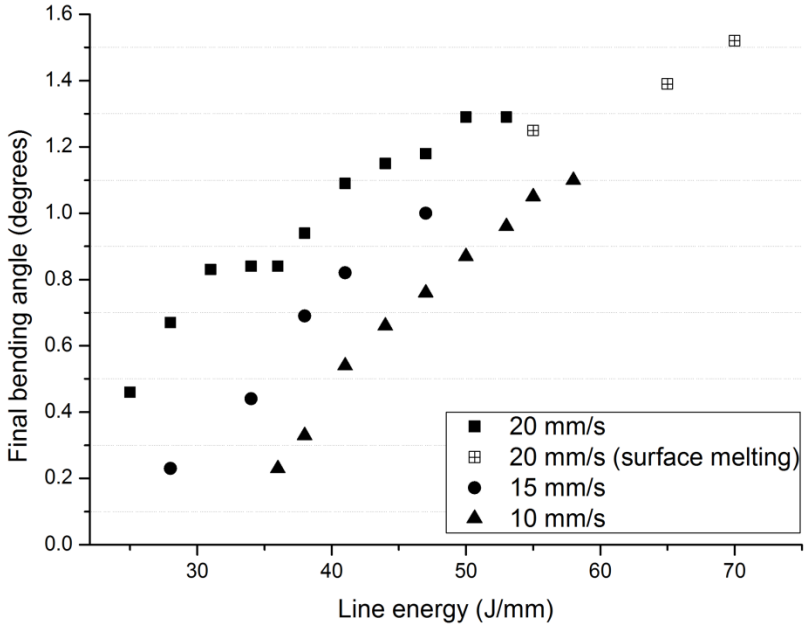

Fig. 6.5: Final bending angle versus line energy (P/v) for scanning speeds of 20, 15 and 10 mm/s. For every individual transverse speed, the bending angle is almost linearly dependent on the laser power.

Fig. 6.6 shows the successive bending angle response of different tracks with multiple overlapping scans using three different laser powers (580 W, 500 W and 410 W) at the same scanning speed of 10 mm/s. This was achieved by starting at the same *Y* position and scanning the same line multiples times.

A single line was scanned six times (100 % overlap) while waiting about 5 minutes to ensure that the sample is again at room temperature before starting the consecutive scan. All samples showed an increase in bending angle response for the second track, which after the response slowly decreases in the following tracks and tends towards and asymptotic bending angle value. The bending response shows good repeatability as it achieved almost identical values measured on two different samples using the same laser power of 410 W.

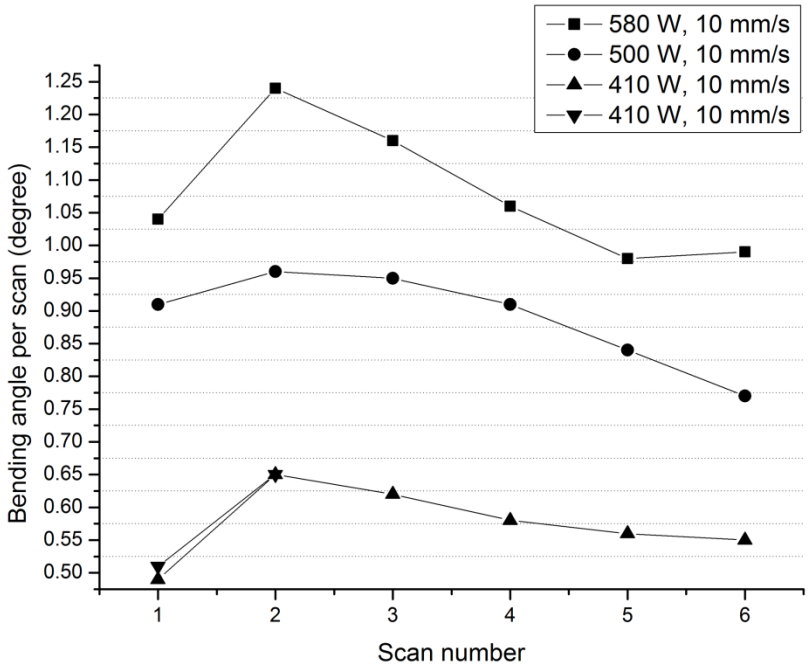

Fig. 6.6: Bending angle response of multiple overlapping tracks using three different laser powers at the same scanning speed. The total bending angle (i.e., the sum off bending angles in 6th and all previous scans) after the 6th scan for the 580 W, 500 W and 410 W is 6.46°, 5.34° and 3.45°, respectively. The total bending angle after the 2nd scan (sum of bending angle in first and second scan) for the 410 W is 1.16°.

The effects of an increase in absorptivity (by means of sandblasting the samples lightly) and grain size are shown in Fig. 6.7. Three samples, as-received, as-received with sandblasted surface and grown grains and sandblasted surface, were all laser formed with a fixed scanning speed of 15 mm/s. For the as-received and big grain, sandblasted samples the laser power was varied but not for the as-received sandblasted sample.

Three different as-received sandblasted samples were tested for repeatability thus yielding similar data points. The big grains plus sandblasted samples show a significant increase in final bending angle when compared to the non-sandblasted as-received sample, especially for lower laser powers. The as-received sandblasted samples show a similar final bending angle when compared to the grain grown sandblasted sample tested at the same laser power. This implies that the absorption coefficient is a more important factor for the bending angle response, while the grain size has only a small

influence. One of the reasons to study the grain grown sample was to see whether the allotropic phase transformation may amplify the bending during the LF process and if it could be detected by the DIC recording.

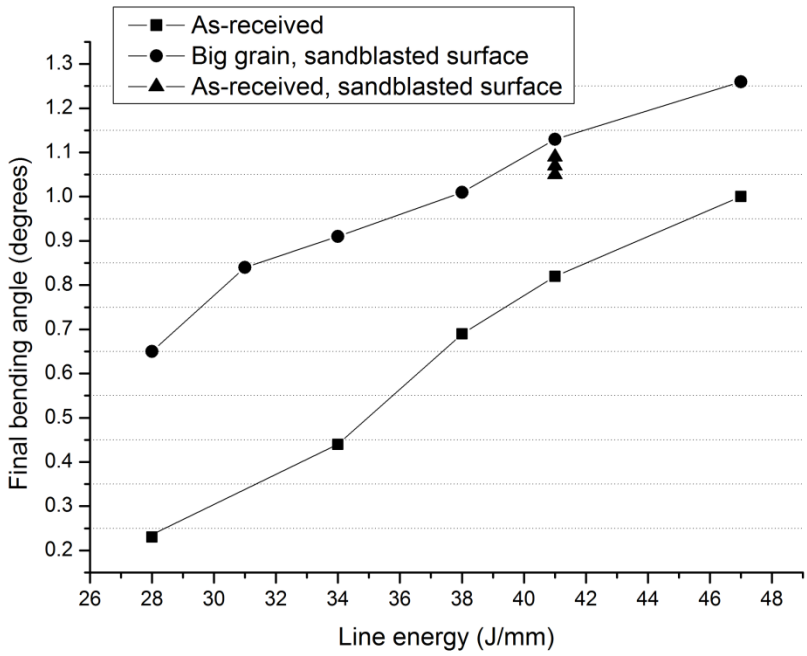

Fig. 6.7: Bending angle response comparison for the CP Ti grade 2 samples which is: as-received, as-received with sandblasted surface and sandblasted surface with grown grains. The bending response is measured at different laser powers, with a fixed 15 mm/s traverse speed for all.

Fig. 6.8 shows the [100] inverse pole figure (IPF) together with kernel average misorientation (KAM, see Chapter 2) maps for three laser powers (560 W, 720 W and 1000 W) which were subjected to the same scanning speed of 20 mm/s. Only alpha titanium has been detected inside LHAZ, similarly as in [21], where welding of CP Ti by laser has been studied. These IFP maps show grain directions parallel to the plate surface normal in a central part of the laser track (top) and under the LHAZ area (bottom). The microstructural changes within the LHAZ (starting from the top towards the bottom) are evident and similar to that reported by [8] showing that these changes can be slip, grain fragmentation, recovery, grain boundary motion due to twinning, alpha-to-beta transformation, grain growth, phase transformation and recrystallization. The LHAZ in Fig. 6.8 shows a fine-

grained acicular alpha structure on the top of the LHAZ followed by columnar grains elongated in the direction perpendicular to the surface. This behavior is seen throughout all the experiments. The depth of the columnar grains indicates the depth of the LHAZ, and this depth is shown in Fig. 6.9 for all experiments mentioned in Table 6.1.

One of the microstructural parameters studied involving transversal cross sections of laser tracks was the depth of LHAZ observed in the center of the track. Fig. 6.9 shows the relationship between the LHAZ depth and line energy. For a constant scanning speed the LHAZ increases approximately linearly with line energy. A higher scanning speed leads to a deeper LHAZ at constant line energy. These crystallographic findings of the LHAZ will be discussed in the following section dealing with EBSD.

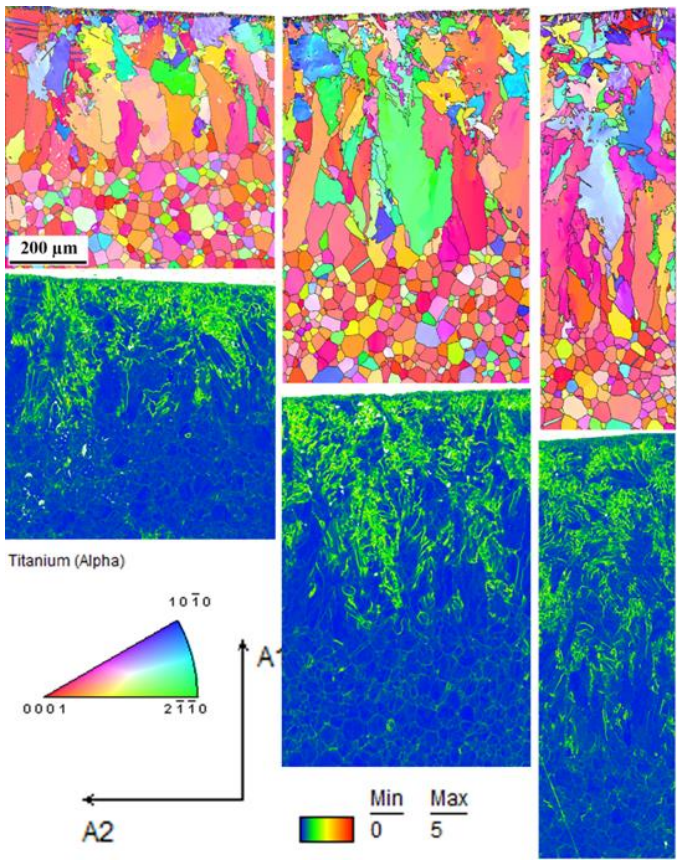

Fig. 6.8: [100] inverse pole figure (IPF) (top) and kernel average misorientation (KAM) maps (bottom) of the 560 W (left), 720 W (center) and 1000 W (right) scans with a scanning speed of 20 mm/s. The depth of the laser heat-affected zone (LHAZ) increases with an increase in laser power as indicated by the long columnar grains. No texture is observed after the forming process for all experimental results shown in Table 6.1. Scale bar 200 µm hold for all electron back-scatter diffraction (EBSD) maps in this figure.

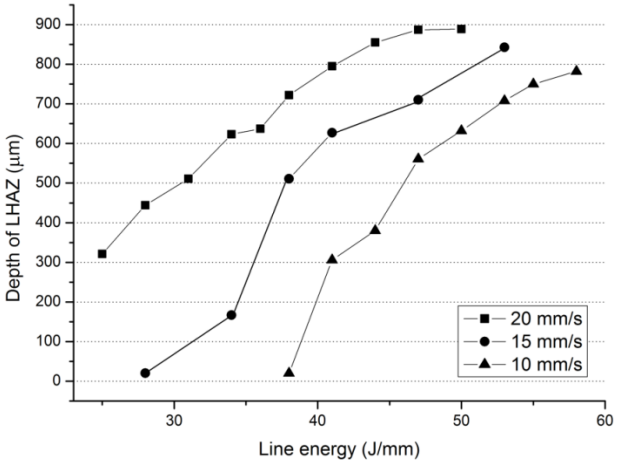

Fig. 6.9: The depth of the LHAZ microstructure compared for different values of the laser parameters, power and transverse speed, with the maximum depth plotted against the line energy.

Fig. 6.10 shows the [100] IPF and KAM maps for as-received, sandblasted, and large grain sandblasted sample tracks treated with the same laser power of 615 W and scanning speed of 15 mm/s. KAM is a well-established parameter to characterize local strain accumulated inside individual grains as described by [22]. For instance, the misorientation between a grain at the center of the kernel and all points at the perimeter of the kernel are measured. The local misorientation value assigned to the center point is the average of these misorientations. The graph on the bottom part of Fig. 6.10 shows the averaged value of KAM for a particular LHAZ depth. The as-received KAM profile shows the highest accumulated strain at the surface with a gradual decrease within the LHAZ until ~550 µm. The sandblasted sample shows approximately the same strain near the surface, less steep decrease in depth, but a sharp decrease in KAM values from depths of ~650 to 700 µm. The large grain sand blasted sample shows a significant decrease in KAM values from the top (0 µm) to ~50 µm after which it increases to the values observed for other samples. Local strain shows again a sharp change over the boundary of the LHAZ. This sudden decrease leads to very fine first order pyramidal <C+A> slip planes that emerged during the high temperature deformation. The same pyramidal slip was detected as a main mechanism for producing elongation and shortening in the c-axis direction as reported by [23]. The depth of LHAZ is the smallest for the as-received sample without sandblasting, followed by the sandblasted sample and the largest for the large grain sandblasted sample.

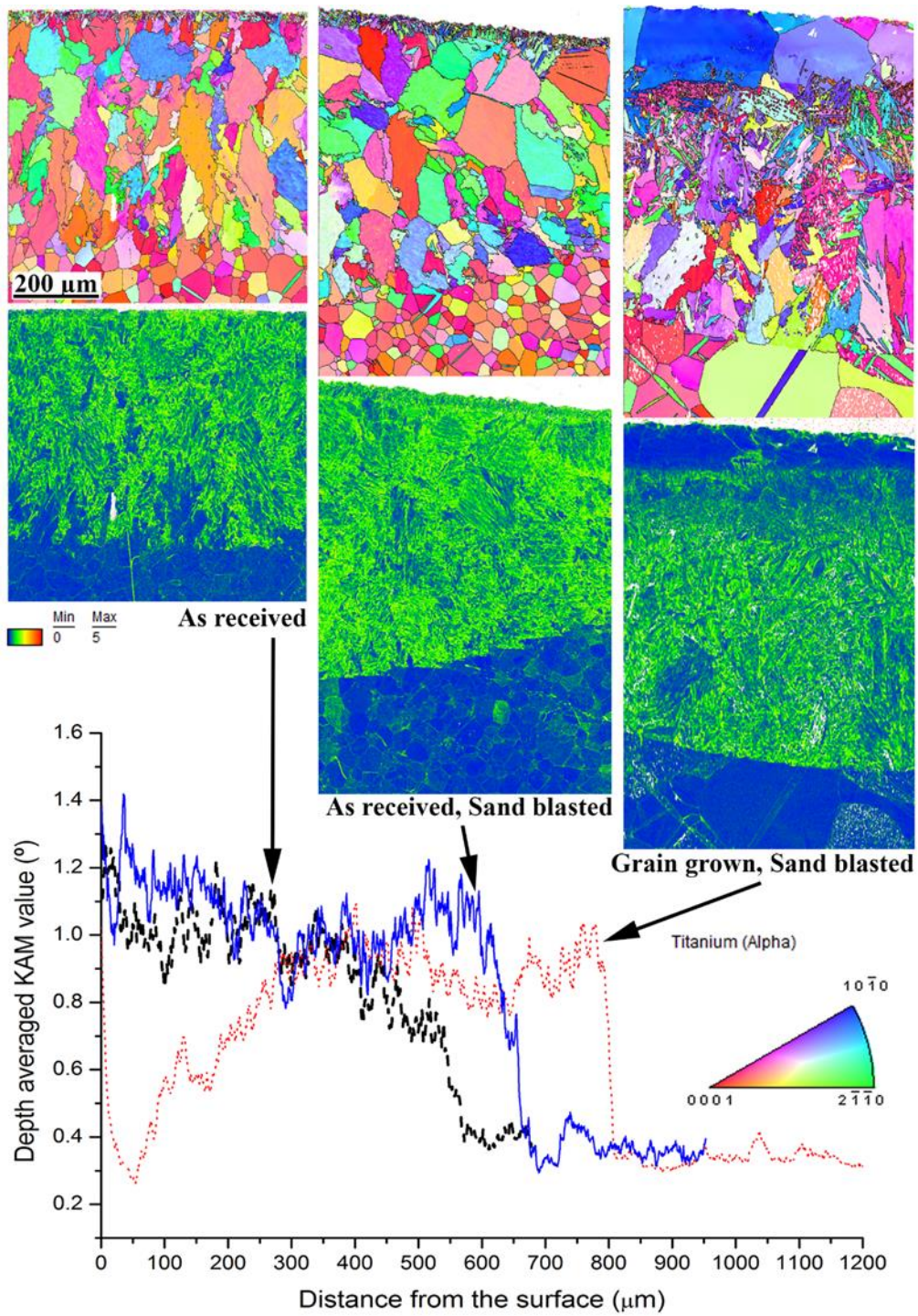

Fig. 6.10: [100] IPF and KAM maps of the central parts of the laser track transversal cross-sections for as-received (left), sandblasted (center) and large grain sandblasted (right) sample treated at 615 W and 15 mm scanning speed. Average KAM value profiles from the top surface to bottom under the LHAZ (bottom). Scale bar 200 µm hold for all EBSD maps in this figure.

The image quality (IQ) map shown in Fig. 6.11 illustrates a general response of the microstructure with depth after the LF process which is observed in all LF samples listed in Table 6.1. For this LF sample (560 W, 20 mm/s), the first 10–20 µm (Region 1 in Fig. 6.11) from the top shows a fine columnar microstructure followed by distorted grains that contain tensile and compression twining (Region 2). Region 3 gives rise to elongated columnar grain growth towards the center which indicates that phase transformation occurred until this depth. The latter phenomenon is elaborated in the discussion. Region 4 is an unaffected substrate material throughout the rest of the sample. The grain boundaries can be defined as irregular sized, jagged and interlocking with each other.

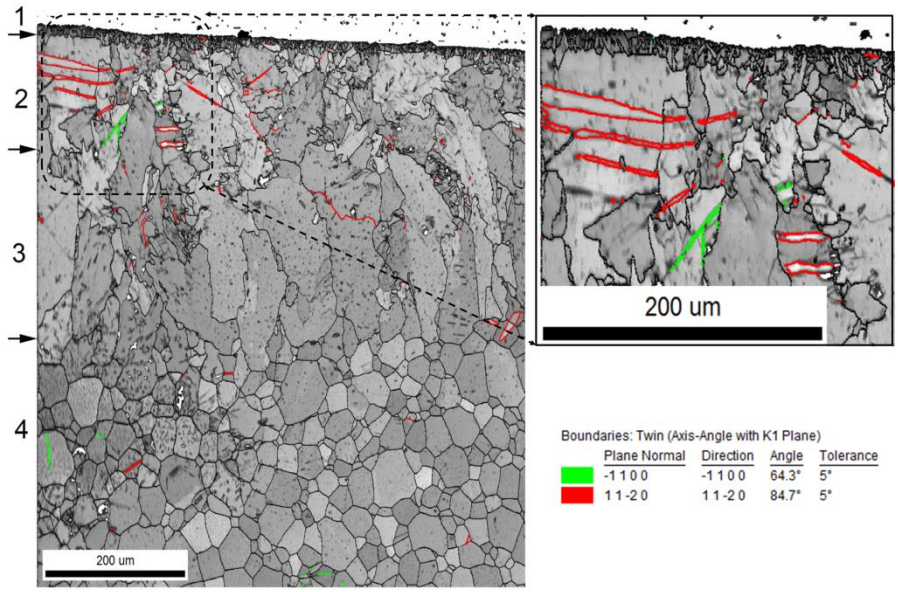

Fig. 6.11: Image quality (IQ) maps with highlighted twins and small misorientation of the cross-section of the 560 W and 20 mm/s track. The image shows four regions that are similar for all of the as-received samples that were laser formed, namely, 1—fine microstructure at the top, 2—twining with distorted grains, 3—elongated columnar grain growth towards the center, 4—unaffected substrate material.

6.3 Discussion

One would expect that the effect of the non-heated part of the bending line that is given stronger resistance to the bending operation may be a reason for an accelerated bending. As the laser makes progress over the sample, the non-heated (yet to be bent) part gets smaller and thus the resistance to bending is reduced. As already discussed in Section 3, the experimental results involving the bending of the plate as a whole showed no differences in the bending angle behavior for line 2, 3, 4 and 5 (refer to Fig. 6.2). Moreover, if the accelerated mechanism would be present then one would expect bending angle acceleration during the entire LF process. Because this acceleration occurs only at the end (region 2–3, Fig. 6.3) this must be associated with a temperature increase only because of the decreasing cooling ability near the sample edge.

As mentioned previously, the primary processing factors in laser forming are laser power, scanning speed and plate thickness. It is indicated in [3] that in the fields of welding and flame heating the parameters $\frac{P}{t\sqrt{v}}$ or $\frac{P}{\sqrt{v}}$ are used as the dependent parameter(s) to analyse the process variable effects on the bending angle. Results of the in situ laser forming observations summarized in Fig. 6.5 clearly demonstrate that the final bending angle in LF of 3-mm thick Ti plates cannot be represented by a single linear least square fit because of the significant scatter in the data points represented by the different scanning speeds when the final bending angle is plotted against $\frac{P}{v}$. Replacing the line energy with the parameter $\frac{P}{\sqrt{v}}$ in Fig. 6.5 results in the graph shown in Fig. 6.12.

The final bending angle data for the as-received sample surface results in a narrower band for all three scanning speeds. A linear fit over all data points in Fig. 6.12 yields a reasonable estimate of the predicted bending angle as a function of laser power and scanning speed in agreement with a rather simple model proposed earlier [5]. The relationship between bending angle, power *P* and velocity v_l is given by

$$\alpha_b = 0.009\left(\frac{P}{\sqrt{v_l}}\right) - 0.632 \tag{6.4}$$

with a R^2 value equal to 0.8986. The preference for using $\frac{P}{\sqrt{v_l}}$ as the dependent variable in Eq. (6.4) instead of $\frac{P}{v_l}$ is that Eq. (6.4) can calculate the final bending angle of 3-mm thick CP Ti with laser scanning speeds ranging between 10 and 20 mm/s. The standard deviation of residuals from the linear fit in Fig. 6.12 is approximately 18 % which is a significantly closer prediction than what was previously reported by [4] in their Fig. 6.2 which range between 45 and 100 %.

It should be emphasized that the impetus for using the square root instead of the linear dependence on velocity was not purely a scientific one based on the physical reasoning but rather to propose an equation to predict an estimated value for the final bending angle. Nevertheless, it is noteworthy that based on qualitative physical arguments a square root instead of a linear dependence on velocity can be expected by realizing that the bending phenomenon appears due to a stress gradient.

As explained already in Chapter 3: Taking linear elasticity as a starting point, a stress gradient $\partial\sigma$ can be converted to a gradient in thermal strain $\partial\varepsilon$ as a result of a temperature gradient ∂T. As a consequence, the temperature gradient can be written as the product of heat density input Q, i.e., the heat input of the laser with power P per unit area, and the heat resistance, which is nothing else than the thermal diffusion length l over the thermal conductivity K, i.e., a higher thermal conductivity means a lower heat resistance.

Taking phonons as the crucial carriers of heat transport in metallic systems the thermal diffusion length is, in a first approximation, proportional to the square root of the product of thermal diffusivity κ and the interaction/dwell time τ_l involved. The latter is inversely proportional to the laser beam velocity v_l, i.e., the bending angle α_b becomes inversely proportional with the square root of v_l, i.e.,

$$\alpha_b \propto \delta\sigma \propto \delta\varepsilon \propto \delta T \propto \frac{Ql}{K} \propto P\sqrt{\kappa\tau_l} \propto \frac{P}{\sqrt{v_l}} \tag{6.5}$$

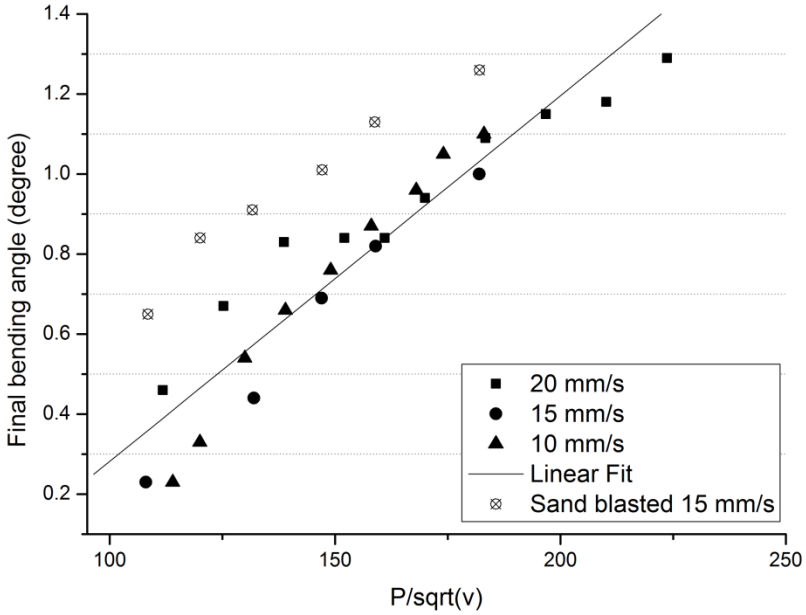

Fig. 6.12: Final bending angle versus $\frac{P}{\sqrt{v}}$ *parameter for 20, 15 and 10 mm/s, single scanned track on CP Ti.*

It should be noted that for multiple overlapping tracks the bending angle per track from the second to sixth track slowly decreases to an almost constant bending angle per track. This could be attributed to a build-up of residual stresses in the LHAZ since it has been previously reported by [17] that the relieved residual stresses can be as high as 108 MPa after the sixth scan. The fact that the bending angle between the first and the second laser scan increased between 5 % and 24 % can be attributed to the change in surface absorptivity after the first track passes the surface when moving from the first to the second track.

For an in-depth understanding of the heat flow within the material a 3D time dependent FEM is generated using COMSOL Multiphysics. An example of the iso-surface plot for the track processed with a laser power of 440 W and a speed of 10 mm/s is presented in Fig. 6.13. The heat transfer during the laser forming process, when the beam is located in the middle of the track length is illustrated. The area for the high temperature isolines stay roughly circular, however, during the conduction of heat the isothermal lines become egg shaped because of the movement of the laser on the surface.

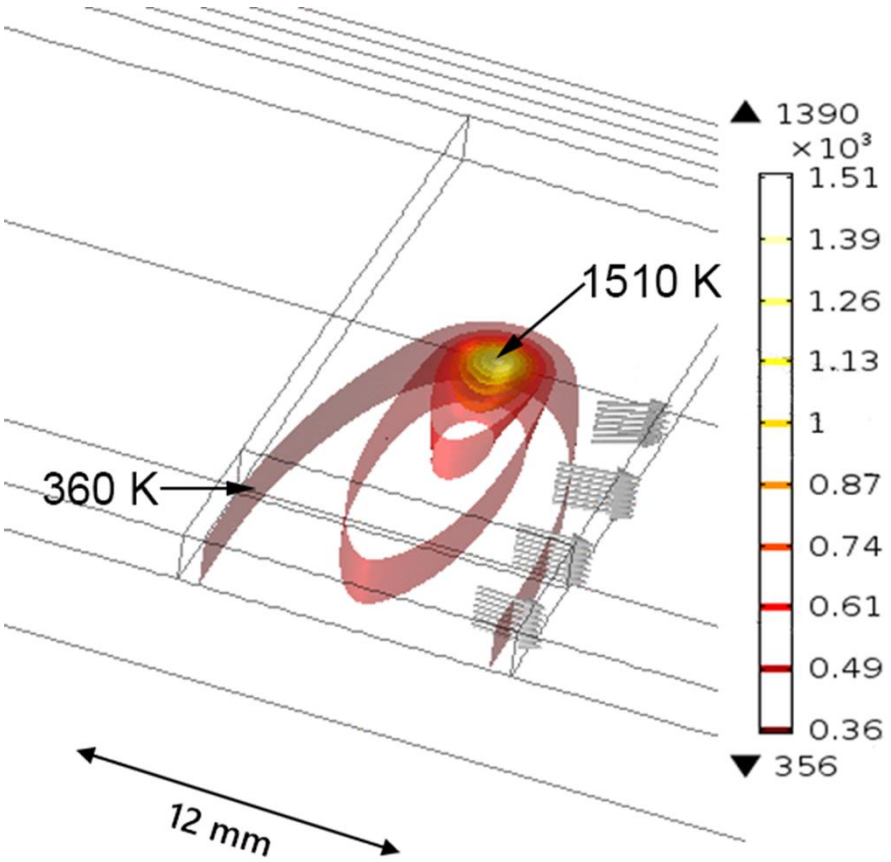

Fig. 6.13: A 3D iso-surface temperate plot (in Kelvin) of the laser beam heat model, showing iso-surfaces of different temperatures. The arrows represent a direction of the heat flux.

Furthermore, the maximum temperature value is almost constant as the laser beam moves over the plate, until the laser beam approaches the edge where the maximum temperature rises causing the previously mentioned edge effect. For example, using parameters of 720 W and 20 mm/s, the maximum temperature at the position shortly behind the beam center rises from 1390 K in the center of the track length to 1540 K at the edge of the sample as shown in Fig. 6.14 by the dashed line. This FEM allows calculation of the temperature history at any point inside the plate. By highlighting the temperature range of the α to β phase transformation in the graph where the maximum temperature is plotted as a function of depth for different combinations of processing parameters (Fig. 6.14), an expected depth of the phase change can be estimated. These estimated depths are almost identical to

the experimentally measured depths of the LHAZ microstructure, as shown in Fig. 6.9. Although the experimental data was used to calibrate the FEM and the FEM was used to determine the dependence of the maximum temperature on the depth of the sample for different laser power and scanning speeds, it should be noted that the FEA was used as primary purpose of serving as supporting tool in order to understand the underlying physical phenomena of the laser process and not as an exact measure for validating the results obtained with the laser scanning speed. Similar results for the sample depth have been reported by [8] in which only an approximate equation for heat transfer in titanium has been used. Therefore it can be concluded that the size of the LHAZ observed by EBSD is identical to the volume undergoing phase transformation.

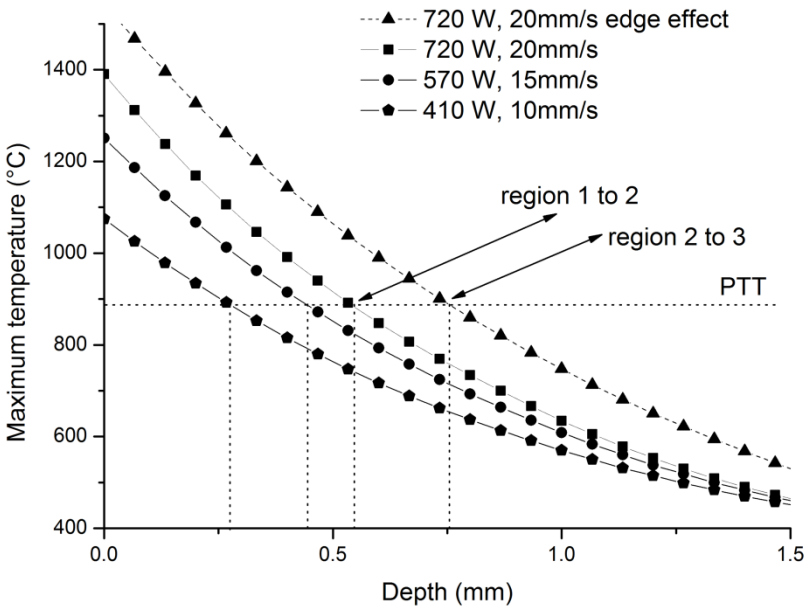

Fig. 6.14: Maximum temperature achieved in the points under track center plotted against their distance from the surface (depth) calculated from the FEM. The α to β phase transformation temperature (PTT) is highlighted and the depth in which transformation occurs is estimated by vertical dashed lines. A difference between the phase transformation depth at the center of the laser track (bending with slow rate, region 1 to 2 in Figs. 6.3 and 6.4) and on the edge of the plate (accelerated bending, region 2 to 3 in Figs. 6.3 and 6.4) is also shown.

By extrapolating the abovementioned model, one can determine a relationship between the laser power, scanning speed and maximum surface temperature.

The results shown in Fig. 6.15 are a set of maximum surface temperatures of 1325 K, 1546 K and 1734 K with respect to a varying scanning speed (5 to 25 mm/s).

A correlation of the bending angle and depth of LHAZ is observed when comparing Figs. 6.9 to 6.14. Detected local strain by KAM reveals that the amount of the (peak) local strain is not substantially different between the as-received and sandblasted specimens, although, the depth of local strain increased. Furthermore, the actual size of the transformed microstructure volume (indicated by the KAM) determines the size of the bending angle. This increase in KAM depth from the surface varied between approximately 20 to 38 %. It was also established that the LHAZ boundary is in agreement with the depth of the α to β phase transformation line determined by the FEM. In Fig. 6.15 it is shown that the maximum temperature achieved depends on the scanning speed and the laser power. Three isotherm curves are shown which illustrate that in order to achieve a phase transformation temperature at some particular depth with an increase in scanning speed it is necessary to increase the laser power proportional to $\sqrt{v}$. This is illustrated by the inserted figure on the top left-hand side of Fig. 6.15.

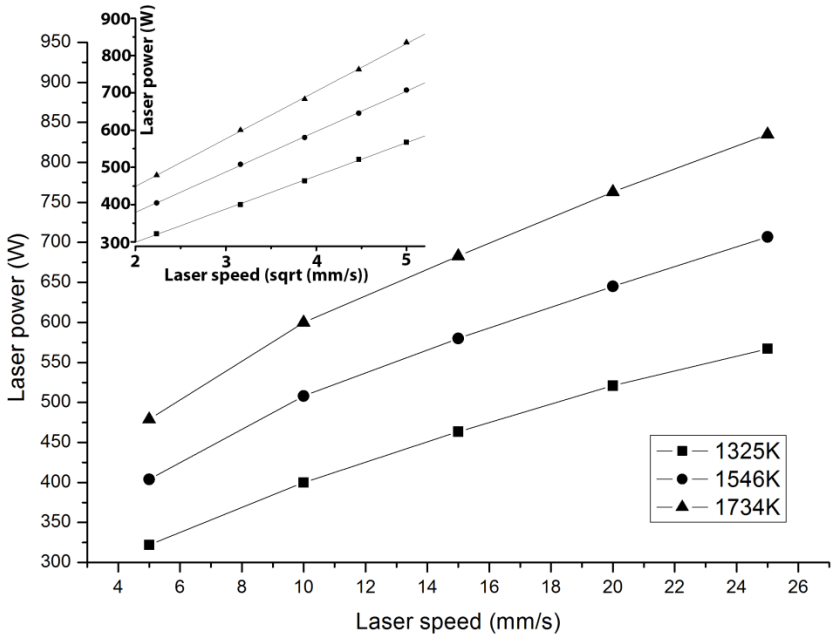

Fig. 6.15: The laser power plotted against the laser scanning speed for three maximum surface temperatures. The inserted figure on the top left-hand side represents the laser power versus square root of the laser scanning speed with a linear regression indicated for each maximum surface temperature.

It is known that sandblasting could substantially influence the amount of absorbed laser energy. Therefore the size of the transformed volume also changes substantially and this is the reason why the bending angle was significantly increased for samples after sandblasting. On the other hand, the grain size could affect the size of the transformed area mostly via a change in thermal conductivity, but the effect is much smaller in comparison with a change in absorption after sandblasting (as shown in Fig. 6.7).

6.4 Conclusions

A correlative comparison is presented between laser forming parameters and microstructural changes by utilizing in situ digital image correlation and electron backscatter diffraction techniques. Digital image correlation revealed that the final bending response is uniform over the entire plate width and no torsional effects can be observed when using a 3-mm thick commercially pure titanium sample. The behavior of the material because of the laser forming process may offer the industry relevant information when considering advanced forming methods. The conclusions are summarized as follows:

1. The bending rate during the laser forming process is constant and increases as the laser beam moves over the final plate edge. For multiple overlapping tracks the final bending angle per track varies for each of the processing parameters (laser power and scanning speed) but decreases slightly to an asymptotic value.
2. The final bending angle of a thick Ti plate scales with the ratio $\frac{P}{\sqrt{v}}$ where P represents the laser power and v is the laser beam scanning speed. However, surface roughness and therefore different absorptivity substantially influences the final bending angle.
3. The local strain by KAM suggests that the amplitude of local strain does not depend critically on the processing conditions. However, the total strain increases with the depth of the LHAZ. Both deformation mechanisms (dislocation slip and twinning) are detected. However sandblasted samples with large grains show a high degree of pyramidal first-order <C+A> slip near the treated surface.

Specifically for a relatively thick (3 mm) Ti plate and the range of laser processing parameters used, the actual size of the volume of the transformed microstructure determines the magnitude of the bending angle. FEM showed agreement between the phase transformation depth and the microstructurally

determined size of the LHAZ. Experimental observations also prove that the depth of the LHAZ scales with $\frac{P}{\sqrt{v}}$ rather than with $\frac{P}{v}$, similarly as the final bending angle.

6.5 References

[1] Y. Namba, Laser Forming of Metals and Alloys. In Proceedings of the LAMP'87, Osaka, Japan, 21–23 May 1987; pp. 601–606.

[2] K. Scully, Laser Line Heating. *J. Ship Prod.* 1987, *3*, 237–246.

[3] F. Vollersten, Mechanisms and Models for Laser Forming. In Proceedings of the Laser Assisted Net Shape Engineering Conference,; Meisenbach: Bamberg, Germany, October 12 – 14 1994; pp. 345–359.

[4] H. Shen and F. Vollertsen, Modelling of laser forming—An review. *Comput. Mater. Sci.* 2009, *46*, 834–840.

[5] M. Geiger and F. Vollertsen, The Mechanisms of Laser Forming. *CIRP Ann.* 1993, *42*, 301–304.

[6] M. Geiger, M. Merklein and M. Pitz, Laser and forming technology—An idea and the way of implementation. *J. Mater. Process. Technol.* 2004, *151*, 3–11.

[7] A. Els, H. Fidder, S. Woudberg and P.J. McGrath, Mechanical Characterisation of the Effect of Various Forming Processes Applied to Commercially Pure Titanium. *Mater. Charact.* 2014, *96*, 206–212.

[8] H. Fidder, V. Ocelík, A. Els and J.T.M. De Hosson, Response of Ti microstructure in mechanical and laser forming processes. *J. Mater. Sci.* 2018, *53*, 14713–14728.

[9] Y. Shi, C. Zhang, G. Sun and C. Li, Study on reducing edge effects by using assistant force in laser forming. *J. Mater. Process. Technol.* 2016, *227*, 169–177.

[10] M. Safari, and M. Farzin, Experimental investigation of laser forming of a saddle shape with spiral irradiating scheme. *Opt. Laser Technol.* 2015, *66*, 146–150.

[11] S.S. Chakraborty, H. More and A.K. Nath, Laser forming of a bowl shaped surface with a stationary laser beam. *Opt. Lasers Eng.* 2016, *77*, 126–136.

[12] K. Maji, D.K. Pratihar and A.K. Nath, Experimental investigations, modeling, and optimization of multi-scan laser forming of AISI 304 stainless steel sheet. *Int. J. Adv. Manuf. Technol.* 2016, *83*, 1441–1455.

[13] F. Vollertsen, I. Komel and R. Kals, The laser bending of steel foils for microparts by the buckling mechanism-a model. *Model. Simul. Mater. Sci. Eng.* 1995, *3*, 107.

[14] C.L. Yau, A New Analytical Model for Laser Bending. Laser Assisted Net Shape Engineering 2. In Proceedings of the LANE'97, Erlangen, Germany, 23–26 September 1997; pp. 357–366.

[15] T.C. Chu, W.F. Ranson and M.A. Sutton, Applications of digital-image-correlation techniques to experimental mechanics. *Exp. Mech.* 1985, *25*, 232–244.
[16] T. Pretorius, G. Habedank, J. Woitschig and F. Vollertsen, Thermal Generation of Residual Stress Fields for Purpose of Distortion Minimization. *Materialwissenschaft und Werkstofftechnik* 2006, *37*, 85–91.
[17] H. Fidder, A. Els, S. Woudberg, P.J. McGrath, V. Ocelik and J.T.M. De Hosson, A study of microstructural fatigue and residual stress evolution in titanium plates deformed by mechanical and laser bending. In *Surface Effects and Contact Mechanics Including Tribology*; De Hosson, J.T.M., Hadfield, M., Brebbia, C.A., Eds.; WIT Press: Southampton, UK, 2005; pp. 23–34.
[18] I. Basu, H. Fidder, V. Ocelík and J.T.M. De Hosson, J. Local Stress States and Microstructural Damage Response Associated with Deformation Twins in Hexagonal Close Packed Metals. *Crystals* 2018, *8*, 1.
[19] T. Hennige, Development of irradiation strategies for 3D-laser forming. *J. Mater. Process. Technol.* 2000, *103*, 102–108.
[20] W. Li and Y.L. Yao, Laser Forming with Constant Line Energy. *AMT* 2001, *17*, 196–203.
[21] C. Li, K. Muneharua, S. Takao and H. Kouji, Fiber laser-GMA hybrid welding of commercially pure titanium. *Mater. Des.* 2009, *30*, 109–114.
[22] S.I. Wright, M.M. Nowell and D.P. Field, A Review of Strain Analysis Using Electron Backscatter Diffraction. *Microsc. Microanal.* 2011, *17*, 316–329.
[23] Z. Zeng, Y. Zhang and S. Jonsson, Deformation behaviour of commercially pure titanium during simple hot compression. *Mater. Des.* 2009, *30*, 3105–3111.
[24] H.S. Carslaw and J.C. Jaeger, *Conduction of Heat in Solids*; Clarendon Press: London, UK, 1959.
[25] J.V. Beck, K.D. Cole, A. Haji-Sheikh and B. Litkouhi, *Heat Conduction Using Green's Function*; Taylor & Francis: New York, USA, 1992; ISBN 978-0-429-25836-7.
[26] M.N. Özısık, *Heat Conduction*; John Wiley & Sons: New York, USA, 1993.

Chapter 7

Local Stress States and Microstructural Damage Response Associated with Deformation Twins in Hexagonal Close Packed Metals

7.1 Introduction

The current work implements a correlative microscopy method utilizing electron back scatter diffraction, focused ion beam and digital image correlation to accurately determine spatially resolved stress profiles in the vicinity of grain/twin boundaries and tensile deformation twin tips in commercially pure titanium. Measured local stress gradients were in good agreement with local misorientation values. The role of dislocation-boundary interactions on the buildup of local stress gradients is elucidated. Stress gradients across the twin-parent interface were compressive in nature with a maximum stress magnitude at the twin boundary. Stress profiles near certain grain boundaries initially display a local stress minimum, followed by a typically observed “one over square root of distance” variation, as was first postulated by [2]. The observed trends allude to local stress relaxation mechanisms very close to the grain boundaries. Stress states in front of twin tips showed tensile stress gradients, whereas the stress state inside the twin underwent a sign reversal. The findings highlight the important role of deformation twins and their corresponding interaction with grain boundaries on damage nucleation in metals.

7.2 Intrinsic Length Scales

The mechanical behavior of metals is to a large extent, influenced by the changes in intrinsic length scales and the interaction between different microstructural features associated with them. A microstructure can be essentially defined as the overall arrangement of crystallites/grains and

material defects (point defects, dislocations and grain/twin boundaries). Depending upon the volume of the probed region these features can considerably vary both topologically as well as dimensionally. Since the local stress state in a material is directly proportional to the density and spatial configuration of defects, this also means that internal/residual stresses can strongly vary across different length scales i.e., macro-, meso- and microscopic dimensions.

7.3 Background

Plastic deformation in metals is primarily carried out by the creation and motion of linear defects viz. dislocations. In polycrystalline materials with diverse grain orientations, the interfaces between differing crystallite orientations can present themselves as severe obstacles to dislocation motion. The resultant interaction between line defects and such grain boundaries often gives rise to complex geometrical configurations of stored dislocations that are associated with long-range elastic stress fields.

These stored dislocations are termed as geometrically necessary dislocations (GNDs), since they ensure the geometrical compatibility of deformed grains across the grain boundaries. Superposition of such stress fields invariably results in a strong spatial heterogeneity in local stress states. Needless to say, the variation in local GND density levels directly influences the distribution of microscopic residual stresses in the grain and grain boundaries. Internal stresses are also influenced by mutual interaction of line defects leading to local entanglements of dislocations i.e., forest dislocations or statistically stored dislocations (SSDs), but their numeric contribution in comparison with GNDs progressively diminishes with increasing applied strains due to saturation in dislocation densities of the former for strains above ~0.1–0.2 [1]. On the other hand, GND dislocation associated with grain boundaries continue to increase linearly with applied shear strain [1], thus acting as the primary contributors to strain hardening. Such correlation between GND density levels and local stress gradients has been utilized in the past to explain local hardening phenomenon due to dislocation pile-up at grain boundaries. Eshelby et al. [2] showed analytically that a dislocation pile-up ahead of an insurmountable obstacle such as a grain boundary would result in a stress gradient that varies as “one over the square root” of the distance from the obstacle. In fact, the stress field in front of the spearhead of the dislocation

pile-up resembles the stress field of a crack singularity in a linear elastic medium. Subsequent experimental observations by Hall [3,4] and Petch [5] independently re-established such a behavior in metals as the well-known Hall-Petch effect, wherein the mechanical strength of the material increases with a decreasing intrinsic length scale of the grain size.

The dislocation configuration near a grain boundary strongly determines the degree of pile-up and corresponding local stress concentration. Depending on the crystallography of the grain boundary certain slip/twin systems may find conjugate systems in the neighboring grain that facilitate complete or partial strain transfer. It must be mentioned here that like slip deformation, twins are described by their twinning plane and the direction of shear. A theoretical estimate of the feasibility of slip/twin transmission can be captured by the strain transfer parameter [6, 7], expressed as,

$$m' = (\vec{n}_1.\vec{n}_2)(\vec{b}_1.\vec{b}_2) \tag{7.1}$$

where $\vec{n}_1$ and $\vec{n}_2$ are the normalized intersection line directions common to the slip/twinning planes and the boundary plane, and $\vec{b}_1$ and $\vec{b}_2$ are the normalized slip/twinning shear directions in the pile-up and emission grains. The value of m' provides a measure of the probability for possible transmissivity of a slip or twinning dislocation across the grain boundary. Maximization of the strain transfer parameter m' abates dislocation pile-up and promotes easier strain transfer across the grain boundary. Precise measurement of residual stresses at different length scales is extremely vital in order to acquire a fundamental understanding of damage mechanisms in present day structural materials. Despite the availability of diverse techniques for estimating internal stresses such as, using hard X-rays, hole drilling, contour method, slitting and ring coring, very few methodologies allow estimation of stresses up to micron and sub-micron scale resolution. Diffraction techniques utilizing convergent beam or nano-beam and hard X-rays from a synchrotron are some of the available methods that can resolve stress at inter/intra-granular level [8], but the availability of such facilities are scarce [9]. Lately, the measurement of local scale stresses can be performed by high resolution electron back scatter diffraction (HR-EBSD) wherein Kikuchi patterns from reference (un-deformed) and deformed states are used to measure the residual displacements, and subsequently calculate the local elastic strain and stress state [10–14]. However, the method is limited to 2-

dimensional investigations wherein only subsurface information is obtained [8]. With the advent of dual-beam focused ion beam (FIB) field emission gun microscopes, measurement of residual stresses with simultaneous sub-micron lateral and depth resolution in a semi-automated and robust way [9] is made possible. In this way both the subsurface and bulk deformation contribution on internal stress build up is accounted for during stress quantification. The methodology utilizes correlative imaging and milling to remove material and estimate the local stress relaxation in the neighborhood. Depending upon the milling geometry, either multiple stress components of the whole stress tensor can be determined or spatial stress gradients along one stress component is evaluated. Digital image correlation (DIC) is utilized to determine relaxation induced displacements in the vicinity of the milled region. In previous studies [15, 16] the authors introduced a site-specific technique utilizing electron back scattered diffraction (EBSD) and FIB-DIC linear slit milling to accurately determine spatially resolved stress profiles in the vicinity of grain boundaries in commercially pure titanium. The investigations in the vicinity of different grain boundaries in commercially pure titanium revealed the appearance of a local stress minimum just next to the boundary. This was followed by a Hall-Petch type monotonic stress decrement to a steady state regime. Correlations with the GND density and local misorientation data further validated the observed trends (c.f. Fig. 7.1a,b). The results further showed that the width over which the stresses relaxed in the vicinity of the boundary was strongly dependent upon the obstacle strength of the grain boundary i.e., the Hall-Petch coefficient, k_{HP} (c.f. Fig. 7.1c). The observed stress drop was justified by a local change in elastic stress fields arising from dislocation-dislocation and dislocation-grain boundary interactions that may lead to a relative depletion of dislocation densities in the vicinity of specific grain boundaries. It was shown that the stress fields due to dislocation-grain boundary interactions are long range in nature and can be of the order of 10^{-3} G even at distances $\approx 10^4 \cdot b_d$ (where, G is the shear modulus and b_d is the magnitude of the Burgers vector for active dislocation slip) from the grain boundary plane.

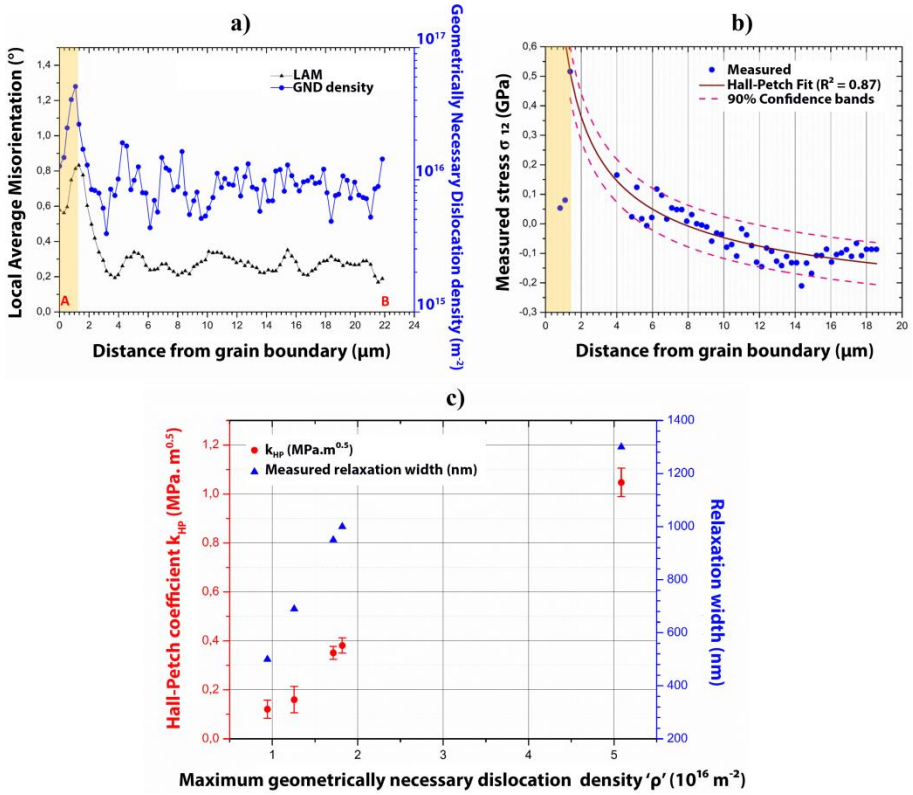

Fig 7.1: Local misorientation and stored dislocation densities in the vicinity of the grain boundary; (b) corresponding residual stress profile as a function of distance from the grain boundary; (c) variation of k_{HP} and relaxation width with the peak GND density measured in the vicinity of different grain boundaries (adapted from [15]).

Hexagonal crystal structures, due to their low symmetry, often exhibit anisotropic deformation behavior unlike face centered cubic metals with cubic symmetry. This typically arises from a lack of easily available slip deformation modes along the c-axis and the role of mechanical twinning in accommodating strain out of the basal plane [17–20]. Due to its inherent nature, deformation twinning strongly impacts crystallographic texture evolution as well as the grain scale stress evolution [21, 22]. While plastic slip is spatially more homogeneous and lattice strain evolution is gradual, the onset of twinning involves sudden reorientation of a part of the crystal associated with significant lattice strain and localized shear. The localized lattice rotation during twinning leads to the creation of twin boundaries. These newly formed boundaries can dynamically refine the grain size and lead to significant latent hardening inside the twins on subsequent straining [23, 24]. Furthermore, dislocations, grain-boundaries and twins can mutually interact.

Such complex local plastic response often gives rise to significant stress heterogeneities in the vicinity of twins. The significance of understanding such localized stress fields is in determining their associated effects either on accommodating deformation close to crack tips or on nucleation and propagation of cracks and thus their tendency to limit ductility [21, 22]. Unfortunately, due to the sudden nature of twin formation that comprises nucleation and propagation, capturing load partitioning between the twin and untwinned parent experimentally is still extremely important.

The current work therefore aims to extend the aforementioned combination of EBSD and FIB-DIC methodology to quantify stress fields arising from the interaction of twin boundaries with parent grains and grain boundaries in commercially pure titanium. The observed trends are subsequently discussed with respect to underlying physical processes and the subsequent impact of deformation twinning on fracture behavior of titanium is acknowledged.

7.4 Experimental Methods

Commercially available grade 2 titanium was subjected to room temperature in situ four-point bending test inside a Tescan Lyra dual beam (FEG-SEM/FIB) scanning electron microscope (Brno, Czech Republic). The initial microstructure comprised of coarse grains with a mean grain size of ~100 µm. Prior to mechanical testing, bending specimens were prepared for EBSD measurements using conventional metallographic techniques [25]. Specimens were strained to a final surface true strain of ε = 0.18. Microstructural characterization was performed by means of EBSD, thereby extracting both topographical and orientation information about the individual grains. A step size of 0.3 µm and hexagonal type of grid was used for the measurements. The acquired raw EBSD data was subsequently analyzed using EDAX-TSL OIM Analysis™ 7.3 software and the MTEX open source Matlab toolbox [26]. Slip traces in individual grains were imaged using in situ scanning electron microscopy (SEM) (Tescan Lyra, Brno, Czech Republic). The orientation of the grain boundary plane was determined by milling into the region containing the boundary using a focused ion beam and examining the grain boundary trace along the milled cross section. All observations were made on the tensile surface of the bent specimen, with the direction of viewing parallel to the surface normal, hereinafter referred to as the A3 sample axis.

7.5 Residual stress by FIB-DIC slit milling

The protocol followed during the measurement of residual stress starts with the acquisition of a scanning electron microscopy (SEM) image of the area to be analyzed. After recording the first image, a slit is milled on the surface. Then, a second image of the same area is taken. From the comparison of these two SEM images recorded before and after stress release by DIC the displacements are obtained. These displacements are compared with those obtained by the analytical solution for an isotropic elastic material, and the value of residual stress is obtained from the slope of the fitting [27]. Fig. 7.2 shows the geometry of the slit used in our experiments including its dimensions: a length *L*, a width *w* and a depth *a*. The evaluated displacements of the surface, u_x, are normal to the plane of the slit. The origin of coordinates is placed at the center of the slit. Considering the geometry, in plane displacements U_{dir} can be related to residual stress σ_{dir} in the same direction by an analytical expression such that [27–29]:

$$U_{dir} = \frac{2.243}{E'}\sigma_{dir}\int_0^a \cos\theta\left(1+\frac{\sin^2\theta}{2(1-\nu)}(1.12+0.18\,\mathrm{sech}\left(\tan\theta\right)\right)dz \quad (7.2)$$

where E' is $E/(1-\nu^2)$, E is Young's modulus, ν is the Poisson ratio, θ is equal to $\arctan(d/a)$, with *a* is the depth of the slit and *d* the distance from the slit and *dir* represents *x* or *y* directions. The displacements caused by the stress release depend on the slit depth *a* and are directly proportional to the σ/E ratio. Moreover, the extraction of the residual stress requires a priori knowledge of the elastic properties of the material under study (i.e., Young's modulus and Poisson's ratio). In the present study, the adopted rectangular slit geometry allows measurement of only one stress component that is aligned laterally to the longitudinal direction of the slit.

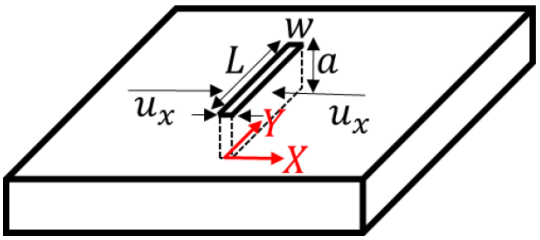

Fig. 7.2: Schematic of slit introduced by FIB milling.

SEM images acquired before and after FIB milling are processed using commercial digital image correlation software GOM Correlate v. 2016 and subsequent displacements lateral to the slit are recorded for each facet (group of pixels) position. Fig. 7.3 shows an example of a typically obtained DIC contour map of relative displacements normal to the slit corresponding to the local stress release due to milling. The scale bar of the image is in the range of tens of nanometers. Each color means that a group of pixels is displaced over the respective number of nanometers. When studying the displacements normal to the plane of the slit, the displacement is to the right (red color) or to the left (blue). Consequently, data arrays comprising of facet ID, coordinates and relative displacements are exported for post processing and residual stress determination. A Matlab based script is utilized to empirically determine the residual stress values from the experimentally measured displacements, as per Eq. (7.2).

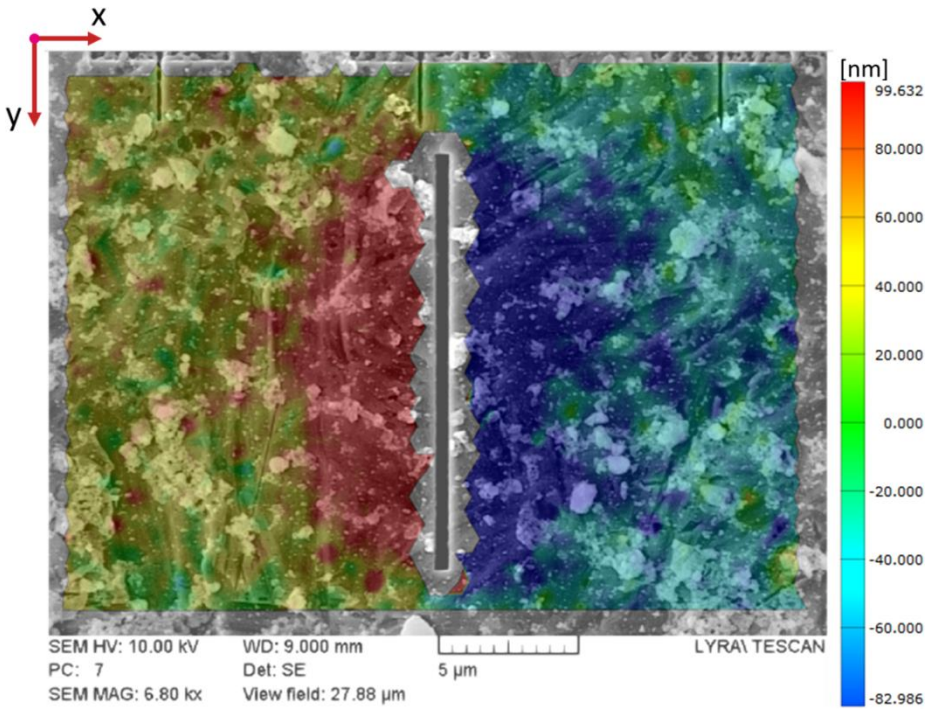

Fig. 7.3: An arbitrary example illustrating the displacement field map from DIC analysis in GOM; image acquired over a field of view of ~28 µm, the color bar on the right hand side shows the magnitude of recorded surface displacements due to stress relaxation by FIB milling along the x-direction on both sides of the slit. The values range between −100 to +100 nm.

In the present study, linear slits, oriented normal to the grain/twin boundary trace, with widths between 0.3–0.5 μm, depths from 1.5–2.5 μm, and lengths varying from 15–25 μm (depending on the twin/grain size), were milled inside individual grains/twins showing pile-up, classified on the basis of measured local lattice misorientation values near the grain/twin boundary. For each slit, multiple SEM images of resolution 768 × 768 pixels were acquired at high magnifications (field of view of 10–15 M) to ensure a high spatial resolution of measured displacement field. In order to obtain statistically sufficient data points, DIC was performed using a facet size of 19 × 19 pixels with a step width of 16 pixels. Yttria-stabilized Zirconia (YSZ) nano-particles were used for surface decoration to obtain optimum image contrast for high accuracy DIC analysis. To quantify displacements in the range of nanometers, the precision of measurements at reduced length scales at high magnifications is critical. The accuracy of the measured displacement field from DIC, $u_{x,y}$, depends upon the image pixel size along the x and y-directions, $N_{x,y}$ and the sub-pixel l shift resolution parameter k, given by the expression [28,30]:

$$u_{x,y} = kN_{x,y} \tag{7.3}$$

Under favorable imaging conditions the value of k achievable from the DIC algorithm is 0.01, which amounts to a precision of 1×10^{-5} [30, 31]. It must be mentioned here that the sub-pixel shift resolution is a major criterion for stress measurement with high spatial resolution. Due to the characteristics of the above expression, the measurement accuracy can be progressively improved with smaller imaging sizes i.e., view fields. In realistic cases, including imaging related drift inaccuracies, the sub-pixel shift resolution varies from 0.01 to 0.1. For instance, in the present study the pixel sizes range between 13–18 nm (for the above defined view fields and image resolution) leading to the resultant sensitivity of the DIC software of each measured displacement being in the range of 0.1 nm to 1.8 nm. In the present study, SEM imaging parameters were optimized according to [30] in order to minimize experimental drift related inaccuracies. Stress distributions at sub-microscopic length scales need not always be homogeneous i.e., constant stress all throughout the material, but may considerably vary spatially. In such cases, stress determination by simplistic averaging of all displacements along the slit length, misrepresents the actual stress state of the material. A multiple fitting approach [15, 29], wherein a stress value is obtained for displacements corresponding to each row was implemented to account for spatially heterogeneous stress states. All stress calculations were made using

orientation dependent elastic modulus values, extracted from [32], wherein the angle between the indentation loading axis and the crystal c-axis was varied to obtain an angular dependence of the elastic modulus with respect to the c-axis orientation.

7.6 Results and Discussion

7.6.1 Stress gradients across twin-parent interface

Fig. 7.4 illustrates a representative case of coherent twin-parent interface in titanium. Fig. 7.4a shows the inverse pole figure (IPF) map of the highlighted twin boundary in the inset image. The viewing axis corresponds to the A3 direction. The twinned region and the parent grain are labelled as 'T_{grain}' and 'P_{grain}', respectively. While the c-axis of twinned grain is oriented parallel to the viewing axis, the parent grain was oriented such that its c-axis was aligned with the tensile axis. Fig. 7.4a also shows the orientation of the milled slit lying between points A and B. Fig. 7.4 b,c represent the kernel average misorientation (KAM) and local average misorientation (LAM) mappings. The KAM physically describes the average misorientation spread between a reference pixel and its nearest neighbor pixels for a defined kernel size. The LAM angle corresponds to the misorientation averaged over all nearest neighbor pairs within a kernel. Both LAM and KAM values were calculated for the 2nd nearest neighbor with a threshold value of 2° [33]. {10-12} Tension twin boundaries are shown in red in Fig. 7.4 b,c. The characterization of twins in the EBSD maps (c.f. Fig. 7.4 b,c) was done on the basis of the characteristic misorientation angle of 85.03° about the <11-20> rotation axis (given in minimum angle-axis pair), which corresponds to the {10-12}<10-11> tension twin. A maximum angular deviation of ±6° was considered [34, 35]. The KAM and LAM maps indicate signs of stress concentration at the interface.

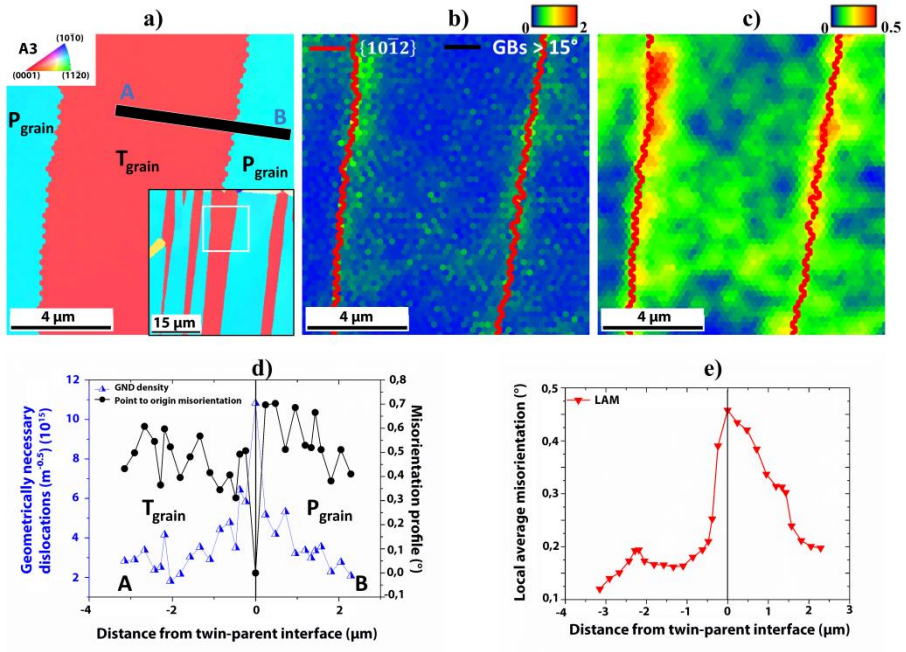

Fig. 7.4: (a) Inverse pole figure (IPF) map of twin lamellae intersecting a grain boundary; inset image shows a low magnification IPF map enclosing the area of interest highlighted in black square. Slit orientation between points A and B is shown schematically; parent and twin grains are labelled as P_{grain} and T_{grain}; (b) KAM and (c) LAM maps {10-12} <10-11> tension twin boundaries shown in red and high angle grain boundaries shown in black); (d) GND density and misorientation profile (with respect to the grain boundary) inside twin and neighbor grain; and (e) LAM profile between points A and B.

Fig. 7.4d shows the misorientation profile with respect to the interface along the twin grain and parent grain. The degree of misorientation between the twin center and the interface is of the order of ~0.6°, whereas between the boundary and parent grain interior it is ~0.7°. GND density values are additionally shown as a function of distance from the twin-parent interface. GND density (ρ_{GND}) values from EBSD data were calculated using the strain gradient approach [36, 37], given by the expression:

$$\rho_{GND} = \frac{2\theta}{n\lambda\left|\vec{b}_d\right|} \tag{7.4}$$

where θ is the experimentally measured KAM value, λ is the step size, n is the number of nearest neighbors averaged in the KAM calculation, and b_d is the magnitude of the Burgers vector corresponding to the active slip system in the grain. It must be noted that the GND values obtained from Eq. (7.4) provide a lower bound estimate as they can only account for contributions from the non-

paired edge dislocation segments and dislocation walls (since both lead to an effective unclosed Burgers circuit, thereby contributing to the measured local misorientation). Fig. 7.4e displays the LAM values with respect to the distance from the twin-parent interface. The maximum LAM value is recorded at the boundary as 0.45°. Both the GND and LAM values decrease monotonically on moving away from the twin boundary. The excellent agreement between the LAM and GND values is not surprising since both values are derived from the measured local misorientation. Fig. 7.5a shows the interaction of (10-10) prismatic slip bands with the twin-parent interface shown in Fig. 7.4. The corresponding local misorientation gradient due to slip accumulation at the interface is shown in the inset LAM map. Fig. 7.5b,c represents the FIB-DIC analysis and corresponding stress measurements for the region shown in Fig. 7.4. Fig. 7.5b shows the spatial orientation of the milled slit with respect to the twin boundary. The white dots correspond to the YSZ particles used for surface decoration. The twin boundary plane orientation is highlighted by the yellow parallelogram, with the twin plane normal defined as T_n. The measured stress values were resolved along the twin plane to obtain the shear component acting on the twinning plane along the twin boundary trace, designated as $\sigma_{1,Twinplane}$. Fig .7.5c displays the variation of $\sigma_{1,Twinplane}$ as a function of normal distance from the twin boundary i.e., along direction 2. The stress values all throughout the twin and parent remain compressive in nature, with a continuous transition across the interface. The magnitude of the stress is highest at the interface reaching up to a value of ~ −180 MPa, subsequently dropping to −80 MPa near the twin center. On the other hand, the stress values in the parent grain interior stabilize at ~ −110 MPa. On comparing the stress gradients with Fig. 7.4d,e the agreement seems excellent, thereby indicating that the observed stress fluctuations indeed confer to the actual stress state in the twin and parent grains.

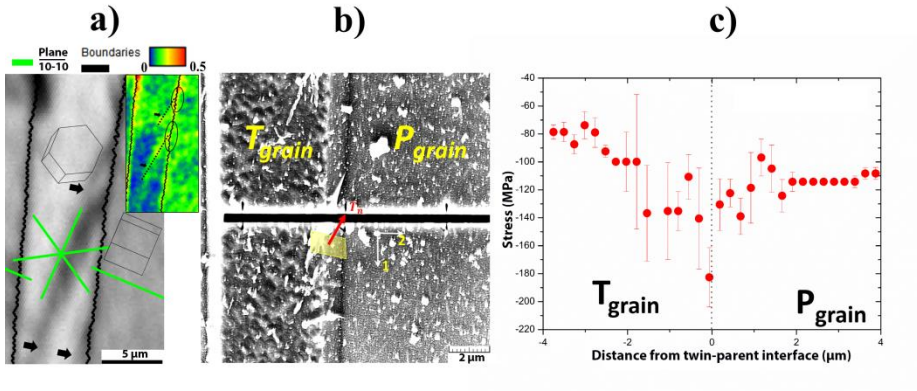

Fig. 7.5: (a) Image quality map showing instances of (10-10) prismatic slip bands interacting with twin parent interface; inset image shows corresponding local misorientation gradient along the identified slip trace; (b) SEM image of decorated twin-parent interface from Fig. 7.4a; the twin boundary plane orientation is shown in yellow with twin plane normal T_n. Slit coordinate system labelled by directions '1' and '2'; (c) corresponding measured resolved shear stress component ($\sigma_{1,Twinplane}$) along line AB.

The observations indicate the presence of compressive residual stress states acting parallel to the twin boundary plane. In order to understand the implications of such a stress state it is important to delve into the mechanism of migration of coherent twin-parent interfaces. The lateral broadening of a twin typically involves shear coupled migration of twin boundaries, whereby the normal translation of the boundaries is simultaneously accompanied by shearing of the parent grain. The magnitude of the theoretical twin shear S^t is characteristic for the twin type and in the case of {10-12} <10-11> tension twins is given as:

$$S^t = \frac{\left(\frac{c}{a}\right)^2 - 3}{\frac{c}{a}\sqrt{3}} \tag{7.5}$$

for titanium with c/a = 1.587, $S^t = 0.171$.

Twin boundary motion typically involves the glide of twinning dislocations/zonal dislocations, which are defined as regions wherein non-homogeneous shear at the twin matrix interfaces is accomplished at the expense of pure atomic shuffling in multilayer twin lamellae (c.f. Fig. 7.6a). The mechanism of lateral thickening is demonstrated in Fig. 7.6a. During

tensile loading, the stress component acting along the twin plane $\tau_{applied}$ typically drives the motion of twinning dislocations along the twin plane, resulting in shearing of the adjacent parent region and simultaneous thickening of the twin by a value Δh. This process repeats itself as long as the applied stress is sufficient to move the twinning dislocations and sustain the thickening process. In the unloaded state however, the presence of a compressive residual stress state generates a negative shear that may promote the motion of twinning dislocations in a direction opposite to that in case for externally applied stress (c.f. Fig. 7.6b). Such a scenario typically indicates the favorability of the twin lamellae to undergo thinning during unloading and also disappear when the applied load is reversed. This further explains why lower applied stresses are required to activate de-twinning as compared to twin nucleation during cyclic loading behavior, since the already present internal compressive stresses act as an additive stress to the applied load [38, 39]. Indeed, it must be noted that the considerations of anisotropy in twin boundary motion in the longitudinal and transverse directions, due to the former being shear dominated and the latter primarily driven by atomic shuffling, is also crucial to accurately understand the de-twinning phenomenon. In the forthcoming section, it will also be shown how the stress state at the twin tips further contribute to the aforementioned de-twinning effects, often observed in hexagonal close packed metals [40].

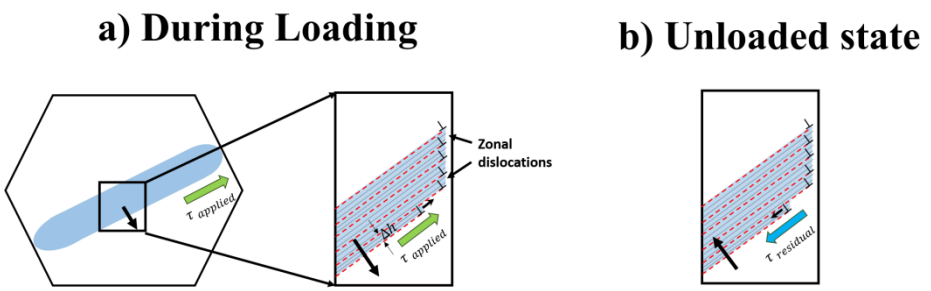

Fig. 7.6: (a) Schematic showing twin boundary migration leading to twin broadening under applied stress; the stress component parallel to the twin boundary drives the motion of zonal dislocations that result in simultaneous shearing and twin thickening i.e., shear coupled twin boundary motion (b) In unloaded state, compressive residual stress states can exert negative shear forces and subsequently favor opposite movement of twinning dislocations and concurrent twin shrinkage i.e., de-twinning.

7.6.2 Stress gradients from twin-grain boundary interactions

Fig.7.7 illustrates an instance of twin-grain boundary interaction wherein {10-12} tension twin lamellae impinge and are subsequently being blocked at the grain boundary. Fig. 7.7a represents the inverse pole figure map of the twin-grain boundary intersection zone, wherein two tension twins of the same variant meet the grain boundary (marked as GB). The selected area corresponds to the magnified view of the highlighted region in the inset image. The inset image indicates that the investigated twin could either arise in the blue grain by means of propagation of the dark pink twin in the neighboring green grain across the grain boundary or due to simultaneous nucleation of twins at the grain boundary, which subsequently propagate inside both green and blue grains. As in Fig.7.4a, the parent grain is denoted as 'P_{grain}', whereas the twinned domains are labelled as 'T_{grain}' and the neighboring grain is represented as 'N_{grain}'. A schematic of the orientation of the milled slit from point A to B is additionally shown in Fig. 7.7a. Fig. 7.7b,c represent the KAM and LAM maps of the same region, with twin boundaries highlighted in red and grain boundaries shown in black. Grain boundaries were designated by a lower threshold of 15° in Fig. 7.7b,c. A grain boundary map color coded with respect to the ease of twin transmission is presented in Fig. 7.7d. The values at the grain boundary of interest indicate a poor probability of twin transfer, evident by an m' value of 0.3 (c.f. Eq. (7.1)). Grain and twin orientations are further depicted by the spatial orientation of the hexagonal crystals. Traces corresponding to the twin plane (in orange) and twin shear directions (in blue) are also plotted in Fig. 7.7d. Fig. 7.7e shows the distribution of GND values as well as the misorientation profile with respect to the grain boundary along line AB. Fig. 7.7f indicates the LAM distribution along line AB. Fig. 7.7e,f indicate a peak lattice distortion and dislocation density in the vicinity of the grain boundary that decays to lower values on moving left (towards twin interior) or right (into the neighboring grain). Lattice rotations inside the twin near the twin-grain boundary interface are significantly high and drop drastically, within a width of 1 μm away from the grain boundary. On the other hand, the strain gradient in the neighboring grain shows a less sharp decrease. The GND and LAM values in the neighbor grain indicate a local minimum in the vicinity of the grain boundary, within a width of 440 nm.

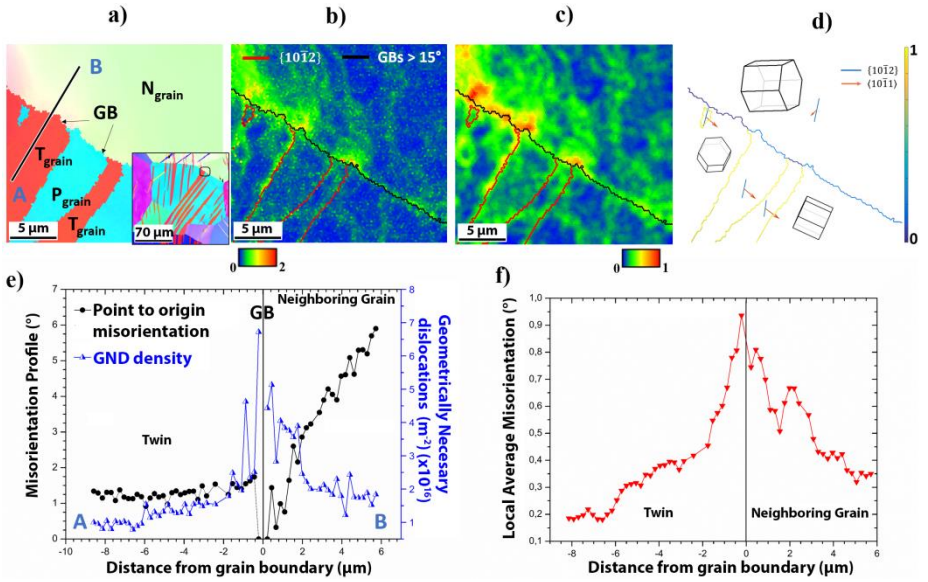

Fig. 7.7: (a) Inverse pole figure (IPF) map of twin lamellae intersecting a grain boundary; inset image shows a low magnification IPF map enclosing the area of interest highlighted in black square. Slit orientation between points A and B is shown schematically; parent, twin and neighbor grains are labelled as P_{grain}, T_{grain} and N_{grain}; (b) KAM, (c) LAM and (d) m' maps corresponding to twin transmission across grain boundary ({10-12} <10-11> tension twin boundaries shown in red and high angle grain boundaries shown in black); (e) GND density and misorientation profile (with respect to the grain boundary) inside twin and neighbor grain and (f) LAM profile between points A and B.

Fig. 7.8 presents the stress measurements obtained from the FIB-DIC slit milling technique. Fig. 7.8a presents the image quality map of the region shown in Fig. 7.7a, with a schematic of the slit. The twins, parent and neighbor grains are labelled as T_{grain}, P_{grain} and N_{grain}, respectively. Fig. 7.8b corresponds to a SEM image captured post slit milling of the region highlighted in Fig. 7.8a. The twin boundary plane orientation is depicted and the corresponding inclination of the twinning plane normal with respect to the sample surface is measured as 137°. The twinning shear direction, S_d is aligned with the normal to the slit wall, represented by axis 1. The longitudinal axis of the slit is labelled as '2'. Since the measured stress component from slit milling corresponds to σ_{11}, the corresponding stress component lying on the twinning plane and in the direction of twinning shear can be described as $\sigma_{1R} = \sigma_{11} \cdot \cos 47°$. Fig. 7.8c shows the orientation of the grain boundary plane, marked by the red arrow, to be perpendicular to the longitudinal axis of the slit, labelled as '2'. Fig. 7.8d represents the measured profile of resolved stress on the twin plane along the twinning shear direction, σ_{1R} along line AB.

The stress gradients inside the twin domain reveal high compressive stresses at the twin tip, reaching values up to ~ −170 MPa. On moving inwards, the stress values decrease considerably reaching values in the less negative/low positive range. On the other hand, the stress profile in the neighboring grain registers tensile stresses as high as ~50 MPa near the grain boundary that subsequently drop to very low positive values on moving away from the grain boundary. Agreeing with the trends seen in Fig. 7.7e,f, the stress values in the neighbor grain show a local minimum near the grain boundary.

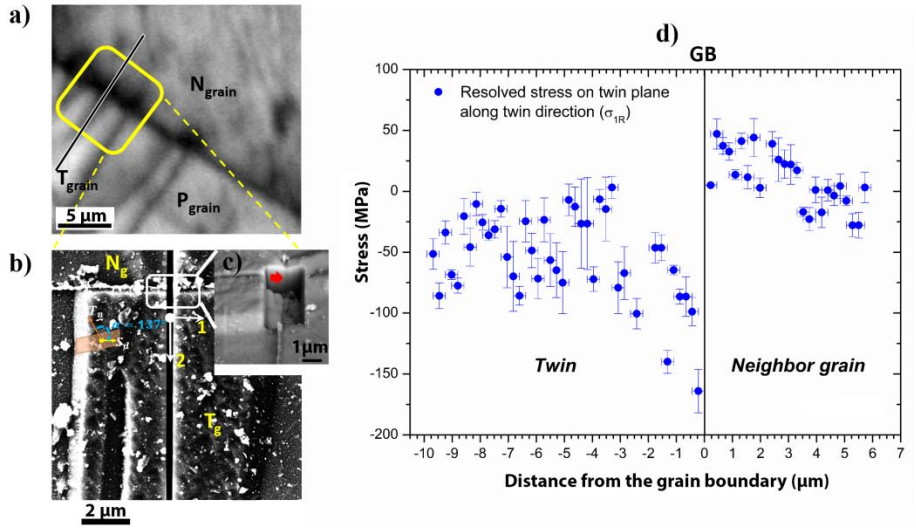

Fig. 7.8: (a) Image quality map of region shown in Fig. 7.7a with schematic of milled slit; (b) SEM image of decorated twin-grain boundary intersection from Fig. 7.7a; twin boundary plane orientation is shown in orange with twin plane normal T_n and twin shear direction S_d. Slit coordinate system labelled by directions '1' and '2', measured angle between twin boundary normal and axis '1' (normal to the slit wall) is displayed as 137°(HV 10kV, SEM MAG 18.14 kx, det. SE) ; (c) the orientation of the grain boundary plane (marked by red arrow) with respect to the slit length aligned normal to the wall of the milled trench (HV 10kV, SEM MAG 31.73 kx, det. BSE); (d) corresponding measured resolved shear stress component (along the twinning plane in the direction of twinning shear) along line AB.

Residual stress profiles measured inside the twin and the neighbor grain indicate a sign reversal in stress states across the twin-grain boundary interface. Previous studies employing simulations also reported similar observations of sign reversal of stress states in twin and neighboring grains [41–44]. In general, grain orientations in low symmetry hexagonal crystals can be classified into crystallographically 'soft' or 'hard' orientations, depending on whether they are initially favorably oriented for strain accommodation along the <a>-axis (i.e., basal or prismatic slip) or not. {10-

12} tension twinning typically results when the local stress along the c-axis of a crystallographically 'hard' parent orientation is tensile in nature. Under an externally applied stress, the soft orientations are typically the first to yield while the hard grain orientations, being elastically stiffer, undergo elastic straining due to lack of slip accommodation. This mechanism continues until a threshold stress is reached, whereby twinning is able to activate in the crystallographic hard grain orientations. Twinning in hexagonal crystals proceeds primarily via 3 stages: nucleation, propagation and lateral growth of the twin lamella. Nucleation involves formation of viable twin nuclei, a few atoms thick, preferably at grain boundaries associated with high localized stress concentration. It has been suggested that the twin nucleation mechanism is triggered by the interaction of grain boundary dislocations and stress driven slip dislocations [40]. Typically, the nucleation process is governed by two main factors, that is, the local resolved shear stress along the twinning shear direction on the twin plane and the ease of accommodation of twin associated shear in the neighbor grain (either by twinning or dislocation slip). The accommodation strains imposed on the neighboring grains by twinning can be readily calculated from the twinning shear by rotating its displacement tensor into the crystallographic reference frame of the neighboring grain.

Following nucleation, the twin propagates along the longitudinal direction, elongating in shape (Fig. 7.9a). The green arrows in Fig. 7.9a,b indicate the direction of the applied stress in the current study. Propagation refers to the process of the twin front moving, by means of glide of twinning dislocations, into the bulk of the grain and eventually terminating on encountering an obstacle such as the grain boundary. The orange arrow in Fig. 7.9b indicates the direction of the resolved shear stress component that drives twin propagation. Hereafter, further stress increase triggers lateral growth of the twins leading to their thickening (Fig. 7.9b). The mechanism of twin thickening is already described in Section 7.4.1 (c.f. Fig. 7.6a).

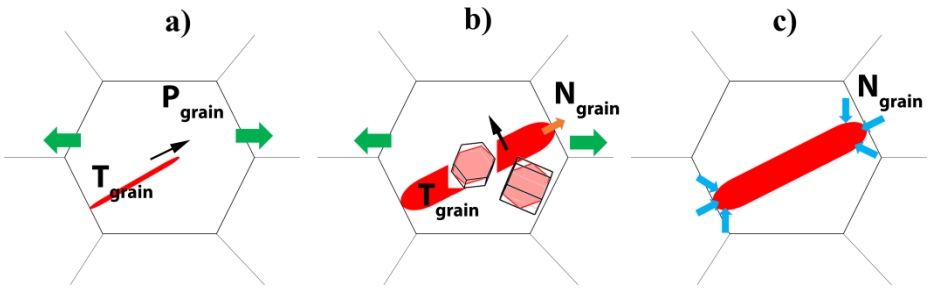

Fig. 7.9: (a) Schematic showing twin propagation in a parent grain, applied stress in the present study is depicted by green arrows, direction of propagation shown by black open arrow; (b) twin growth leads to lateral thickening under external stress once the twin hits the grain boundary, the forward stress component driving motion of twinning front (shown in blue arrow) is accommodated in the neighboring grain; (c) direction of back stresses acting on the twin in the investigated region during unloading that resist further twin growth.

While the part of the parent undergoing twinning undergoes significant stress relaxation, the untwinned parts of the parent grain, as well as the neighboring grains devoid of twinning show a significant increase in the internal stresses on further straining. Additionally, owing to the nearly 90° crystallographic reorientation of the twinned volume, the twins also assume a plastically hard orientation in terms of both slip as well as {10-12} tension twinning (Fig. 7.9b), leading to build up of large compressive internal stresses.

During unloading it is expected that the large internal stresses stored in the untwinned parent grain and the neighboring grains would impose considerable back stress on the twin (schematically illustrated by the blue arrows in Fig. 7.9c), which explains the observed compressive stress state inside the twin domain (Fig. 7.8d). The values of stresses near the twin tip in the present study reached values of −170 MPa. Comparing these values and the ones obtained in Section 4.1 to the typical critical resolved shear stresses for twinning in pure titanium that is around 125 MPa [45], indicates that the reaction stresses at the twin tips as well as along the twin boundary plane are significant enough to trigger mechanisms such as de-twinning in these regions. Furthermore, the high back stresses near the tips and low values at the mid region of the twin also comply with the typically seen lamellar twin morphology with converging tips (higher resistance to lateral growth) and a relatively thick mid-section (easier thickening under external stress).

The tensile stress gradient observed in the neighbor grain (Fig. 7.8d) most likely arises from the forward stress component (Fig. 7.9b) driving twin propagation (owing to the directional nature of twinning) and countering the

aforementioned back stress. When the twin hits the grain boundary this positive stress in front of the twin tip is plastically accommodated in the neighboring grain, either by slip or twinning. In the present case absence of twins and a steady change in misorientation observed in the neighbor grain (c.f. Fig. 7.7a–d) typically indicates slip induced strain accommodation. Similar to the observations in [15], the stress profile indicated a local minimum close to the boundary (Fig. 7.8d). This characteristic is attributed to the role of stress fields arising from superposition of twinning dislocations and grain boundary dislocations, which in turn influence the pile-up configuration.

7.6.3 Implications for macroscopic damage performance and fatigue behavior of hexagonal materials

The implications of the observations in the current work are significant in terms of understanding the role of twins on the fracture behavior in titanium. The findings indicate that stress development inside twins is significantly impacted by neighbor grain deformation as well as the plastic response of the untwinned parent. The values presented in the current study also highlight the role of twins in crack nucleation in the adjacent grain, especially at the twin tips. Furthermore, compressive back stresses acting parallel to the twin-parent interface in the unloaded state, along with the reaction forces at the twin tips explain the frequently observed dynamic microstructural changes induced due to internal back stresses during unloading via mechanisms such as, de-twinning or re-twinning [39, 40]. The measured values also indicate that stresses can be significantly large to easily drive such reverse migration of twin boundaries, thereby corroborating the frequently observed behavior of twins disappearing during cyclical loading experiments. The quantitative estimates of local stress profiles near twin boundaries provides an in depth understanding of microscale stress evolution, which is essential for designing microstructures that can enhance bulk scale mechanical performance.

7.7 Conclusions

A novel correlative technique utilizing EBSD and a FIB-DIC method for obtaining site specific microstructural and local stress information is presented. Stress gradients due to dislocation pile-up at pure titanium twin boundaries and at twin-grain boundary intersections are quantified. The following conclusions are drawn:

1. Stress gradients across the tension twin-parent interface were compressive in nature, with the maximum stresses recorded at the twin boundary. A resolved stress of ~−180 MPa acting along the twin boundary is reported. The results indicate that the in-built stresses are significant enough to promote reverse migration or de-twinning during reverse loading.

2. Stress profiles at twin grain boundary intersections show a sign reversal, being compressive inside the twin and tensile in the neighboring grain. The results provide a quantitative measure of back stresses exerted on the twin in the unloaded condition (which reach values as high as ~−170 MPa near the twin tips) and stress gradients originating in the neighbor grain due to the interaction of twinning dislocations and a grain boundary.

3. The stress values at the twin tips and in the twin center also highlight the role of local stresses in defining the typically observed lamellar morphology of twins with wider mid-sections and converging tips.

4. The observations in the current work highlight the contribution of residual stresses associated with deformation twinning in hexagonal close packed metals in predicting their damage behavior.

7.8 References

[1] E. Nes and K. Marthinsen, Modeling the evolution in microstructure and properties during plastic deformation of f.c.c.-metals and alloys—An approach towards a unified model. Mater. Sci. Eng. A 2002, 322, 176–193.

[2] J.D. Eshelby, F.C. Frank and F.R.N. Nabarro, XLI. The equilibrium of linear arrays of dislocations. Lond. Edinb.Dublin Philos. Mag. J. Sci. 1951, 42, 351–364.

[3] E.O. Hall, The Deformation and Ageing of Mild Steel: III Discussion of Results. Proc. Phys. Soc. Sect. B 1951, 64, 747.

[4] E.O. Hall, Variation of Hardness of Metals with Grain Size. Nature 1954, 173, 948–949.

[5] N.J. Petch, The Cleavage Strength of Polycrystals. J. Iron Steel Inst. 1953, 174, 25–28.

[6] Z. Shen, R.H. Wagoner and W.A.T. Clark, Dislocation and grain boundary interactions in metals. Acta Metall. 1988, 36, 3231–3242.

[7] W.A.T. Clark, R.H. Wagoner, Z.Y. Shen, T.C. Lee, I.M. Robertson and H.K. Birnbaum, On the criteria for slip transmission across interfaces in polycrystals. Scr. Metall. Mater. 1992, 26, 203–206.

[8] Y. Guo, D.M. Collins, E. Tarleton, F. Hofmann, J. Tischler, W. Liu, R. Xu, A.J. Wilkinson and T.B. Britton, Measurements of stress fields near a grain boundary: Exploring blocked arrays of dislocations in 3D. Acta Mater. 2015, 96, 229–236.

[9] B. Winiarski and P.J. Withers, Novel implementations of relaxation methods for measuring residual stresses at the micron scale. J. Strain Anal. Eng. Des. 2015, 50, 412–425.

[10] T.B. Britton and A.J. Wilkinson, Measurement of residual elastic strain and lattice rotations with high resolution electron backscatter diffraction. Ultramicroscopy 2011, 111, 1395–1404.

[11] T.B. Britton and A.J. Wilkinson, Stress fields and geometrically necessary dislocation density distributions near the head of a blocked slip band. Acta Mater. 2012, 60, 5773–5782.

[12] Y. Guo, T.B. Britton and A.J. Wilkinson, Slip band–grain boundary interactions in commercial-purity titanium. Acta Mater. 2014, 76, 1–12.

[13] J. Jiang, T.B. Britton and A.J. Wilkinson, Mapping type III intragranular residual stress distributions in deformed copper polycrystals. Acta Mater. 2013, 61, 5895–5904.

[14] Y. Guo, H. Abdolvand, T.B. Britton and A.J. Wilkinson, Growth of {11-22} twins in titanium: A combined experimental and modelling

investigation of the local state of deformation. Acta Mater. 2017, 126, 221–235.

[15] I. Basu, V. Ocelík and J.T.M. De Hosson, Measurement of spatial stress gradients near grain boundaries. Scr. Mater. 2017, 136, 11–14.

[16] I. Basu, V. Ocelík, and J.T.M. De Hosson, Experimental determination and theoretical analysis of local residual stress at grain scale. WIT Trans. Eng. Sci. 2017, 116, 3–14.

[17] J. Hirsch and T. Al-Samman, Superior light metals by texture engineering: Optimized aluminum and magnesium alloys for automotive applications. Acta Mater. 2013, 61, 818–843.

[18] I. Basu, G. Gottstein and B.D. Zander, Recrystallization Mechanisms in Wrought Magnesium Alloys Containing Rare-Earth Elements. Bachelor's Dissertation, RWTH Aachen University, Aachen, Germany, December 2016.

[19] I. Basu, T. Al Samman and G. Gottstein, Recrystallization and Grain Growth Related Texture and Microstructure Evolution in Two Rolled Magnesium Rare-Earth Alloys. Mater. Sci. Forum 2013, 765, 527–531.

[20] I. Basu and T. Al-Samman, Triggering rare earth texture modification in magnesium alloys by addition of zinc and zirconium. Acta Mater. 2014, 67, 116–133.

[21] M.H. Yoo, Slip, twinning, and fracture in hexagonal close-packed metals. Metall. Trans. A 1981, 12, 409–418.

[22] M.H. Yoo and J.K. Lee, Deformation twinning in h.c.p. metals and alloys. Philos. Mag. A 1991, 63, 987–1000.

[23] H. El Kadiri and A.L. Oppedal, A crystal plasticity theory for latent hardening by glide twinning through dislocation transmutation and twin accommodation effects. J. Mech. Phys. Solids 2010, 58, 613–624.Crystals 2018, 8, 1 15 of 15

[24] H. Qiao, X.Q. Guo, A.L. Oppedal, H. El Kadiri, P.D. Wu and S.R. Agnew, Twin-induced hardening in extruded Mg alloy AM30. Mater. Sci. Eng. A 2017, 687, 17–27.

[25] B. Taylor and E. Weidmann, Metallographic Preparation of Titanium, Struers Application Notes; Struers: Ballerup, Denmark, 2008.

[26] R. Hielscher and H. Schaeben, A novel pole figure inversion method: specification of the MTEX algorithm. J. Appl. Crystallogr. 2008, 41, 1024–1037.

[27] K.J. Kang, N. Yao, M.Y. He and A.G. Evans, A method for in situ measurement of the residual stress in thin films by using the focused ion beam. Thin Solid Films 2003, 443, 71–77.

[28] N. Sabaté, D. Vogel, A. Gollhardt, J. Marcos, I. Gràcia, C. Cané and B. Michel, Digital image correlation of nanoscale deformation fields for local stress measurement in thin films. Nanotechnology 2006, 17, 5264.

[29] C. Mansilla, D. Martínez-Martínez, V. Ocelík, and J.T.M. De Hosson, On the determination of local residual stress gradients by the slit milling method. J. Mater. Sci. 2015, 50, 3646–3655.

[30] C. Mansilla, V. Ocelík and J.T.M. De Hosson, A New Methodology to Analyze Instabilities in SEM Imaging. Microsc. Microanal. 2014, 20, 1625–1637.

[31] D.V. Nelson, A. Makino and T. Schmidt, Residual Stress Determination Using Hole Drilling and 3D Image Correlation. Exp. Mech. 2006, 46, 31–38.

[32] T.B. Britton, H. Liang, F.P.E. Dunne, A.J. Wilkinson, The effect of crystal orientation on the indentation response of commercially pure titanium: experiments and simulations. Proc. R. Soc. Lond. Math. Phys. Eng. Sci. 2010, 466, 695–719.

[33] M. Calcagnotto, D. Ponge, E. Demir and D. Raabe, Orientation gradients and geometrically necessary dislocations in ultrafine grained dual-phase steels studied by 2D and 3D EBSD. Mater. Sci. Eng. A 2010, 527, 2738–2746.

[34] C. Drouven, I. Basu, T. Al-Samman and S. Korte-Kerzel, Twinning effects in deformed and annealed magnesium-neodymium alloys. Mater. Sci. Eng. A 2015, 647, 91–104.

[35] I. Basu and T. Al-Samman, Competitive twinning behavior in magnesium and its impact on recrystallization and texture formation. Mater. Sci. Eng. A 2017, 707, 232–244.

[36] L.P. Kubin and A. Mortensen, Geometrically necessary dislocations and strain-gradient plasticity: A few critical issues. Scr. Mater. 2003, 48, 119–125.

[37] P.J. Konijnenberg, S. Zaefferer and D. Raabe, Assessment of geometrically necessary dislocation levels derived by 3D EBSD. Acta Mater. 2015, 99, 402–414.

[38] H. Qiao, S.R. Agnew and P.D. Wu, Modeling twinning and detwinning behavior of Mg alloy ZK60A during monotonic and cyclic loading. Int. J. Plast. 2015, 65, 61–84.

[39] L. Wu, S.R. Agnew, D.W. Brown, G.M. Stoica, B. Clausen A. Jain, D.E. Fielden and P.K. Liaw, Internal stress relaxation and load redistribution during the twinning–detwinning-dominated cyclic deformation of a wrought magnesium alloy, ZK60A. Acta Mater. 2008, 56, 3699–3707.

[40] I. Basu and T. Al-Samman, Twin recrystallization mechanisms in magnesium-rare earth alloys. Acta Mater. 2015, 96, 111–132.

[41] M. Arul Kumar, A.K. Kanjarla, S.R. Niezgoda, R.A. Lebensohn and C.N. Tomé, Numerical study of the stress state of a deformation twin in magnesium. Acta Mater. 2015, 84, 349–358.

[42] M. Arul Kumar, I.J. Beyerlein, R.J. McCabe and C.N. Tomé, Grain neighbour effects on twin transmission in hexagonal close-packed materials. Nat. Commun. 2016, 7.

[43] M. Knezevic, M.R. Daymond and I.J. Beyerlein, Modeling discrete twin lamellae in a microstructural framework. Scr. Mater. 2016, 121, 84–88.

[44] R.Y. Zhang, M.R. Daymond and R.A. Holt, A finite element model of deformation twinning in zirconium. Mater. Sci. Eng. A 2008, 473, 139–146.

[45] X. Wu, S.R. Kalidindi, C. Necker and A.A. Salem, Prediction of crystallographic texture evolution and anisotropic stress-strain curves during large plastic strains in high purity α-titanium using a Taylor-type crystal plasticity model. Acta Mater. 2007, 55, 423–432.

Samenvatting

Dit onderzoek concentreert zich op de structuur-eigenschappen relaties in met laser behandelde voorwerpen gemaakt van Titaan. Lasers worden in de materiaalkunde veelvuldig gebruikt voor oppervlaktebehandelingen maar dit proefschrift verkent een nieuw toepassingsgebied van lasers: het gebruik in de vormgeving van nieuwe producten. Het idee is dat thermische gradiënten die in het materiaal gecreëerd worden door lasers kunnen mee helpen om een product een bepaalde uitwendige macroscopische vorm te geven. Ons onderzoek concentreert zich op de fundamentele, materiaalkundige aspecten die bij 'laser-manufacturing-processing' een rol van betekenis spelen.

Kristallografische veranderingen spelen een belangrijke rol in het gedrag van deze zogenoemde hexagonaal-dicht-gepakte Titaan materialen bij blootstelling aan hoge opwarm- en afkoelsnelheden. De belangrijkste experimentele methode die werd gebruikt om de kristallografische structuur in kaart te brengen was elektron terugverstrooiing-diffractie (electron back-scatter diffraction, EBSD).

Dit proefschrift laat zien dat via de thermische controle met behulp van een laserbron een vooraf bepaalde gewenste vorm kan worden verkregen. Afkoelsnelheden bepalen ook of er fasetransformaties optreden die de verdere verfijning van de microstructuur beinvloeden. Bovendien worden in het materiaal thermische spanningen geïnduceerd als gevolg van gradiënt in de temperatuur. Zowel de microstructurele veranderingen als ook de restspanningstoestand zullen samen de uiteindelijke prestatie van de met de laser gemodificeerde voorwerpen bepalen. Dit is een belangrijk punt voor industriële toepassingen omdat de specifieke mechanische eigenschappen, zoals vermoeidheid en hardheid, bepaald worden door de microstructuur samen met de residuele spanningstoestand.

Uit ons onderzoek komt naar voren dat verschillende sets van laserparameters kunnen worden gebruikt om een plaat Ti te vervormen en te buigen tot vooraf bepaalde krommingen, die vergelijkbaar zijn met de buigingen die gebruikelijk zijn in de traditionele mechanische buigprocedures, variërend tussen 150 mm en 350 mm radii. Met behulp van de vooraf bepaalde laserinstellingen (laservermogen, en scansnelheid) werden alle voorwerpen

concaaf gebogen, d.w.z. naar de laserbron toe. Zoals in het proefschrift in detail wordt besproken, is thermische controle van de warmte toevoer met behulp van de laser van het grootste belang, aangezien laserinstellingen ook kunnen leiden tot convexe krommingen, d.w.z. die van de laserbron afbuigen. Zowel laser- als mechanisch gevormde (en een combinatie van de twee) voorwerpen lieten vergelijkbare vermoeiingseigenschappen zien. De laserbehandeling genereerde aanzienlijke interne restspanningen die in de regel hoger liggen in vergelijking met de restspanningen in mechanische vervormde voorwerpen.

Interessant is dat kristallografische veranderingen in de mechanisch vervormde voorwerpen overwegend gebaseerd waren op coherente tweeling vorming. Bovendien laten de door de laser vervormde voorwerpen een veel hogere dislocatiedichtheid zien, tot grote diepte in de voorwerpen als gevolg van de thermische spanningen en geïnduceerde lokale plasticiteit. Uiteraard spelen de experimentele parameters een cruciale rol bij de microstructurele veranderingen omdat de afkoelsnelheid het microstructurele gedrag van het laservormingsproces dicteert. De amplitude van de lokale spanning is minder afhankelijk van de precieze verwerkingsparameters, maar de totale spanning neemt wel toe met de diepte van de warmte beïnvloede zone (Heat Affected Zone: HAZ). We hebben aangetoond dat laservorming bepaald wordt door plastische vervorming, die bij hoge temperaturen essentieel anders is dan mechanische vorming bij kamertemperatuur.

Digitale beeldcorrelatie (Digital Image Correlation, DIC) toonde aan dat de uiteindelijke vervorming tijdens het laser-buigproces uniform is over de gehele plaatbreedte en dat er geen torsie-effecten werden waargenomen. De buigsnelheid is constant en neemt toe naarmate de laserbundel over de buitenste plaatranden beweegt. Voor meerdere overlappende sporen varieert de uiteindelijke buighoek per spoor, en nadert een asymptotische waarde. Eindige-elementenmodellering toonde de overeenstemming aan tussen de fase-transformatiediepte en de bepaalde grootte van de HAZ. Verder is aangetoond dat de buighoek in het laser proces omgekeerd evenredig is met de vierkantswortel van de lasersnelheid en lineair evenredig met de warmtedichtheid of laservermogen. Zowel kwalitatieve als kwantitatieve fysische argumenten werden voor deze control parameterruimte afgeleid en onderzocht

Voor een gedetailleerd inzicht in de structuur-eigenschap relatie werden de spanningsgradiënten als gevolg van opeenhoping van dislocaties aan tweelinggrenzen en aan tweeling-korrelgrenzen met behulp van EBSD en DIC-methoden nader bestudeerd. Spanningsgradiënten over de tweelinggrens waren compressief van aard, met een maximale spanning op de tweelinggrens. De resultaten geven aan dat de ingebouwde spanningen significant genoeg zijn om de migratie of tweelingvorming om te draaien gedurende het omkeren van de mechanische belasting. Interessant is dat de spanningsprofielen op de kruispunten van tweeling-korrelgrenzen een omkering vertonen van het teken, compressief binnen de tweeling en tegengesteld van teken (in trek) daarbuiten in de aangrenzende korrel.

Summary

This research concentrates on the structural crystallographic properties in laser assisted and mechanically deformed shapes within hexagonal closed packed (HCP) material. This thesis explores a new 'challenge and opportunity' for lasers in the field of manufacturing processing, i.e. using a laser as an innovative tool for *materials forming* purposes. Indeed the laser have been used before as a sophisticated heat source for manufacturing products but the *processing-structure-property* relationships have been largely neglected. Here, we present a detailed and in-depth study of the structure-performance relationships in laser assisted and mechanically deformed advanced materials.

Crystallographic changes play an important role in understanding the mechanical behavior of HCP materials when subjected to high heating and cooling rates. The main experimental technique used was electron backscatter diffraction (EBSD) which provides influential local and global map data due to the changes in crystallography between the forming processes. This thesis shows that through thermal control which is provided by the laser (a contactless process), a desired shape can be obtained while considering the working environment of the final product. Cooling rates determine if the phase transformations that occur are conformable to the equilibrium phase diagram and it also influences the refinement of the microstructure. Additionally, thermal stresses will be induced in the heat affected zone (HAZ) within the substrate as a consequence of the thermal gradient. Both microstructural changes and the residual stress state will determine the final performance of the laser-modified layer. This is important for industrial applications as it will give further insight into specific mechanical properties such as fatigue and hardness.

The comparison studies showed that different sets of laser parameters can be used to bend CP Ti to predetermined curvatures similar to that for the traditional mechanical bending procedures which ranges between 150 mm and 350 mm radii. Using predetermined laser settings (laser power, laser distribution profile and scanning speed) all samples bended concave, upwards towards the laser source. As discussed in Chapter 3, thermal control of the laser input is of utmost importance as different laser settings can also result in convex curvatures bending away from the laser source. Both laser and mechanical formed (and a combination of the two) specimens showed a

similar decrease in fatigue results when comparted to the substrate that was subjected to the same loading set-points. Laser formed specimens developed higher internal residual stresses when comparing it to the mechanical specimens.

Crystallographic changes within the mechanically formed specimens showed predominantly coherent twinning modes. Furthermore, the laser formed specimen's changes show a high degree of dislocation glide deeply inside the top and bottom sections due to the thermal stresses and induced local plastic buckling. As expected, it was found that the processing parameters play a critical role in the microstructural changes as the cooling rate dictates the microstructural behavior for the laser forming process. The local strain by kernel average misorientation suggests that the amplitude of local strain does not depend critically on the processing conditions but the total strain increases with the depth of the HAZ. We concluded that laser forming utilizes plastic deformation at high temperatures, while mechanical forming at room temperature is characterized by plastic deformation at low temperature.

Digital image correlation revealed that the final bending response during the laser forming process is uniform over the entire plate width and no torsional effects can be observed. The bending rate is constant and increases as the laser beam moves over the final plate edge. For multiple overlapping tracks the final bending angle per track varies for each of the processing parameters but decreases slightly to an asymptotic value. Finite element modelling showed agreement between the phase transformation depth and the microstructurally determined size of the HAZ. Furthermore it has been found that the bending angle becomes inversely proportional with the square root of the laser beam velocity and linearly proportional to the heat density or laser power at constant area.

Stress gradients due to dislocation pile-up of twin boundaries and at the twin-grain boundary was studied by utilizing EBSD, focus ion beam milling and DIC methods. Stress gradients across the tension twin-parent interface were compressive in nature, with the maximum stresses recorded at the twin boundary. The results indicate that the in-built stresses are significant enough to promote reverse migration or de-twinning during reverse loading. Stress profiles at the twin grain boundary intersections show a sign reversal, being compressive inside the twin and tensile in the neighboring grain.

Acknowledgements

Herewith my acknowledgements and gratitude for all the people that influenced my past ≈ 4.5 years during my PhD "tenure". It was an excellent and memorable time from a professional point of view (challenging and rewarding), but also from a personal perspective.

First and foremost I would like to give my thanks to Prof. Jeff De Hosson. Prof, thank you for giving me the opportunity to become a MK group "veteran". The amount of knowledge, dedication and passion that Prof invest in each student is something that I will always remember. Furthermore, the MK/research group model (researchers, equipment & support) is a paradigm to copy and paste at other institutions and not forgetting the conferences and industrial collaborations contributions. *Heel erg bedankt Prof.*
Een besondirlike herinnering was toe Prof tot ridder geslaan was. Dit was 'n baie spesiale geleentheid wat ek beleef het. Ook wil ek graag dankie sê dat ek kon Prof se laaste PhD student wees, dit was 'n voorreg.

Second is my daily supervisor, Vasek (Václav) Ocelík. Thank you for all the teachings in microscopy and software. You always have an open door (making time for each student) and encouraging in-depth discussions (laser, pole figures, texture etc. etc.) especially when things get difficult. I would also like to thank Helena Ocelík for opening your home to me during Christmas(es), holidays and birthdays. I hope to see you in the southern hemisphere when visiting me.

I want to thank the reading committee, Prof. dr. P. Rudolf, Prof. dr. H.A. De Raedt and Prof. dr. A. Botes for their careful reading of the thesis. My MSc students, Joris Admiraal for the contribution to the project and Roy Blum for the late night GND carbide discussions during your write-up (not to mention the AFM's quantum superposition).

Of course the people of the MK group are the central part of acknowledgements : Leo de Jeer whom was a great colleague and friend during the time in Groningen and yes we will continue the random

conversations, Gerrit Zijstra – spending time fixing your car(s) and moving to your new house, Enne (and Anna) Faber – moving to your new house, Willem van Dorp, Jintoa Shen – moving out your house, Erik Detsi, Ismail Hemmati, Ondrej Nenadl, Diego Gomes, Anatoliy Turkin, Mikhail Dutka, Deepak – Borrel sessions during meetings, Angela, Fabio, Theresa, Jean-Luca, Emad – for all the help in the lab's, Yutoa Pei, Diego and Catalina Martinez , Michiel Top and Remy Ripandelli.

David Vainchtein, thank you for all the help and paperwork, it was much appreciated. To the late Paul Bronsveld – I will always remember the random conversations (in Dutch to me but speaking English to the rest) and the M2i conferences. Indranil Basu – I have no doubt that you will be a great researcher. Thank you for the collaboration in Groningen and Zurich. All the best for the future.

Kitty, Alex, Jac, Jan and Yolanda, thank you for all the ***braai's*** in Spanbroek (NL) and Stellenbosch (ZA). See you soon for the traditional family gathering.

Menze, Anna, Kolya and Eric. Thank you for the past 4.5 years. I hope to see you soon in the southern hemisphere when visiting me.

I would like to thank Sonia for the time and experience that we have shared together in Groningen, and in particular for her support during the PhD. Thank you for being a supportive wife and mother. My last words will go to my son, Herman Johann Fidder. I always enjoy our laughs together and when you sleep on my shoulder.

Herman Fidder
Stellenbosch/Groningen
Juni 2020

List of publications

Journal papers

1. Fidder, H., Admiraal, J. P. J., Ocelík, V., & De Hosson, J. T. M. (2020). In Situ Digital Image Correlation Observations of Laser Forming. Metals, 10(1), [17]. https://doi.org/10.3390/met10010017

2. Fidder, H., Ocelík, V., Els, A., & de Hosson, J. T. M. (2018). Response of Ti microstructure in mechanical and laser forming processes. Journal of Materials Science, 53(20), 14713-14728. https://doi.org/(...)07/s10853-018-2650-4

3. Basu, I., Fidder, H., Ocelík, V., & De Hosson, J. T. M. (2018). Local stress states and microstructural damage response associated with deformation twins in hexagonal close packed metals. Crystals, 8(1), [1]. https://doi.org/10.3390/cryst8010001

4. Els A., Fidder, H., Woudberg S. and McGrath P.J. (2014). Mechanical characterisation of the effect of various forming processes applied to Commercially Pure Titanium, Materials Characterization, 96, pp 206-212. https://doi.org/10.1016/j.matchar.2014.08.012

5. H. Fidder, I. Basu, V. Ocelík, J.T.M. De Hosson. Deformation strain and strain rate on orientation relationship in pure α titanium (in preparation)

6. H. Fidder, I. Basu, V. Ocelík, J.T.M. De Hosson. Stress response of compression twins in hexagonal close packed metals (in preparation)

Conference proceedings

1. Fidder, H., Ocelik, V., & De Hosson, J. T. M. (2017). Microstructure transformation of Alpha-titanium after mechanical and laser forming. In WIT Transactions on Engineering Sciences (Vol. 116, pp. 215-222). WIT Press. https://doi.org/10.2495/MC170221

2. Fidder, H., Els, A., Woudberg, S., McGrath, P. J., Ocelik, V., & de Hosson, J. T. M. (2015). A study of microstructural fatigue and residual stress evolution in titanium plates deformed by mechanical and laser bending. 23-34. https://doi.org/10.2495/SECM150031

3. Fidder, H., Els, A., Woudberg, S. and McGrath P.J. (2013), Characterization of microstructure and fatigue life of CP titanium grade 2 specimens subject to various bending processes, in Surface effects and contact mechanics XI (Editors: J. Th. M. De Hosson and C. A. Brebbia), Proceedings of the 11th International Conference on Surface effects and Contact mechanics, Siena, Italy, 5-7 June 2013, WIT Press, UK, pp. 25-33. https://doi:10.2495/secm130031

4. Fidder H., Els A. and McGrath P.J. (2011). Origins of differences in S-N performance for cold worked and laser formed titanium, Proceedings of the New Metals Development Network Conference (ZrTa2011), Mount Grace Country House & Spa, Magaliesburg, 12–14 October 2011.

Book Chapters

1. Indranil Basu, Herman Fidder, Vaclav Ocelik and Jeff Th.M De Hosson, Local Stress States and Microstructural Damage Response Associated with Deformation Twins in Hexagonal Close Packed Metals, in Crystal Indentation Hardness, Eds. Ronald W. Armstrong, Stephen M. Walley, Wayne L. Elban, MDPI, Basel,Switzerland, 2018, pp.303-317. ISBN 978-3-03842-967-8 (Pbk), ISBN 978-3-03842-968-5 (PDF)